1984

Crossed molecular beam: I. Photoionization studies of hydrogen sulfide and its dimer and trimer, II. A rotating source crossed molecular beam apparatus

Harry Frank Prest
Iowa State University

Prest, Harry Frank

CROSSED MOLECULAR BEAM: I. PHOTOIONIZATION STUDIES OF HYDROGEN-SULFIDE AND ITS DIMER AND TRIMER. II. A ROTATING SOURCE CROSSED MOLECULAR BEAM APPARATUS

Iowa State University PH.D. 1984

PLEASE NOTE:

In all cases this material has been filmed in the best possible way from the available copy. Problems encountered with this document have been identified here with a check mark __√__.

1. Glossy photographs or pages __√__
2. Colored illustrations, paper or print _____
3. Photographs with dark background _____
4. Illustrations are poor copy __√__
5. Pages with black marks, not original copy _____
6. Print shows through as there is text on both sides of page _____
7. Indistinct, broken or small print on several pages _____
8. Print exceeds margin requirements _____
9. Tightly bound copy with print lost in spine _____
10. Computer printout pages with indistinct print _____
11. Page(s) _____ lacking when material received, and not available from school or author.
12. Page(s) _____ seem to be missing in numbering only as text follows.
13. Two pages numbered _____. Text follows.
14. Curling and wrinkled pages _____
15. Other _____

Crossed molecular beam:

I. Photoionization studies of hydrogen sulfide and its dimer and trimer

II. A rotating source crossed molecular beam apparatus

by

Harry Frank Prest

A Dissertation Submitted to the

Graduate Faculty in Partial Fulfillment of the

Requirements for the Degree of

DOCTOR OF PHILOSOPHY

Department: Chemistry
Major: Physical Chemistry

Approved:

Members of the Committee:

Signature was redacted for privacy.

In Charge of Major Work

Signature was redacted for privacy.

Signature was redacted for privacy.

For the Major Department

Signature was redacted for privacy.

For the Graduate College

Iowa State University
Ames, Iowa

1984

TABLE OF CONTENTS

DEDICATION

To my parents, grandparents, family and friends for their boundless love reflected in their unflagging encouragement and unconditional support.

And to my teachers, Paul Harteck, Henry B. Hollinger, Robert R. Reeves, Ernst Seglie, and Robert L. Strong who graciously and patiently encouraged and inspired a much less than promising student.

These precious gifts I will forever treasure.

ACKNOWLEDGEMENTS

Here I can list but a few of the many individuals that I am deeply grateful to for earnestly aiding me in my efforts. My thanks to Roland Struss and Norbert Cent for teaching me mechanical drawing and design and with whom I enjoyed many fruitful discussions. At one time or another, I've benefited from, and now thank, all the members of the Ames Laboratory Research Machine Shops, most especially Jerry Hand, Kent Mogard and Charles Burg. My thanks to Jerry Hand for finding the time and materials required. The majority of the rotating source apparatus was fabricated by Kent Mogard who did the impossible on a regular basis. Charles Burg performed rapid and vac-tight welding on everything from feedthroughs to the beam source chambers. I also greatly appreciate the efforts of the machinists of the ISU Chemistry Machine Shop, Eldon Ness, George Steininger and John Sauke, for taking care of the seemingly omnipresent emergency and "I needed it yesterday" stuff. My thanks to Harold Skank, John Erickson and Darwin Lekwa of the Instrumentation Group for digging up all the parts and constructing all the in-house electronics, especially the controllers and microprocessor. Many thanks to Dr. Harry J. Svec for solving the difficult fiscal problems that made the RSA possible, advising me, and proofing this text. I am deeply indebted to Dr. H. Fritz Franzen for reminding me neither science nor the scientist are one-dimensional. I wish to thank Yoshi Ono, Steve H. Linn, Tzeng Wen-Bih (for "their part in obtaining the H_2S data") and Shao Jian-Dong for sharing the encouraging discussions, frustrations, and absurd situations that have been graduate school.

I will always be grateful for the mechanical talent reflected in the rotating source apparatus which is due to the man who showed me mechanical mastery and allowed me to make the thousands of mistakes necessary to acquire the small portion I possess; Mr. Samuel W. Prest, Sr. (and to Mrs. Maddy F. Prest who made sure each mistake was followed by the proper medical treatment).

GENERAL INTRODUCTION

> To someone who could grasp the
> universe from one unified viewpoint,
> the entire creation would appear as
> a unique fact and a great truth.
>
> J. D'Alembert

The fundamental physical event is the collision; the primary process whereby information is obtained and exchanged. Seeking to understand the general nature of the collision and the participants, the event can be divided phenomenologically into:

1. an initial state
2. an intermediate state
3. a final state.

The diversity of the manifestations and the information contained in the character of the collision event have required the development of numerous theoretical and experimental approaches.

The molecular beam technique allows the preparation and study of unique species in an isolated environment. The singular nature of this environment permits a variety of spectroscopic techniques to be applied to the unperturbed species over relatively long time scales. Originally "simple" effusive sources, such as Knudsen ovens, were exclusively used; primarily due to the ease of maintaining the required vacuum. However, improvements in vacuum technology have allowed implementation of noneffusive sources, such as the supersonic nozzle source, with dramatic increases in the intensity of the collision participant(s) enabling the investigation of even less prominent processes. Further, an ever

increasing array of sensitive and specific detection techniques, each with its own advantages and disadvantages, are bringing more and more detail to our knowledge of molecular processes.

The first part of this thesis examines the ionizing collision of a vacuum ultraviolet (VUV) photon with a molecular species. In general, the number of parameters accessible to experimental control or observation is limited:

1. initial state characteristics - the excitation energy ($\hbar\omega$) delivered to the (state selected) molecular system;
2. intermediate state characteristics - e.g., lifetimes;
3. final state characteristics - energy partitioning, spacial distribution, mass charge, etc.

The complexity of photoionization and subsequent events demands a number of techniques providing complementary information. For example, photoelectron spectroscopy supplies information about the character and energies of ion states while photoionization spectroscopy provides insight into ionization processes. Specifically, this first part illustrates the combination of photoionization mass spectrometry with the supersonic molecular beam technique applied to hydrogen sulfide (H_2S). The mass spectrometric analysis of the positively charged fragments as a function of VUV photon energy yields appearance energies, branching ratios, etc. for various ions and processes. The supersonic molecular beam technique not only provides the required high intensity for the species of interest, but substantially improves energetic resolution by greatly reducing the vibrational and rotational distributions

over those of room temperature. Essentially, this is initial state selection. Additionally, it is possible to synthesize van der Waals clusters (e.g., $(H_2S)_n$, n = 2,3) and observe what are equivalent to very low kinetic energy collisions between state selected or, in an alternate view, the unimolecular decay of a state-selected collision complex.

Part II describes the design of a unique neutral-neutral species crossed molecular beam apparatus - The Rotating Source Apparatus. Again, the general features of the collision accessible experimentally are limited:

1. the initial state - internal energy and velocity;
3. the final state - product identity, angular distribution, energy partitioning, etc.

Although there are valid and convincing arguments that apparatus design can only be optimized on an individual case by case basis, the immense expense and time required make this experimental approach unrealistic. However, to permit incorporation of a variety of diverse experiments and techniques requires a flexible and, therefore, complex apparatus. These conflicting precepts of tailored versus general, simple versus complex, inexpense versus costly, etc. have made the evolution of crossed beam apparati slow but diverse. However, rapidly new "tools", most importantly involving the laser, have become available and attractive. Still, in view of the expense of the construction venture, the prospect of sacrificing previous useful design features is uninviting. With these thoughts in mind, the rotating source apparatus was designed.

Explanation of Thesis Format

The different topics of this thesis allow a clear separation into a Part I concerned with the photoionization studies and a Part II which describes the rotating source apparatus. Part I is broken, after a brief introduction, into two sections each presented in the format of a publication. Part II, although also divided, is formatted to allow a clear presentation of the rotating source apparatus. All references, illustrations, etc. are separated among the two parts to avoid confusion.

PART I. PHOTOIONIZATION OF HYDROGEN SULFIDE AND ITS CLUSTERS

Introduction

Incidence of vacuum ultraviolet (2000 Å - 2 Å) photons on a system of molecular species may produce numerous results: collisional ionization, charge transfer, chemionization, direct photoionization, autoionization, predissociation, ion-pair formation, reradiation, etc. Those processes requiring participation of a third body are largely eliminated by the molecular beam technique. Of the remaining processes, only those leading to positive ions are to be observed here experimentally.

Essentially the experimental arrangement consists of a monochromatic VUV photon beam intersecting a molecular beam at a 90 degree angle and subsequent extraction, sorting by mass-to-charge ratio, and counting of the positive ions formed. The ratio of the ion intensity to the incident photon intensity at a specific wavelength is referred to as the photoionization efficiency (PIE). Most photoionization spectra are presented as the PIE versus the wavelength (in Angstroms).

The most prominent features of the plotted PIE data are due to direct photoionization and autoionization processes. A brief review of these processes, with emphasizing physical insight instead of mathematical thoroughness, will prove helpful.

Direct photoionization

In the dipole approximation for photoabsorption, the cross section for absorption of a photon of polarization $\vec{\lambda}$ and energy $\hbar\omega$ is [1],

$$\sigma = 4\pi^2 \left(\frac{e^2}{\hbar c}\right) \hbar\omega |\langle \Omega | \vec{r} | A \rangle \bullet \vec{\lambda}|^2 \delta(\varepsilon_\Omega - \varepsilon_A - \hbar\omega) \quad .$$

Thus, the initial and final states of the system, labeled A and Ω, of energies ε_A and ε_Ω, respectively, are connected. The term of interest is

$$\langle \Omega | \vec{r} | A \rangle$$

where $\vec{r}$ represents the sum over all individual electron positions, $\vec{r}_j$;

$$\vec{r} \equiv \sum_j \vec{r}_j \quad .$$

In direct photoionization, the final state (Ω) is that of an ion (Φ_Ω^+) and an unbound electron (ψ_ε).

Invoking the Born-Oppenheimer approximation [2] allows the separation of the system states into products of electronic and nuclear wavefunctions,

$$\Phi(\vec{R},\vec{r}) = \Psi(\vec{r};\vec{R})X(\vec{R})$$

where $\vec{R}$ indicates the nuclear coordinates. Reexamining the matrix element,

$$\langle \Omega^+ | \vec{r} | A \rangle = \langle \Phi_\Omega^+(\vec{R},\vec{r})\psi_\varepsilon | \vec{r} | \Phi_A(\vec{R},\vec{r}) \rangle$$

$$= \langle \Psi_\Omega^+(\vec{r};\vec{R})X_\Omega^+(\vec{R})\psi_\varepsilon | \vec{r} | \Psi_A(\vec{r};\vec{R})X_A(\vec{R}) \rangle \quad .$$

Taking advantage of the fact that $\vec{r}$ operates only on the electronic wavefunctions, the matrix element can be rewritten

$$e\langle\Omega^+|\vec{r}|A\rangle = \langle X_\Omega^+(\vec{R})\{\Psi_\Omega^+\psi_\varepsilon|e\vec{r}|\Psi_A\}X_A(\vec{R})\rangle$$

$$\equiv \langle X_\Omega^+(\vec{R})|\vec{M}(\vec{R},\varepsilon)|X_A(\vec{R})\rangle \quad .$$

The electric dipole transition moment, $\vec{M}(\vec{R},\varepsilon)$, is a function of the internuclear distances, $\vec{R}$, and the continuum wavefunction of the unbound electron. Assuming $\vec{M}(\vec{R},\varepsilon)$ to be independent of $\vec{R}$ is the Franck-Condon (F.C.) approximation. Because most spectroscopy involves the ground state, the transition moment is evaluated for the equilibrium nuclear configuration; $\vec{R} = \vec{R}_{eq}$. Therefore, the photoionization cross section becomes proportional to the product of two terms which can be considered separately;

$$\sigma_{F.C.} \propto |\langle X_\Omega^+|X_A\rangle|^2 \; |\vec{M}(\vec{R}_{eq},\varepsilon)|^2 \quad .$$

(At this point, the mathematical orchestra has been arranged and may be played for physical insight.)

Assume the transition involves strictly a single electron, labeled i, which occupied the one electron bound orbital ψ_A in the ground state and upon ionization the bound state ψ_ε, then the transition moment would become

$$\vec{M}(\vec{R}_{eq}) \propto \langle\psi_\varepsilon(\vec{r}_i)|\vec{r}_i|\psi_A(\vec{r}_i)\rangle \quad .$$

One sees that because the ground state wavefunction is localized, the asymtotic region of the continuum wavefunction is not of interest. Further assume, for ease of visualization, the atomic case of ionization of a bound 2p electron to an unbound state of d angular

momentum. The 2p radial wavefunction is nodeless and positive, and near threshold (i.e., $\varepsilon \sim 0$), the first node of the d wavefunction is also positive near the origin. Therefore, the matrix element is positive and fairly large. However, as the kinetic energy (ε) of the free electron increases above threshold, the wavelength of the departing electron decreases bringing in nodes and loops causing cancellation and reducing the matrix element. Consider now ionization from a 3p orbital into a d continuum state. Because the 3p wavefunction has a node and at its maximum is negative, the matrix element is negative near threshold. Again as ε increases, cancellation occurs and the matrix element becomes increasingly positive and eventually changes sign. At one point, the matrix element passes through zero and the cross section displays a "Cooper Minumum" [3]. Because the wavelength changes slowly with ε, this general behavior of the cross section is exhibited over several Rydbergs or hundreds of Angstroms above threshold.

If one simultaneously addressed the possibility of the transition $np \rightarrow \varepsilon s$ versus $np \rightarrow \varepsilon d$, consideration of the effective potential, which is strongly dependent on the angular momentum, would complicate matters. The presence of the centrifugal barrier can prejudice ionization according to the angular momentum ℓ due to the inability of the higher ℓ state to penetrate [4,5]. In the molecular case (e.g., CO_2 and N_2 [6]), these barrier effects manifest themselves as "shape resonances" which are several eV broad.

Returning to consider the first term in the cross section expression $\sigma_{F.C.}$, and neglecting interaction between vibration and rotation,

one can separate the nuclear states into products of vibrational (χ) and rotational (θ) wavefunctions:

$$\langle \chi_{\Omega}^{+} | \chi_{A} \rangle = \langle \chi_{\Omega}^{+} \theta_{\Omega}^{+} | \chi_{A} \theta_{A} \rangle \quad .$$

Ignoring the rotational contribution [7], $\sigma_{F.C.}$ becomes proportional to the square of the overlap integral of the vibrational wavefunctions referred to as the Franck-Condon factor;

$$\sigma_{F.C.} \propto |\langle \chi_{\Omega}^{+} | \chi_{A} \rangle|^{2} \quad .$$

This again emphasizes the "vertical" nature inherent in the Franck-Condon approximation in that the value of the overlap integral is determined by the oscillation of the upper state vibrational wavefunction χ_{Ω}^{+} directly above the ground state wavefunction χ_{A}. Therefore, the relative positions of the potentials and their shapes are important. (This concept and the following arguments are most easily envisioned for the diatomic case.)

In ionization, the bonding, antibonding, or nonbonding character of the removed electron is manifest in the shift, and the change in depth and curvature of the upper ionized state potential from that of the ground state. The potential curvature and depth influence the rate of oscillation of the wavefunction as well as the level spacing and are held as being of secondary importance relative to the effect of well displacement on the overlap integral. For instance, removal of a nonbonding electron leaves the position of the upper potential unchanged. Thus, the F.C. factor favors the transition from the ground vibrational

state of the neutral to the ground vibrational of the ion, $\chi_A(0) \rightarrow \chi_\Omega^+(0)$, over all others. The energy at which this occurs is termed the adiabatic ionization energy. Removal of a bonding or an antibonding electron shifts the ion potential and, in general, the most favored overlap will take place between some other final ion vibrational state, $\chi_A(0) \rightarrow \chi_\Omega^+ (V\neq 0)$. This most probable transition occurs at the vertical ionization energy. In the simple diatomic case, the "classic" example is NO [8], which reflects this F.C. picture in the step-like structure of the PIE curve with the height of each step proportional to the F.C. factor.

Autoionization

Each rovibronic state of a molecular ion can be the ionization limit for a series of discrete, electronically bound states. The physical basis for these Rydberg series is the quasi-hydrogenic situation of a single, highly excited electron about an ionic core. For those states above the first ionization limit, coupling to continuum states is energetically possible and the subsequent formation of an ion and unbound electron is termed autoionization. This process is viewed as occurring in two steps; photoexcitation from the initial state A to the discrete state Ω^* followed by autoionization to produce the ionic state Ω^+. In terms of Fermi's Golden Rule [9], the autoionization rate becomes

$$k_a = \frac{2\pi}{\hbar} |\langle \Omega^+ | W | \Omega^* \rangle|^2 \rho(\varepsilon(\Omega^+)) \quad .$$

Because various interactions, W, are possible, various types of autoionization take place. Where the source of interaction is electron-

electron repulsion, the autoionization is termed electron. Perturbation by nuclear motions are ascribed to either vibrational or rotational autoionization. The general theory of electronic autoionization of Fano [10] has been vigorously developed [11,12,13] and applied to autoionization resonances (line shapes) in photoionization spectra (e.g., [14,15]).

The coupling of nuclear and electronic motion represents the breakdown of the Born-Oppenheimer (BO) approximation. Guided by the adiabatic principle, on which the BO approximation is founded, one can gauge where to expect this failure. Consider the diatomic molecule NO for which the average vibrational spacing $\overline{\Delta\varepsilon_v}$ of the $(X^1\Sigma^+)$ ion is 0.286 eV [16]. The period, τ_n, of an electron in a Bohr orbit of quantum number n is

$$\tau_n = (1.52 \times 10^{-16}\ s)n^3 \quad .$$

The adiabatic principle can be formulated in terms of the Massey parameter, $\omega_v\tau_n$, and one expects coupling for

$$\omega_v\tau_n = \left(\frac{\overline{\Delta\varepsilon_v}}{\hbar}\right)\tau_n \lesssim 1 \quad .$$

This implies for $n \lesssim 8$, coupling between vibrational and electron motion should be highly probable. Series assignments on the first four vibrational steps of the NO PIE curve show for $n < 8$, <u>multiple</u> changes in vibrational quantum number v are common. However, for $n > 8$, vibrational changes follow the $\Delta v = -1$ propensity rule developed by Berry [17].

Rotational considerations can be similarly cast, however, it must be remembered that the adiabatic principle does not argue for a particular mechanism (i.e., electronic, vibrational, or rotational autoionization), the elucidation of which requires detailed theoretical considerations.

References

1. G. Baym, Lectures on Quantum Mechanics (Benjamin/Cummings Publishing Co., Reading, MA, 1972), p. 286.
2. M. Born and R. Oppenheimer, Ann. Physik 84, 457 (1927).
3. J. W. Cooper, Phys. Rev. 128, 681 (1962).
4. S. T. Manson and J. W. Cooper, Phys. Rev. 165, 126 (1968).
5. J. L. Dehmer, A. F. Starace, V. Fano, J. Cugar and J. W. Cooper, Phys. Rev. Lett. 26, 1521 (1971).
6. J. L. Dehmer and D. Dill, Phys. Rev. Lett. 35, 213 (1975).
7. G. Herzberg, Molecular Spectra and Molecular Structure. I. Spectra of Diatomic Molecules (Van Nostrand Reinhold Co., New York, 1966), p. 203.
8. Y. Ono, S. H. Linn, H. F. Prest, M. E. Cress and C. Y. Ng, J. Chem. Phys. 73, 2523 (1980).
9. G. Baym, Lectures on Quantum Mechanics (Benjamin/Cummings Publishing Co., Reading, MA, 1972), p. 251.
10. U. Fano, Phys. Rev. 124, 1866 (1961).
11. F. H. Mies, Phys. Rev. 175, 164 (1968).
12. J. N. Bardsley, Chem. Phys. Lett. 2, 329 (1968).
13. A. L. Smith, Philos. Trans. R. Soc. London Sec. A 268, 169 (1970).
14. J. H. D. Eland, J. Berkowitz and J. E. Monahan, J. Chem. Phys. 72, 253 (1980).

15. S. H. Linn, Ph.D. dissertation, Iowa State University, Ames, Iowa, 1982.

16. Y. Ono, Ph.D. dissertation, Iowa State University, Ames, Iowa, 1982.

17. R. S. Berry, J. Chem. Phys. 45, 1228 (1966).

SECTION I. MOLECULAR BEAM PHOTOIONIZATION STUDY OF H_2S

Introduction

The H_2S^+ ions have been the subject of many experimental studies by means of photoelectron spectroscopy [1-10] absorption [11-16] and emission spectroscopy [6,17] electron impact [18-20], and photoionization mass spectrometry [16,21-23]. The detailed analyses [6,24] of the high resolution emission spectrum of H_2S^+ obtained by Horani et al. [17] and the high resolution photoelectron study of Karlsson et al. [10] have provided considerable information about the potential energy surfaces of the $\tilde{X}^2B_1$, $\tilde{A}^2A_1$, and $\tilde{B}^2B_2$ states of H_2S^+. The recent ab initio calculation [25,26] of a correlation diagram for these three doublet and lowest quartet electronic states of H_2S^+ has also been able to provide a rationalization for the dissociation mechanisms of H_2S^+ observed in the studies by photoionization mass spectrometry [22] and photoelectron photoion coincidence spectroscopy [27]. By contrast, information concerning Rydberg states converging to the three lowest doublet states of H_2S^+ is less abundant. Previous absorption studies [11-16] mostly concentrated on investigations of Rydberg states below the ionization energy (IE) of H_2S^+. To our knowledge, the nature of Rydberg levels located above the IE of H_2S which converge to the $\tilde{A}^2A_1$ and $\tilde{B}^2B_2$ state of H_2S^+ has not been explored previously.

The photoionization efficiency (PIE) curves for H_2S^+ obtained by Dibeler and Liston [22] and Walters and Blais [23] clearly reveal rich autoionizing Rydberg structures in the region 650-1190 Å. In order to

examine these autoionizing Rydberg features in details, we have performed a higher resolution photoionization mass spectrometric study of H_2S using the molecular beam method. This report presents the results and an analysis of our experiment. The PIE spectra for $(H_2S)_2^+$, $(H_2S)_3^+$, and their fragments have also been obtained. The analysis of the dimer and trimer systems will be discussed in Section II.

Experimental

The experimental arrangement and procedures were essentially the same as that described previously [28]. Briefly, the apparatus, shown schematically in Figure 1, consists of a 3 meter near-normal incidence vacuum ultraviolet (VUV) monochromator (McPherson 2253M), a supersonic molecular beam production system, a capillary discharge lamp, a VUV light detector, and a quadrupole mass spectrometer for ion detection. The grating employed in this study was a Bausch and Lomb 1200 lines mm^{-1} MgF_2-coated aluminum grating blazed at 1360 Å. Depending on the wavelength region, the hydrogen many-lined pseudocontinuum, the argon continuum, or the helium Hopfield continuum was chosen as the light source.

The hydrogen sulfide was a commercial product (Matteson Gas Products, Joliet, IL 60434) with a quoted purity of ≥99.6%. The H_2S molecular beam was produced by supersonic expansion through a 120 μm diameter stainless steel nozzle at a nozzle temperature of ∿290 K and a stagnation pressure of ∿520 Torr. The arrangement is diagrammed in Fig. 2.

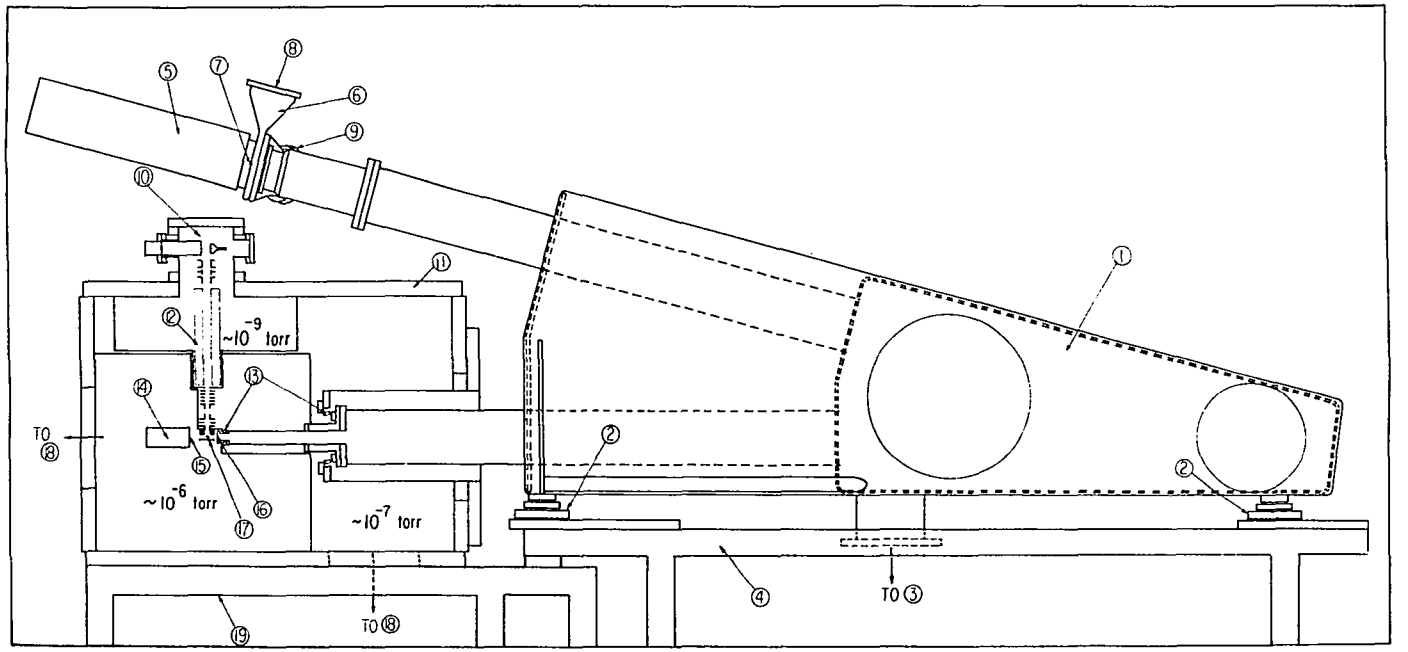

Figure 1. Side view of the photoionization apparatus. (1) monochromator, (2) X-Y translational bench, (3) liquid nitrogen trapped 6 in. diffusion pump, (4) monochromator stand, (5) light source, (6) differential pumping arm, (7) entrance slit, (8) to Roots blower pumping system, (9) to ejector pump, (10) Daly type particle detector, (11) scattering chamber, (12) quadrupole mass spectrometer, (13) flexible coupling bellows, (14) photon detector, (15) sodium salicylate coated quartz window, (16) exit slit, (17) photoionization center, (18) 10 in. diffusion pump system, and (19) stand for scattering chamber

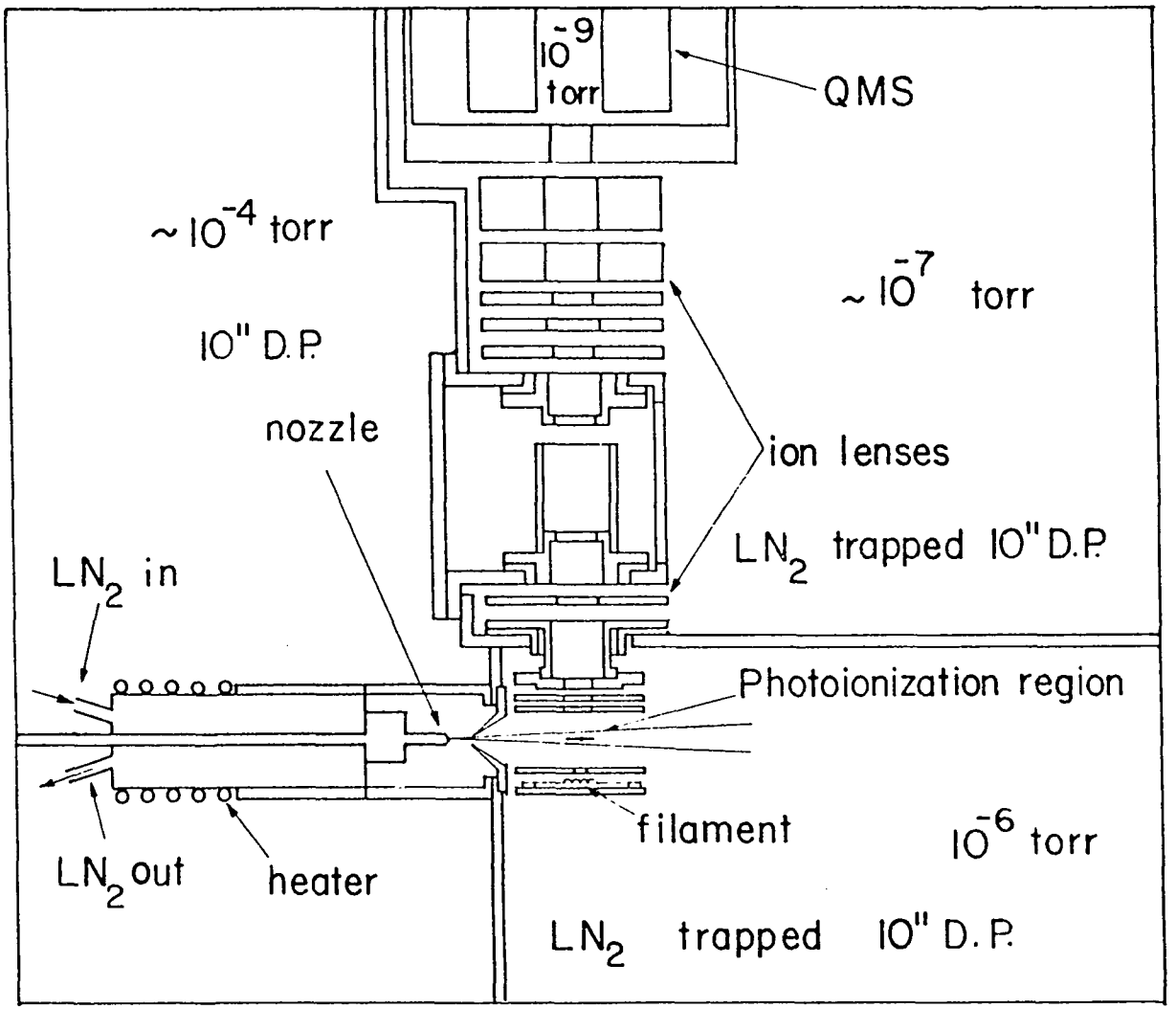

Figure 2. Cross sectional view of the differential pumping arrangement of the molecular beam production system, ionization region, ion optics, and quadrupole mass spectrometer

The wavelength resolutions used in this study were 1.4 Å and 0.14 Å (FWHM). Typical counting times were 6 s, and ion counts of H_2S^+, accumulated at each point in the high resolution (0.14 Å FWHM) study, were ≥8000 counts. The counting rate for H_2S^+, observed in the low resolution (1.4 Å FWHM) experiment, was usually two orders of magnitude greater than that in the high resolution study. Depending on the wavelength resolutions used, data were plotted at intervals of 0.05, 0.1, 0.25, or 0.5 Å. The PIE data for S^+ and HS^+ from H_2S were obtained only with a wavelength resolution of 1.4 Å and were plotted at intervals of 0.25 Å. Wavelength calibrations were made by using appropriate known atomic resonance lines, or H_2 emission lines when the H_2 pseudocontinuum was used [29].

Results and Discussion

Figures 3(a) and (b) show the PIE curves (1.4 Å FWHM) for H_2S^+ in the regions 948-1190 and 645-995 Å obtained by using the hydrogen many-lined pseudocontinuum and the helium Hopfield continuum, respectively. We found excellent agreement between the PIE data recorded in the overlapping 948-995 Å using the two light sources. The high resolution PIE curves for H_2S^+ in the regions 954-996 and ∿768-900 Å obtained using a wavelength resolution of 0.14 Å (FWHM) and the helium Hopfield continuum are shown in Figs. 4 and 5, respectively. The data points which were found to be affected by strong atomic resonance lines superimposed on the helium Hopfield continuum were excluded in the figures. The comparison between the high and low resolution spectra shows that a wavelength resolution of 1.4 Å (FWHM) is sufficient to resolve essentially

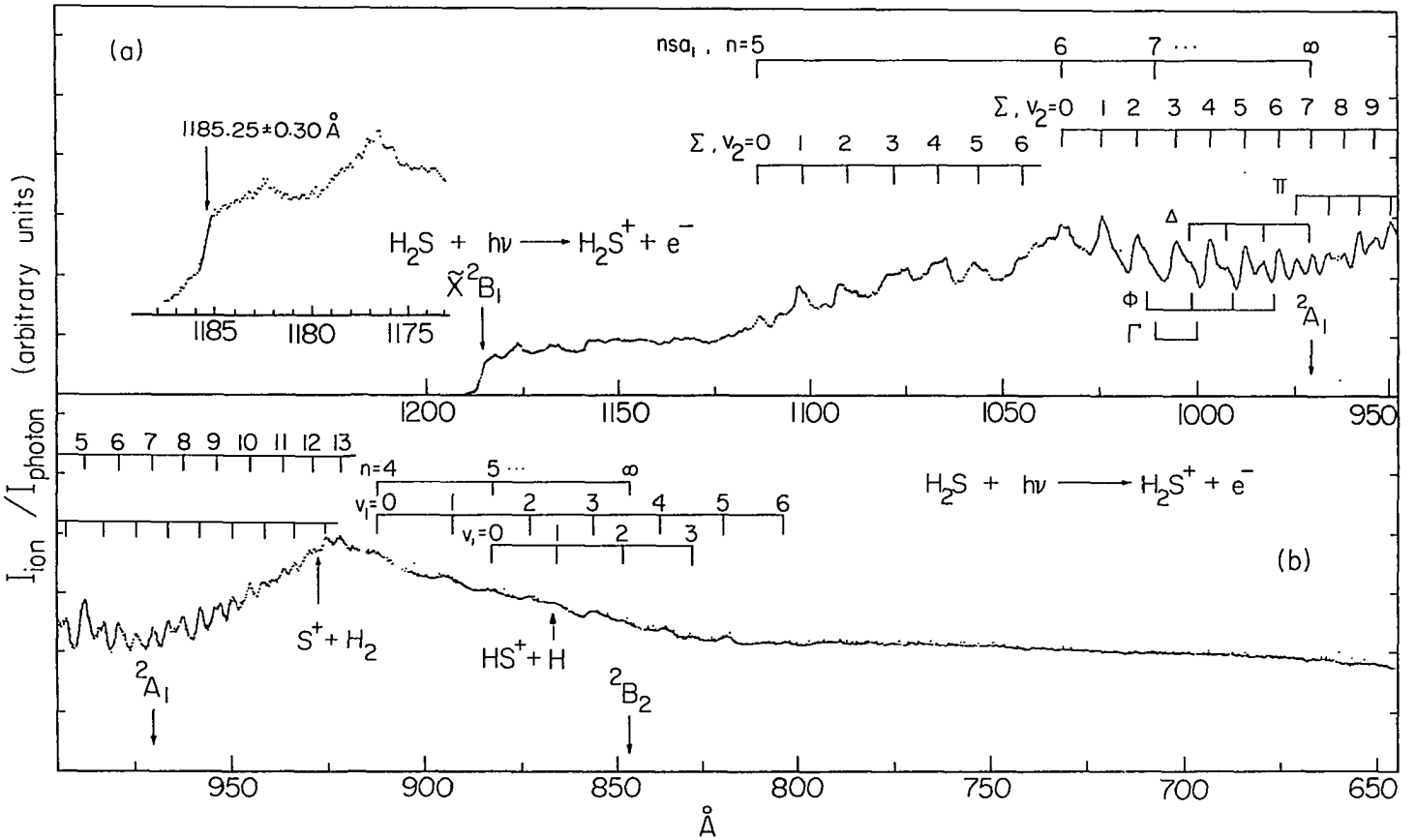

Figure 3. PIE curve for H_2S^+ in the region 645-1190 Å. (a) PIE curve (1.4 A FWHM) for H_2S^+ in the region 948-1190 Å obtained using the hydrogen many-lined pseudocontinuum as the light source; (b) PIE curve (1.4 Å FWHM) for H_2S^+ in the region 634-995 Å obtained using the helium Hopfield continuum as the light source

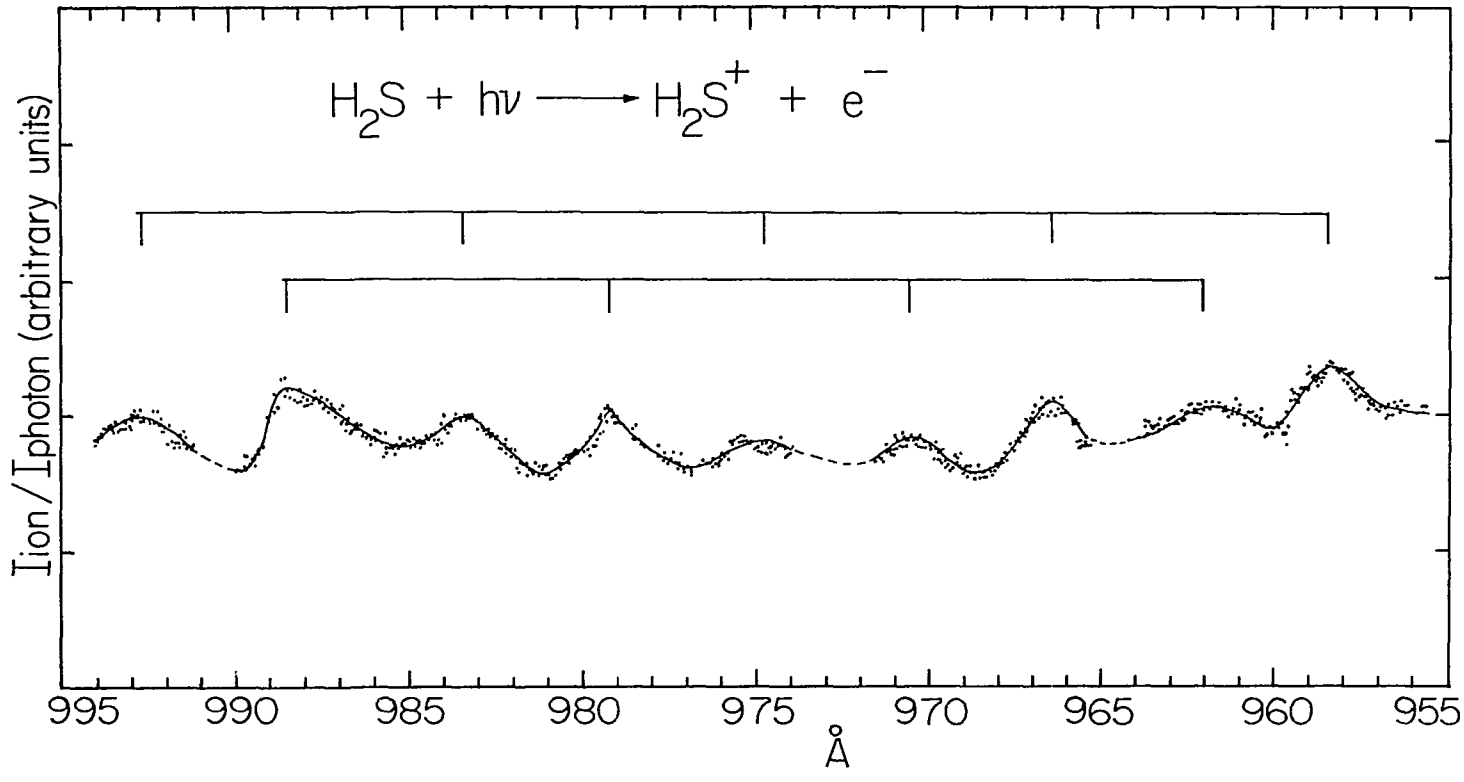

Figure 4. High resolution (0.14 Å FWHM) PIE curve for H_2S^+ in the region 954-996 Å

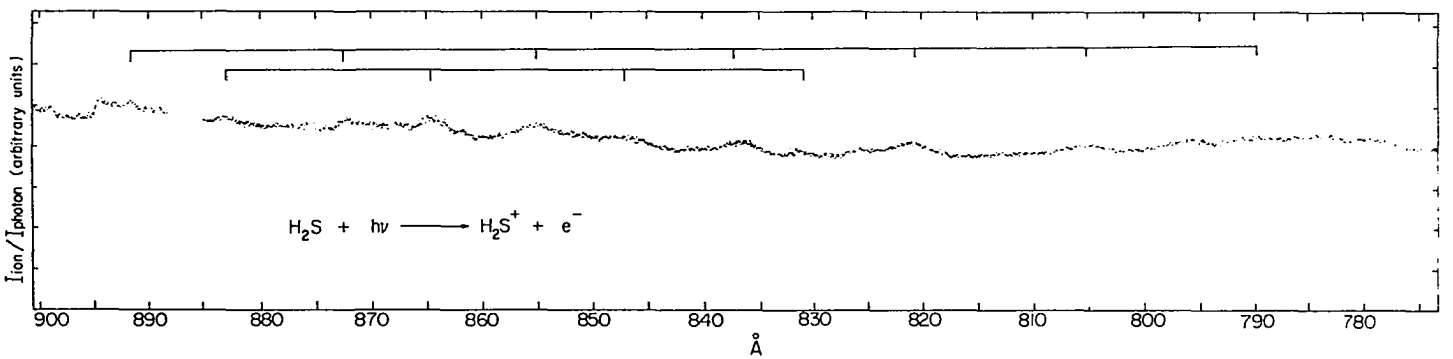

Figure 5. High resolution (0.14 Å FWHM) PIE curve for H_2S^+ in the region 768-900 Å

all autoionizing Rydberg structures. A high resolution (0.14 Å FWHM) PIE curve for H_2S^+ in the region 1070-1190 Å was also measured by using the argon continuum. Since this high resolution curve reveals no new structures other than those appearing in the low resolution spectrum, only a section (1173-1188 Å) of the resolution data for H_2S^+ near the threshold was plotted in Fig. 3(a) to show the ionizing threshold behavior for H_2S in more detail.

In the one-electron approximation, the ground state electronic configuration for H_2S is $(1a_1)^2(2a_1)^2(1b_2)^2(3a_1)^2(1b_1)^2(4a_1)^2(2b_2)^2(5a_1)^2$ x $(2b_1)^2\tilde{X}^1A_1$. Upon ionization from the $2b_1$, $5a_1$, and $2b_2$ valence orbitals, the ionic states formed are the $\tilde{X}^2B_1$, $\tilde{A}^2A_1$, and $\tilde{B}^2B_2$ states, respectively. The adiabatic ionization energies for the $\tilde{X}^2B_1$ (10.466 eV), $\tilde{A}^2A_1$ (12.777 eV), and $\tilde{B}^2B_2$ (14.643 eV) states of H_2S^+ determined by photoelectron spectroscopy [10] are indicated by arrows in the PIE curves for H_2S^+ in Figs. 3(a) and (b). No apparent structure correlating to the onsets of these states can be seen, with the exception of that for the $\tilde{X}^2B_1$ states, where a sharp step-like feature was found. The position of this step was located at 1185.3 ± 1.5 Å in the low resolution PIE curve for H_2S^+ (Fig. 3(a)).

The high resolution (0.14 Å FWHM) spectrum for H_2S^+ near the threshold shows that the PIE for H_2S^+ decreases rapidly in the interval of 1184.95-1185.55 Å and then tails away more gradually toward longer wavelengths. There seems to be a break or change in slope between the tailing structure and the rapidly rising step. The tailing structure found here is similar to that observed in the C_2H_2 system [30], but more

severe than those observed in other triatomic molecular systems [28,31, 32]. It is possible that this substantial tailing structure is indicative of higher rotational temperatures in the H_2S beam than those attained on other triatomic molecular systems such as CS_2 [28], OCS [31], and SO_2 [32] which have smaller rotational quanta than that of H_2S. The other possible mechanism which can give rise to H_2S^+ below the IE of H_2S is field ionization of H_2S in very high Rydberg states. Since the rotational and vibrational temperatures of H_2S after the supersonic expansion are likely to be different, it is difficult to make a quantitative analysis of the threshold and estimate the contributions to this tailing structure from different rotational and vibrational degrees of freedom. Assuming the tailing structure to be hot bands, the midpoint of the rapidly rising step at 1185.25 Å has been taken to be the IE of the $\tilde{X}^2B_1$ state of H_2S. Based on this assumption, the uncertainty of the IE, which is derived from the wavelength span of the rapidly rising step, is ±0.3 Å.

The value of 10.4607 ± 0.0026 eV (1185.25 ± 0.30 Å) for the IE for the $\tilde{X}^2B_1$ state of H_2S^+ determined here was found to be slightly lower than the values of 10.466 ± 0.002 eV determined by Karlsson et al. [10] in a high resolution photoelectron measurement and by Masuko et al. [15] in a photoabsorption study. This slight difference may arise partly from higher rotational temperatures of H_2S in the latter studies. Karlsson et al. [10] note that the photoelectron spectrum of the vibrational band corresponding to the 0-0 transition to the $\tilde{X}^2B_1$ state has a

conspicuous shape. A comparison of values for the IE of H_2S^+ obtained previously by various methods can be found in Table I of Ref. 23.

It is obvious that the PIE curve for H_2S^+ is dominated by autoionizing vibrational structures. Stemming from the fact that the $\tilde{A}^2A_1$ and $\tilde{B}^2B_2$ states are the only ionic states lying in this energy range and that the IE of the next higher ionic state ($\tilde{C}^2A_1$) is 22 eV (564 Å), it is logical to assume that the autoionizing Rydberg states in the region ~800-1190 Å are members of Rydberg series converging to the $\tilde{A}^2A_1$ and $\tilde{B}^2B_2$ states.

Spectrum of H_2S^+ in the 1040-1190 Å region

The structures observed in this region are also discernible in the PIE curve and absorption spectrum of H_2S obtained previously by Watanabe and Jursa [16]. They show that only ~30-60% of the molecules, after absorbing photons in this region, will lead to dissociation. Thus, the diffuse autoionizing features appearing in this portion of the PIE spectrum may be ascribed to autoionization as well as predissociation. The weak peak at 1182.2 Å was found to coincide with the member (n = 7) of the DD'E Rydberg series [15] converging to the vibrationally excited $\tilde{X}^2B_1$ (1,0,0) state of H_2S^+ at 1151 Å (10.722 eV) identified by Masuko et al. [15] in an absorption study. However, a search for the higher members of this series was unsuccessful.

At wavelengths shorter than 1114 Å, more pronounced features were found. The shapes of these structures are irregular and many of these bands appear to be double peaking. The positions of the centers of

these autoionizing bands are listed in Table 1. The average vibrational spacing ($\Delta\nu_{av}$) of this progression is 982 cm^{-1}. Since this value is close to the ν_2 vibrational frequency ($\sim$900 cm^{-1}) [2,5,7,24] of the $\tilde{A}^2A_1$ state of H_2S^+, this autoionizing progression is considered to originate from a member of a Rydberg series converging to the $\tilde{A}^2A_1$ state. The vibronic structure of the $5a_1$ photoelectron band was found to have a complex pattern [10] which has been attributed to the effect of the Renner-Teller vibronic interaction [6,24]. Thus, the band structure cannot be assigned only in terms of the vibrational quantum number ν_2; the splittings of the vibrational energy levels due to different angular momenta (K) must also be considered. The assignment [10] of the individual structures of the $5a_1$ photoelectron band was based on a comparison with the electronic emission spectrum of H_2S^+, which, in turn, has been interpreted by comparison to extensive theoretical calculations [24]. The assignments of autoionizing Rydberg structures observed here follows the assignment of the $5a_1$ photoelectron band by Karlsson et al. [10]. In view of the fact that the first few strong peak-like structures in the $5a_1$ photoelectron band can be correlated with the Σ-bands of the ν_2 vibrational mode, and that the splittings of the autoionizing vibrational bands observed in this region are not unambiguously identified, this autoionizating vibrational progression was fitted into the Rydberg equation using the IEs of the (ν_2,Σ)-bands of the $\tilde{A}^2A_1$ state as the convergence limits. Assuming 89847 cm^{-1} (1113 Å) to be the origin of the 0-0 transition, the average value for the effective principal quantum number (n^*) was found to be 2.909. Since the approximate quantum

Table 1. Progression of vibrational bands of H_2S in the region 1040-1120 Å

Rydberg state	$\tilde{A}^2A_1$ state of H_2S^+	Term values[c]	n*	Assignment[b]	
$\nu_n(cm^{-1})$[a]	$\nu_\infty(cm^{-1})$[b]	(cm^{-1})		ν_2	K
89847	103053	13206	2.883	0	Σ
90744	103972	132228	2.880	1	Σ
91743	104900	13157	2.888	2	Σ
92851	105803	12952	2.911	3	Σ
93853	106666	12813	2.927	4	Σ
94742	107497	12755	2.933	5	Σ
95740	108408	12668	2.943	6	Σ
	Average	12968	2.909		
$\Delta\nu_{av}$=982	$\Delta\nu_{av}$=891				

[a]The positions of the centers of autoionizing vibrational bands.

[b]Reference 10.

[c]The term value is equal to $\nu_\infty - \nu_n = R/n^{*2}$, where R (=109736 cm^{-1}) and n* are the Rydberg constant for H_2S and the effective principal quantum number, respectively.

defects δ in Rydberg series of the free atomic sulfur are δ = 2.0 for ns, 1.6 for np, and 0.3 for nd orbitals [33], it is most likely that this Rydberg state involves an s-type orbital having a quantum defect δ = 2.09 and this discrete structure can be tentatively assigned to the $5a_1 \rightarrow 5sa_1$ transition. We note that a Rydberg absorption feature which was assigned to be $2b_1 \rightarrow 5sa_1$ transition and has an effective principal quantum number of 2.89 was reported by Masuko et al. [15].

Spectrum of H_2S^+ in the range 920-1040 Å

The broad structure at ~1037 Å seems to separate the vibrational progressions on the low and high energy sides with quite different peak shapes. The average spacing of the vibrational bands found on the high energy side is approximately 900 cm^{-1}, which is lower than that of the vibrational bands in the region 1040-1120 Å by ~80 cm^{-1}. It is possible that the irregular shape of the structure at ~1037 Å results from the extensive overlap of autoionizing vibrational bands originating from two different progressions. According to the study of Masuko et al. [15], the effective principal quantum number for the $2b_1 \rightarrow 6sa_1$ transition is equal to 4.10. If the $5a_1 \rightarrow 6sa_1$ transition has a similar n* value, the origin of the 0-0 transition of this Rydberg transition is predicted to be at ~1036 Å. Interestingly, in a close examination, the pattern of autoionizing peaks in the region 925-1040 Å was found to be similar to that of the $5a_1$ photoelectron band. That is, after a series of regularly spaced peaks, the spacing becomes irregular and changes to a series of peaks with approximately half the initial spacing. These

observations are taken as evidence that the autoionizing vibrational progression observed in this region originates from a new Rydberg state which is similar in structure to that of the $\tilde{A}^2A_1$ state.

The positions of the autoionizing peaks resolved in this region are listed in Table 2 and fit to the Rydberg equation using the IEs of the the $\tilde{A}^2A_1$ (ν_2,K) states as the convergence limits. Assuming the peak at 1033.5 Å to be the origin of the 0-0 transition of this progression, the average value for n* was found to be 4.124. The good agreement between the latter n*-value and that of the $2b_1 \rightarrow 6sa_1$ transition indicates that the discrete structure appearing in this region belongs to the member (n = 6) of the Rydberg transitions $5a_1 \rightarrow nsa_1$. Similar Rydberg transitions, $3a_1 \rightarrow nsa_1$, were assigned to a Rydberg series of H_2O by Wang et al. [34] in a photoabsorption measurement. Although many of the peaks corresponding to the Δ-, ϕ-, and Γ-bands have not been resolved, the expected positions of these bands, based on the assignment of the $5a_1$ photoelectron band by Karlsson et al. [10], are also indicated in Fig. 3(a) to illustrate the similarity of the pattern of autoionizing peaks in this region and those peaks observed in the high resolution photoelectron spectrum of H_2S.

Spectrum of H_2S^+ in the region 645-920 Å

Above the IE for the $\tilde{A}^2A_1$ state, the PIE for H_2S^+ increases gradually until, at approximately 926 Å, a sharp break appears in the spectrum and the PIE for H_2S^+ starts to decrease towards higher photon energies. As shown in Fig. 3(b), the break found in the spectrum is in

Table 2. Progression of vibrational bands of H_2S in the region 910-1040 Å

Rydberg state	$\tilde{A}^2A_1$ state of H_2S^+	Term values[c]	n*	Assignment[b]	
$\nu_n(cm^{-1})$[a]	$\nu_\infty(cm^{-1})$[b]	(cm^{-1})		ν_2	K
96759	103053	6294	4.176	0	Σ
97704	103972	6268	4.184	1	Σ
98570	104900	6329	4.164	2	Σ
99552	105803	6251	4.190	3	Σ
99701[d]	106029 106166	6397[e]	4.141	3 3	Δ ϕ
100452	106666	6214	4.202	4	Σ
100746[d]	106868 107142	6259[e]	4.187	4 4	Δ ϕ
101235	107497	6262	4.186	5	Σ
101698	107844[f]	6146	4.226	5	Δ
102124	108408	6284	4.179	6	Σ
102638	108780	6142	4.227	6	Π
103040	109328	6288	4.178	7	Σ

[a]The peak positions of autoionizing vibrational bands.

[b]Reference 10.

[c]The term value is equal to $\nu_\infty - \nu_n = R/n^{*2}$, where R (=109736 cm^{-1}) and n* are the Rydberg constant for H_2S and the effective principal quantum number, respectively.

[d]Shoulders or broad peaks.

[e]These term values are calculated by using the average values of the (ν_2,Δ) and (ν_2,Δ) states as the convergence limits.

[f]Uncertain assignment, see Reference 10.

Table 2. (continued)

Rydberg state	$\tilde{A}^2A_1$ state of H_2S^+	Term values[c]	n*	Assignment[b]	
$\nu_n(cm^{-1})$[a]	$\nu_\infty(cm^{-1})$[b]	(cm^{-1})		ν_2	K
103477	109771	6294	4.176	7	Π
103950	110247	6297	4.174	8	Σ
104341	110788	6447	4.126	8	Π
104822	111312	6490	4.112	9	Σ
105263	111893	6630	4.068	9	Π
105764	112393	6629	4.069	10	Σ
106213[d]	112965	6752	4.031	10	Π
106769	113482	6713	4.043	11	Σ
107664	114030	6366	4.152	11	Π
107643[d]	114595	6952	3.973	12	Σ
107991	115151	7160	3.915	12	Π
108460	115700	7240	3.893	13	Σ
	Average	6463	4.124		

close correspondence with the onset (927 Å) for the fragmentation of H_2S to form $S^+ + H_2$. The onset (867 Å) for the fragment channel $HS^+ + H$ is also indicated in the figure. The strong predissociation of H_2S^+ to form S^+ and HS^+ in the main cause for the broadening of autoionizing structures appearing in the region 780-920 Å. The PIE curve in the region 645-780 Å is essentially structureless.

Since the broad structures in this region are located at energies higher than the IE for the $\tilde{A}^2A_1$ state, it is most likely that they originate from members of Rydberg series converging to the B^2B_2 state at 14.643 eV. The positions of these autoionizing bands are listed in Table 3. A simple inspection shows that these structures can be grouped into two progressions which are designated as Progression I and II here. The average vibrational spacings for Progression I and II are 2427 and 2405 cm^{-1}, respectively. These values are found to be in between the ν_1 vibrational frequency (2615 cm^{-1}) [35] of H_2S in the $\tilde{X}^1A_1$ state and that of the H_2S^+ ($\sim$2257 cm^{-1}) [10] in the $\tilde{B}^2B_2$ state. Assuming that the positions at 913.1 and 844 Å correspond to the 0-0 vibrational band origins, the effective principal quantum numbers for Progressions I and II are deduced to be 3.58 and 4.69, respectively. For the principal quantum numbers n to be equal to 4 and 5, the corresponding values for the quantum defects are 0.42 and 0.31. Again, based on the comparison of these values with δ-values in the Rydberg series of free atomic sulfur, the Rydberg orbitals are likely to be d-type orbitals. In a previous photoabsorption study of H_2S, Masuko et al. [15] also identified the $2b_1 \rightarrow nda_1$ Rydberg series having a value of $\sim$0.339 for the quantum

Table 3. Progressions of vibrational bands H_2S in the region 645-920 Å

Progression I				Progression II			
ν_1[a]	$\nu(cm^{-1})$[b]	$\Delta\nu(cm^{-1})$	n*	ν_1[a]	$\nu_n(cm^{-1})$[b]	$\Delta\nu$	n*
N=4 0	109517		3.58	n=5 0	113122		4.69
		2465				2552	
1	111982			1	115674		
		2631				2459	
2	114613			2	118133		
		2346				2204	
3	116959			3	120337		
		2515					
4	119474					$\Delta\nu_{av}$=2405	
		2329					
5	121803						
		2343					
6	124146						
		2356					
7	126502						
		$\Delta\nu_{av}$=2427					

[a]See text for the assignments of n and ν_1.

[b]The positions of the centers of autoionizing vibrational bands.

defect. Therefore, we prefer the assignments of $2b_2 \rightarrow 4da_1$ and $2b_2 \rightarrow 5da_1$ for Progressions I and II, respectively[1].

Absolute photoionization cross sections for H_2S^+, S^+, and HS^+ formations

The PIE curves for S^+ and HS^+ obtained with a wavelength resolution of 1.4 Å (FWHM) are shown in Figs. 6(a) and (b), respectively. These spectra are in good agreement with those obtained by Dibeler and Liston [22]. The onsets for the S^+ and HS^+ formations from H_2S were determined to be 13.375 ± 0.022 and 14.300 ± 0.024 eV, respectively, values which are also consistent with those reported previously. Weak autoionizing vibrational structures similar to those of Progressions I and II observed in the PIE curve for H_2S^+ are also discernible in the PIE spectra for S^+ and HS^+. In a photoelectron-photoion study, Eland [27] concluded that dissociation from the $\tilde{B}^2B_2$ state of H_2S^+ produces mainly or exclusively HS^+. The observation that the PIE curve for S^+ shows no increase beyond the IE for the $\tilde{B}^2B_2$ state is in conformity with the above conclusion.

The absolute photoionization cross sections for the formation of H_2S^+ ($\sigma_i(H_2S^+)$) in the region from the ionizing threshold of H_2S to 1060 Å have been determined previously by Watanabe and Jursa [16]. By normalizing the PIE curve for H_2S^+ obtained here to the absolute values

---

[1]Masuko et al. [15] also reported a Rydberg series which was assigned to the $2b_1 \rightarrow ndb_2$ transitions and has a quantum defect $\delta \approx 0.4$. Thus, the assignments of Progressions I and II to the $2b_2 \rightarrow 4bd_2$ and $2b_2 \rightarrow 5db_2$ transitions, respectively, cannot be excluded.

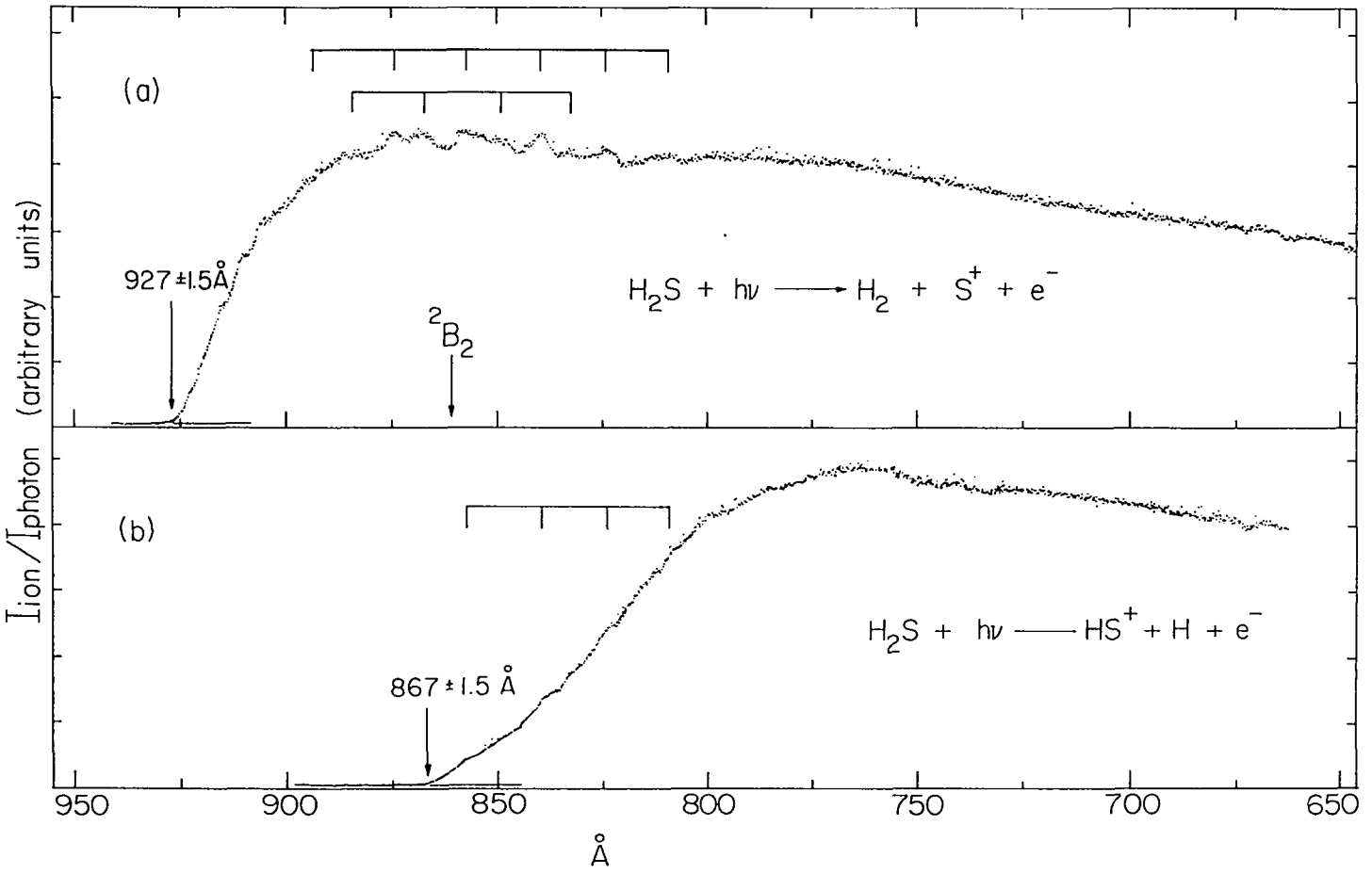

Figure 6. (a) PIE curve (1.4 Å FWHM) for S^+ from H_2S in the region 650-950 Å; (b) PIE curve (1.4 Å FWHM) for HS^+ from H_2S in the region 660-900 Å

for $\sigma_i(H_2S^+)$ near the threshold region, $\sigma_i(H_2S^+)$ in the region 645-1186 Å can be estimated. Table 4 lists some of the estimated values for $\sigma_i(H_2S^+)$ at intervals of 50 Å. The values for $\sigma_i(S^+)$ and $\sigma_i(HS^+)$ have also been deduced from the measured relative intensities of H_2S^+, S^+, and HS^+. The latter values have been corrected for the sulfur isotopic effect. The differences in transmission of these ions through the mass spectrometer used in this experiment has not been corrected. However, since the masses of H_2S^+, HS^+, and S^+ differ only by one to two mass units, the transmission factors are expected to have minor effects on the measured relative intensities of H_2S^+, HS^+, and S^+. Excluding the uncertainty of the measurement of Watanabe and Jursa [16], the values for $\sigma_i(H_2S^+)$, $\sigma_i(S^+)$, and $\sigma_i(HS^+)$ are expected to be better than ±15%.

Some discrepancies were found between the PIE curve for H_2S^+ obtained in this study and that reported by Dibeler and Liston [22]. In the present work, the height of the broad peak at ~925 Å is about four times the height of the onset region, whereas in Ref. 22, the ratio is approximately seven. The VUV photon detector used here is a sodium salicylate fluorescence detector which is known to have a nearly constant quantum yield in the range ~300-2000 Å [36,37]. In the previous experiment, a tungsten photoelectric detector was used. Since the efficiency of a tungsten photoelectric detector varies substantially in the region 650-1190 Å [38], it is most likely that the difference observed in the relative PIE for H_2S^+ by the two studies arises from improper corrections in detection efficiencies at different wavelengths for the tungsten photoelectric detector of the previous study.

Table 4. Absolute photoionization cross sections for H_2S^+, S^+, and HS^+

λ(Å)	σ_i (10^{-17} cm^2)		
	H_2S^+	S^+	HS^+
1150	1.8	...	...
1100	2.5	...	...
1050	3.8	...	...
1000	4.1	...	...
950	5.7	...	...
900	6.5	1.4	...
850	5.1	2.0	0.4
800	4.3	1.8	2.3
750	4.3	1.8	3.0
700	4.1	1.6	2.6
650	3.7	1.4	2.5

In summary, high resolution PIE curves for H_2S^+ have been obtained in the region 645-1190 Å. By using the results of previous photoelectron and photoabsorption studies, autoionizing vibrational progressions resolved in the spectrum have been tentatively assigned. A more definite assignment of Rydberg structures in this region will require a higher resolution study in the future.

References

1. K. Siegbahn, C. Nording, G. Johansson, J. Hedman, P. F. Heden, K. Hamrin, U. Gelius, T. Bergmark, L. O. Werme, R. Manne and Y. Baer, ESCA Applied to Free Molecules (North-Holland Publ. Co., Amsterdam, 1969).

2. J. Delwiche, P. Natalis and J. E. Collin, Int. J. Mass Spectrom. Ion Phys. 5, 443 (1970).

3. D. W. Turner, G. Baker, A. D. Baker and C. R. Brundle, Molecular Photoelectron Spectroscopy (Wiley-Interscience, London, 1970).

4. A. W. Potts and W. C. Price, Proc. R. Soc. London, Ser. A 326, 181 (1972).

5. D. C. Frost, A. Katrib, C. A. McDowell and R. A. N. McLean, Int. J. Mass Spectrom. Ion Phys. 7, 485 (1971).

6. R. N. Dixon, G. Duxbury, M. Horani and J. Rostas, Mol. Phys. 22, 977 (1971).

7. S. Durmaz, G. H. King and R. J. Suffolk, Chem. Phys. Lett. 13, 304 (1972).

8. M. I. Al-Joboury and D. W. Turner, J. Chem. Soc. 49, 482 (1968).

9. C. R. Brundle and A. D. Baker, Electron Spectroscopy, Vol. 3 (Academic Press, London. 1979).

10. L. Karlsson, L. Mattsson, R. Jadrny, T. Bergmark and K. Siegbahn, Phys. Scr. 13, 229 (1976).

11. W. C. Price, J. Chem. Phys. 4, 147 (1936).

12. L. Bloch, E. Bloch and P. Herreng, C. R. Acad. Sci. 203, 782 (1936).

13. W. C. Price, J. P. Teegan and A. D. Walsh, Proc. R. Soc. London, Ser. A 201, 600 (1950).

14. L. B. Clark and W. T. Simpson, J. Chem. Phys. 43, 3666 (1965).

15. H. Masuko, Y. Morioka, M. Nakamura, E. Ishiguro and M. Sasanuma, Can. J. Phys. 57, 745 (1979).

16. K. Watanabe and A. S. Jursa, J. Chem. Phys. 41, 1650 (1964).

17. M. Horani, S. Leach and J. Rostas, J. Mol. Spectrosc. 23, 115 (1967).

18. W. C. Price and T. M. Sugden, Trans. Faraday Soc. 44, 108 (1948).

19. D. C. Frost and C. A. McDowell, Can. J. Chem. 36, 39 (1958).

20. V. H. Dibeler and H. M. Rosenstock, J. Chem. Phys. 39, 3106 (1963).

21. K. Watanabe, T. Nakayama and J. Mottl, J. Quant. Spectrosc. Radiat. Transfer 2, 369 (1962).

22. V. H. Dibeler and S. K. Liston, J. Chem. Phys. 49, 482 (1968).

23. E. A. Walters and N. C. Blais, J. Chem. Phys. 75, 4208 (1981).

24. G. Duxbury, M. Horani and J. Rostas, Proc. R. Soc. London, Ser. A 331, 109 (1972).

25. P. J. Bruna, G. Hirsch, M. Peric, S. D. Peyerimhoff and R. J. Buenker, Mol. Phys. 40, 521 (1980).

26. G. Hirsch and P. J. Bruna, Int. J. Mass Spectrom. Ion Phys. 36, 37 (1980).

27. J. H. D. Eland, Int. J. Mass Spectrom. Ion Phys. 31, 161 (1979).

28. Y. Ono, S. H. Linn, H. F. Prest, M. E. Gress and C. Y. Ng, J. Chem. Phys. 73, 2523 (1980).

29. K. E. Schubert and R. D. Hudson, A Photoelectric Atlas of the Intense Lines of the Hydrogen Molecular Emission Spectrum from 1025 to 1650 Å at a Resolution of 0.10 Å, Report Number ATN-64(9233)-2 (Aerospace Corp., Los Angeles, 1963).

30. Y. Ono, E. A. Osuch and C. Y. Ng, J. Chem. Phys. 76, 3905 (1982).

31. Y. Ono, E. A. Osuch and C. Y. Ng, J. Chem. Phys. 74, 1645 (1981).

32. J. Erickson and C. Y. Ng, J. Chem. Phys. 75, 1650 (1981).

33. E. Lindholm, Ark. Fys. 40, 97 (1968).

34. H.-T. Wang, W. S. Felps and S. P. McGlynn, J. Chem. Phys. 67, 2614 (1977).

35. H. C. Allen and E. K. Plyler, J. Chem. Phys. 25, 1132 (1956).

36. J. A. R. Samson, J. Opt. Soc. Am. 54, 6 (1964).

37. J. A. R. Samson, Techniques of Vacuum Ultraviolet Spectroscopy (Wiley, New York, 1967), p. 215.

38. R. B. Cairns and J. A. R. Samson, J. Opt. Soc. Am. 56, 1568 (1966).

SECTION II. PHOTOIONIZATION STUDY OF $(H_2S)_2$ AND $(H_2S)_3$

Introduction

The ion-molecule reactions between H_2S^+ and H_2S are relatively unexplored. Previous studies by high pressure mass spectrometry [1-2], selected ion flow tube [3], and ion cyclotron resonance [4-6] are in general agreement that the H_3S^+ ion is the most important product ion. The cylotron ejection experiment of Huntress and Pinizzotto [6] showed that the formation of H_3S^+ proceeds almost equally via both proton transfer and hydrogen-atom abstraction. Their experiment further revealed that in addition to the H_3S^+ + HS channel, charge transfer is also a major primary reaction channel for $H_2S^+ + H_2S$.

The S_2^+, HS_2^+, $H_2S_2^+$, and $H_3S_2^+$ ions, which were much lower in intensity in comparison with H_3S^+, have been observed by Ruska and Franklin [1] in a low pressure ion source of H_2S. At higher source pressures of H_2S, ions such as $H_5S_2^+$ and $H_2S_3^+$ resulting from condensation processes or termolecular mechanisms were also found. The results of a trapped ion study by Harrison [5] provided evidence that the S_2^+, HS_2^+, $H_2S_2^+$, and $H_3S_2^+$ ions were secondary in nature and were formed mainly by the reactions between S^+ and HS^+ with H_2S. The S^+ and HS^+ ions were among the major constituents in the ion source and were produced by electron impact ionization of H_2S. Nevertheless, the later experiment of Huntress and Pinizzotto has been able to identify HS_2^+ to be a primary product ion for the reaction of $H_2S^+ + H_2S$. These observations motivate (further) investigation of the association of S_2^+, HS_2^+, $H_2S_2^+$, and $H_3S_2^+$ with the reactions between H_2S^+ and H_2S.

This report presents the results and an analysis of a study of the unimolecular decompositions of $(H_2S)_2^+$ and $(H_2S_3)_3^+$ which were prepared by photoionization of $(H_2S)_2$ and $(H_2S)_3$ formed in a supersonic beam of H_2S.

$$(H_2S)_2 + h\nu \rightarrow H_2S^+ \cdot H_2S + e^- \rightarrow S_2^+ + 2H_2 + e^- \quad (1)$$

$$\rightarrow HS_2^+ + H_2 + H + e^- \quad (2)$$

$$\rightarrow H_2S_2^+ + H_2 + e^- \quad (3)$$

$$\rightarrow H_3S^+ + HS + e^- \quad (4)$$

$$\rightarrow H_3S_2^+ + H + e^- \quad (5)$$

$$(H_2S)_3 + h\nu \rightarrow H_2S^+ \cdot (H_2S)_2 + e^- \rightarrow H_5S_2^+ + HS + e^- \quad (6)$$

By measuring the photoionization efficiency (PIE) spectra of S_2^+, HS_2^+, $H_2S_2^+$, H_3S^+, $H_3S_2^+$, and $(H_2S)_2^+$ from $(H_2S)_2$ and $H_5S_2^+$ and $(H_2S)_3^+$ from $(H_2S)_3$, we have been able to examine the internal energy effects and the energetics of reactions (1)-(6). The study of these unimolecular reactions is expected to have direct bearing on the formation of S_2^+, HS_2^+, $H_2S_2^+$, H_3S^+, and $H_3S_2^+$ from the reactions of $H_2S^+ + H_2S$ by the collisional complex mechanism. Similar photoionization studies on other systems [7-11] have been reported. The merits of the photoionization of van der Waals clusters have also been discussed previously.

Experimental

The experimental arrangement and procedures were essentially the same as those described previously [12,13]. Briefly, the apparatus consists of a 3-meter near-normal incidence vacuum ultraviolet (VUV) monochromator (McPherson 2253M), a supersonic molecular beam production system, a capillary discharge lamp, a VUV light detector, and a quadrupole mass spectrometer for ion detection. The grating employed in this study was a Bausch and Lomb 1200 lines/mm MgF_2 coated aluminum grating blazed at 1360 Å. Either the hydrogen many-lined pseudocontinuum or the helium Hopfield continuum was used as the light source, depending on the wavelength region desired.

The hydrogen sulfide was obtained from Matheson with a quoted purity of ≥99.6%. The H_2S molecular beam was produced by supersonic expansion through a 120 μm diameter (D) stainless steel nozzle. The nozzle stagnation pressure (P_o) was varied in the range of ∿150-500 Torr. With the exception of the PIE spectrum of H_2S^+ [14], which was obtained at a nozzle temperature (T_o) of 290 K, all the other PIE spectra were measured at $T_o \approx 230$ K. In a typical run, the fluctuation in the nozzle temperature was less than ±3 K as monitored with thermocouples. Since the hydrogen sulfide beam was sampled in a collisionless environment, the observed fragment ions represent the primary fragments of H_2S^+, $(H_2S)_2^+$, $(H_2S)_3^+$, and higher hydrogen sulfide cluster ions.

All the data were obtained with an optical resolution of 1.4 Å (FWHM). Data points were taken typically at either 0.5 or 1.0 Å

intervals. The standard deviations of PIE data presented here are better than 10%. Each PIE spectrum was based on at least two scans, and prominent structures in the curves were found to be reproducible. Wavelength calibrations were achieved by using known atomic resonance lines or H_2 emission lines [15] when the H_2 pseudocontinuum was used.

Stemming from the fact that the ions of interest in this experiment, S_2^+, HS_2^+, $H_2S_2^+$, H_3S^+, $H_3S_2^+$, and $H_5S_2^+$, were, in general, much lower in intensity in comparison with the intensities of S^+, HS^+, H_2S^+, $(H_2S)_2^+$, and $(H_2S)_3^+$, it was necessary to operate the mass spectrometer at a resolution sufficiently high to minimize the contribution of intense ions to weaker fragments. The major isotopes of sulfur are ^{32}S, ^{33}S, and ^{34}S which have the natural abundances of 95, 0.76, and 4.22 percent [16], respectively. Maintaining a high mass resolution also makes possible a meaningful correction for the sulfur and hydrogen isotopic effects. The mass spectra of H_2S in the mass range m/e = 31 to 36 obtained at 950 and 800 Å are shown in Figs. 1(a) and (b), respectively, to illustrate the typical mass resolution used in this study.

Results and Discussion

Figure 2(b) shows the PIE curve for $(H_2S)_2^+$ in the region 640-1310 Å obtained at $P_o \approx 465$ Torr. The PIE spectrum for H_2S^+, measured with the same optical resolution, is shown in Fig. 2(a) for comparison. The analyses of the PIE spectra for H_2S^+ and its fragment ions S^+ and HS^+ have been reported previously [14]. The general profile of the PIE curve for $(H_2S)_2^+$ is similar to that for H_2S^+ in the region ~927-1185 Å.

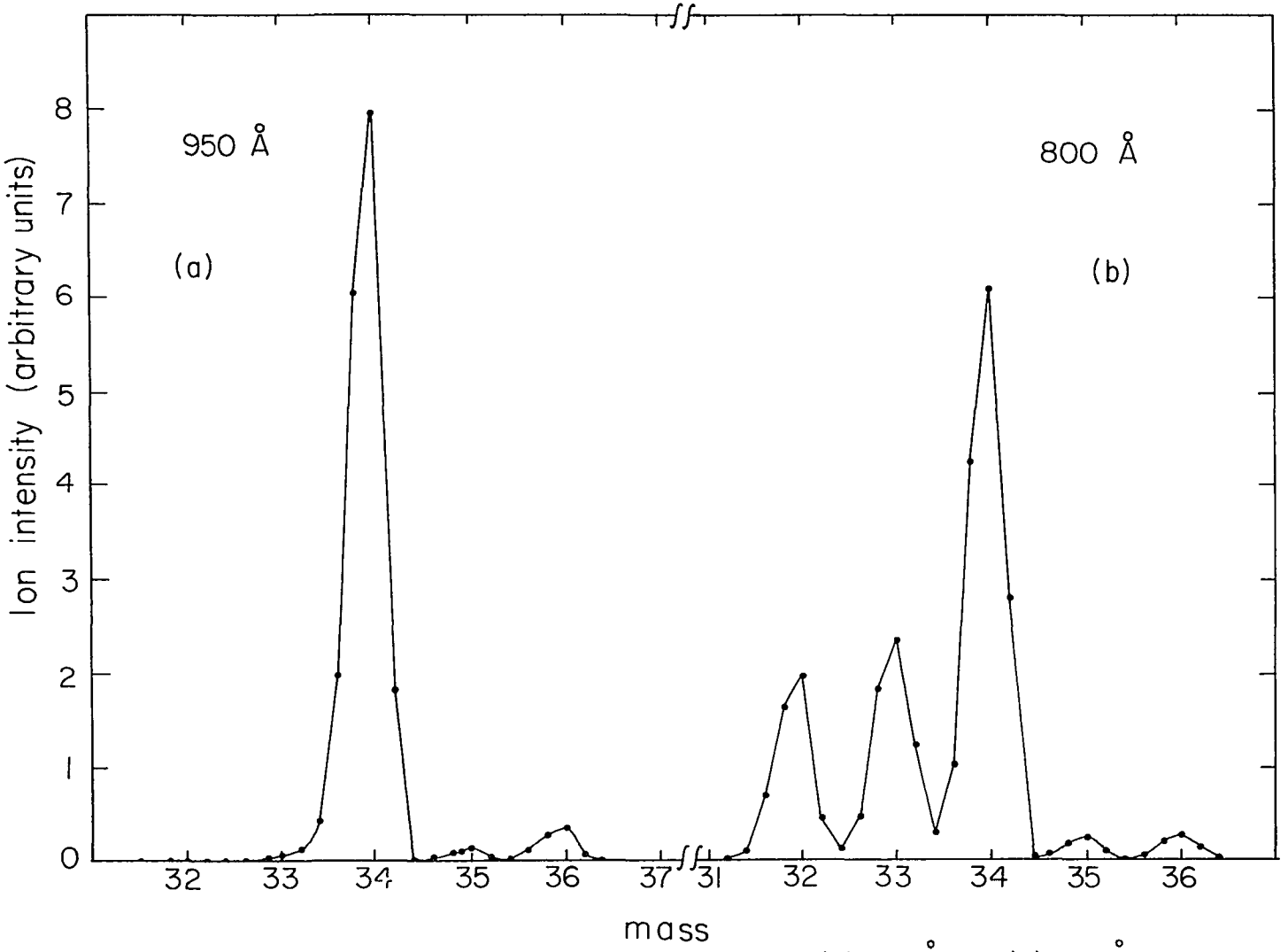

Figure 1. The mass spectra of H_2S obtained at (a) 950 Å and (b) 800 Å

Figure 2. (a) PIE curve for H_2S^+ in the region 650-1185 Å (nozzle conditions: $P_o \approx 150$ Torr, $T_o \approx 298$ K, D = 120 μm); (b) PIE curve for $(H_2S)_2^+$ in the region 640-1310 Å (nozzle conditions: $P_o \approx 465$ Torr, $T_o \approx 230$ K, D = 120 μm); (c) PIE curve for the mass 35 ions ($H_3{}^{32}S^+ + H_2{}^{33}S^+ + H^{34}S^+$) in the region 600-1185 Å (nozzle conditions: $P_o \approx$ 465 Torr, $T_o \approx 230$ K, D = 120 μm); (d) PIE curve for $(H_2S)_3^+$ in the region 650-1325 Å (nozzle conditions: $P_o \approx 465$ Torr, $T_o \approx 230$ K, D = 120 μm); and (e) PIE curve for the mass 69 ions ($H_3{}^{32}S^+ \cdot H_2{}^{32}S + H_2{}^{32}S^+ \cdot H_2{}^{33}S + H_2{}^{32}S \cdot H_2{}^{32}S + H^{34}S^+ \cdot H_2{}^{32}S^+ + H^{32}S^+ \cdot H_2{}^{34}S$) in the region 700-1300 Å (nozzle conditions: $P_o \approx 500$ Torr, $T_o \approx$ 230 K, D = 120 μm). All PIE spectra were obtained with a wavelength resolution of 1.4 Å (FWHM)

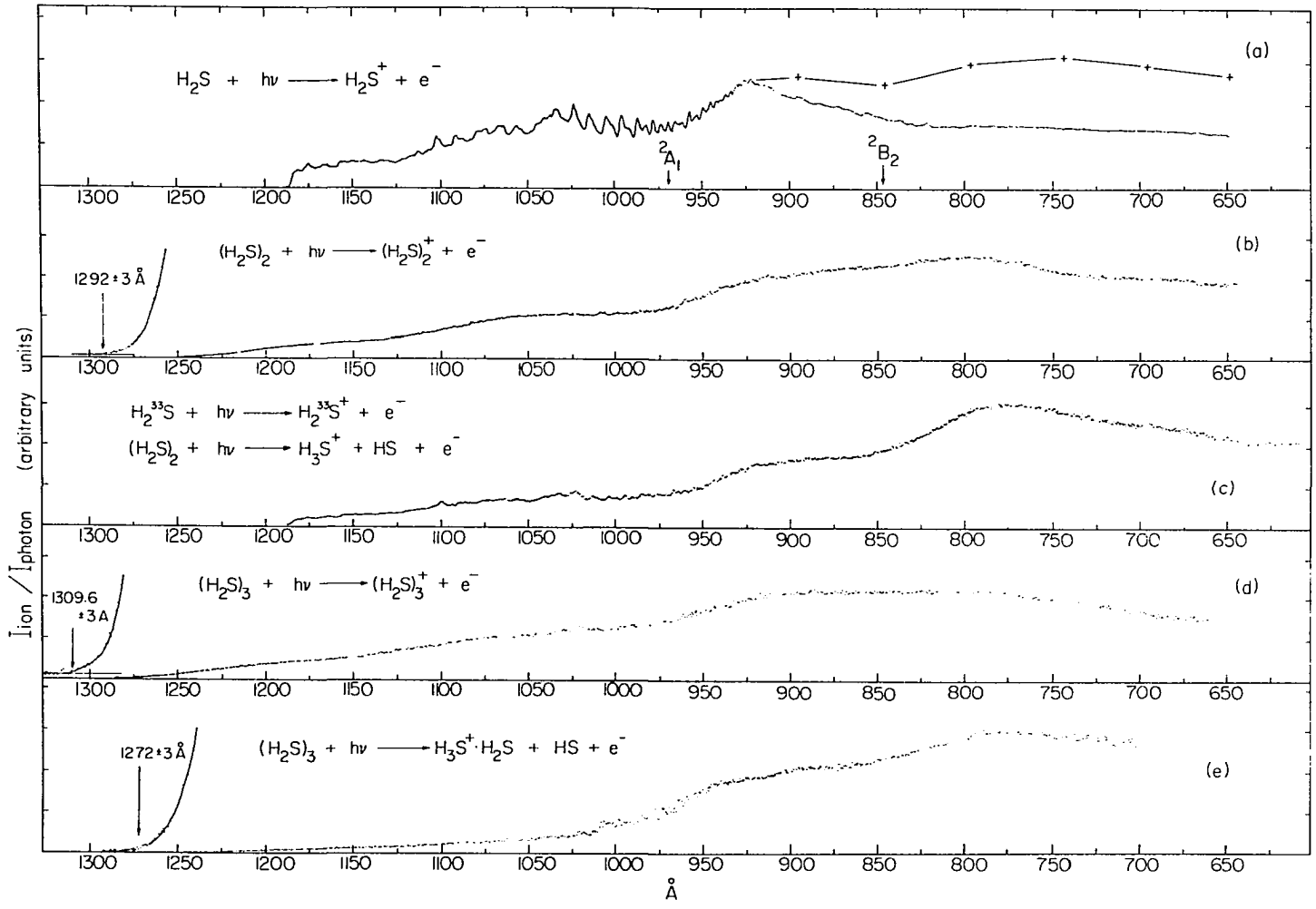
(a)
$H_2S + h\nu \longrightarrow H_2S^+ + e^-$
$^2A_1$
$^2B_2$
(b)
$(H_2S)_2 + h\nu \longrightarrow (H_2S)_2^+ + e^-$
1292 ± 3 Å
(c)
$H_2{}^{33}S + h\nu \longrightarrow H_2{}^{33}S^+ + e^-$
$(H_2S)_2 + h\nu \longrightarrow H_3S^+ + HS + e^-$
(d)
$(H_2S)_3 + h\nu \longrightarrow (H_2S)_3^+ + e^-$
1309.6 ±3A
(e)
$(H_2S)_3 + h\nu \longrightarrow H_3S^+ \cdot H_2S + HS + e^-$
1272 ± 3 Å
1300 1250 1200 1150 1100 1050 1000 950 900 850 800 750 700 650
I_{ion} / I_{photon} (arbitrary units)
Å

In accordance with observations in other systems [9,17-20], autoionizing structures resolved in the H_2S^+ spectrum are hardly discernible in the $(H_2S)_2^+$ spectrum. Since autoionizing Rydberg states in this region have mostly been assigned as vibrationally excited states [14], the lack of structures in the PIE curve for $(H_2S)_2^+$ is likely due to efficient vibrational predissociation of excited Rydberg states of the hydrogen sulfide dimers.

At ~927 Å, the PIE for H_2S^+ starts to decrease toward higher photon energies, whereas the PIE for $(H_2S)_2^+$ continues to increase gradually till ~780 Å. The decrease in PIE for H_2S^+ is a consequence of strong predissociations of H_2S^+ to form S^+ and HS^+ in this region

$$H_2S^+ \rightarrow S^+ + H_2 \qquad (7)$$

$$\rightarrow HS^+ + H \qquad (8)$$

[14]. After including the PIEs for S^+ and HS^+, the corrected PIE curve for H_2S^+ in the region ~780-927 Å (the upper curve in Fig. 2(a)) is found to roughly resemble the shape of the PIE curve for $(H_2S)_2^+$. This observation can be taken as evidence that the probabilities for dissociation processes of $(H_2S)_2^+$ such as

$$H_2S^+ \cdot H_2S \rightarrow S^+ \cdot H_2S + H_2 \qquad (9)$$

$$\rightarrow HS^+ \cdot H_2S + H \qquad (10)$$

are much lower than those of the corresponding reactions (7) and (8). In view of the fact that the $H_2S^+ \cdot H_2S$ complex has more degrees of

freedom in which to redistribute the excess energy of the H_2S^+ moiety in the dimer ion, according to statistical theory, it is reasonable to expect that reactions (9) and (10) are less favorable in comparison with reactions (7) and (8) for the same amount of excess energy. The decreasing trend found in the PIE curve for $(H_2S)_2^+$ in the region ~650-800 Å correlates well with the corresponding increases in the formation of S_2^+, HS_2^+, $H_2S_s^+$, H_3S^+, and $H_3S_2^+$ via reactions (1)-(5) which will be discussed later.

The ionization energy (IE) for $(H_2S)_2^+$ determined in this study was 9.596 ± 0.022 eV (1292 ± 3 Å), which is 0.14 eV lower in energy than that reported recently by Walters and Blais [21]. The existence of weak hydrogen bonding between H_2S molecules was concluded by Harada and Kitamura [22] from considerations based on the structure of solid hydrogen sulfide. From second virial coefficient data [23,24], the well depth for H_2S-H_2S interaction can be estimated to be 0.028 eV. In a spectroscopic study, Lowder et al. [25] obtained a dimerization energy of 0.074 ± 0.013 eV for $(H_2S)_2$. Depending on the geometry of the H_2S dimer, theoretical calculations yielded values in the range 0.01-0.08 eV [26-29]. Here, the average experimental value 0.05 ± 0.03 eV is used as the bond dissociation energy (D_o) for $H_2S \cdot H_2S$. When the IEs of H_2S (10.4607 ± 0.0026 eV) [14,30,31] and $(H_2S)_2$ and the value for $D_o(H(H_2S)_2)$ are used, $D_o((H_2S)_2^+)$ can be calculated from the relation

$$D_o((H_2S)_2^+) = IE(H_2S) + D_o((H_2S)_2) - IE((H_2S)_2) \quad . \qquad (11)$$

The calculated value for $D_o((H_2S_2)_2^+)$ is 0.92 ± 0.04 eV (21.2 ± 0.9 kcal/

mol). This value is comparable to the bond dissociation energies of many other simple inorganic and organic dimer ions [9,10,12,18,19,33,34], but substantially lower than the value of 1.58 ± 0.13 eV for $D_0((H_2O)_2^+)$ [32,35].

The PIE data for $(H_2S)_3^+$ in the region ∿650-1325 Å obtained at $P_o \approx 460$ Torr are plotted in Fig. 2(d). The PIE curves for $(H_2S)_3^+$ and $(H_2S)_2^+$ are similar in appearance. The IE of $(H_2S)_3$ was determined to be 9.467 ± 0.022 eV (1309.6 ± 3 Å) which is also found to be lower than a value of 9.63 ± 0.01 eV obtained by Walters and Blais [21]. Assuming that the bond dissociation energy for $(H_2S)_2 \cdot H_2S$ is the same as that for $H_2S \cdot H_2S$ and when the IEs of $(H_2S)_2$ and $(H_2S)_3$ are used, a value of 0.18 ± 0.04 eV for $D_0((H_2S_2^+ \cdot H_2S)$ is deduced from a relation similar to Eq. (11).

The PIE spectrum for the mass 35 ions in the region ∿600-1200 Å is shown in Fig. 2(c). The $H_3{}^{32}S^+$, $H_2{}^{33}S^+$, $H^{34}S^+$, $DH^{32}S^+$, and $D^{33}S^+$ ions cannot be resolved by our quadrupole mass spectrometer. Considering the low natural abundance of the deuterium isotope (0.015%) [16], the intensities of the latter two ions should be much lower than those of $H_3{}^{32}S^+$, $H_2{}^{33}S^+$, and $H^{34}S^+$. In the region ∿925-1200 Å, the spectrum of the mass 35 ions exhibits the same structure observed in the PIE curve for H_2S^+, an observation indicating that the mass 35 ions in this region are predominantly the $H_2{}^{33}S^+$ ions formed by the direct photoionization of H_2S. The profiles of the PIE curves for the mass 35 ions and $(H_2S)_2^+$ are similar in the region ∿850-925 Å. At wavelengths shorter than ∿867 Å, which is the AE for the formation of HS^+ from H_2S [14], we

find that the $H^{34}S^+$ ions are mainly responsible for the further increase in PIE of the mass 35 ions. In principle, the true PIE curve for $H_3{}^{32}S^+$ can be obtained by substracting the intensities of $H_2{}^{33}S^+$ and $H^{34}S^+$ from that of the mass 35 ions. The true and the uncorrected PIE curves for H_3S^+ in the region ~650-1000 Å are compared in Fig. 3. The profile for the true PIE curve for H_3S^+ is again found to bear some resemblance to that for $(H_2S)_2^+$. The true PIE for H_3S^+ decreases dramatically from ~925 Å toward longer wavelengths. In the region ~950-1180 Å, the intensity of H_3S^+ is less than 10% that of the $H_2{}^{33}S^+$ ion.

According to thermodynamic data listed in Table 1 [36-40], the AE for reaction (4) is predicted to be in the range ~10-07-10.29 eV (1231-1205 Å) which is slightly lower than the IE of H_2S. Since one anticipates that the PIE spectra for $H_2{}^{32}S^+$ and $H_2{}^{33}S^+$ are identical and that the $H_2{}^{33}S^+$ ions cannot be formed below the IE of H_2S, a careful examination of the PIE curves for the mass 35 ($H_2{}^{33}S^+ + H_3{}^{32}S^+$) and the mass 34 ($H_2{}^{32}S^+$) ions below the ionization threshold for H_2S should make possible the identification of the PIE curve for H_3S^+. Figures 4(a) and (b) show the PIE curves in the region ~1180-1240 Å for the mass 35 and 34 ions, respectively. The PIEs for the mass 34 and 35 ions were normalized at 1180 Å. As expected, this comparison clearly brings out the difference between the PIE spectra for the mass 34 and 35 ions in the energy range lower than the IE of H_2S. The finite yields observed for the mass 35 ions in the region ~1190-1210 Å are definitely due to reaction (4). The AE for the formation of H_3S^+ is quite distinct and has a value of 10.249 ± 0.012 eV (1209.7 ± 1.5 Å). From the latter

Figure 3. The relative PIEs for $(H_2S)_3^+$, $H_5S_2^+$, $(H_2S)_2^+$, $H_3S_2^+$, $H_2S_2^+$, HS_2^+, S_2^+, and H_3S^+ in the region ~65-1000 Å obtained with $P_o \approx 360$ Torr and $T_o \approx 230$ K. The PIE spectra connected by solid lines have not been corrected for isotopic effects. The PIE spectrum for H_3S^+ connected by dash lines has been corrected for isotopic contributions. No corrections were made to account for transmission factors of these ions through the mass spectrometer used in this experiment

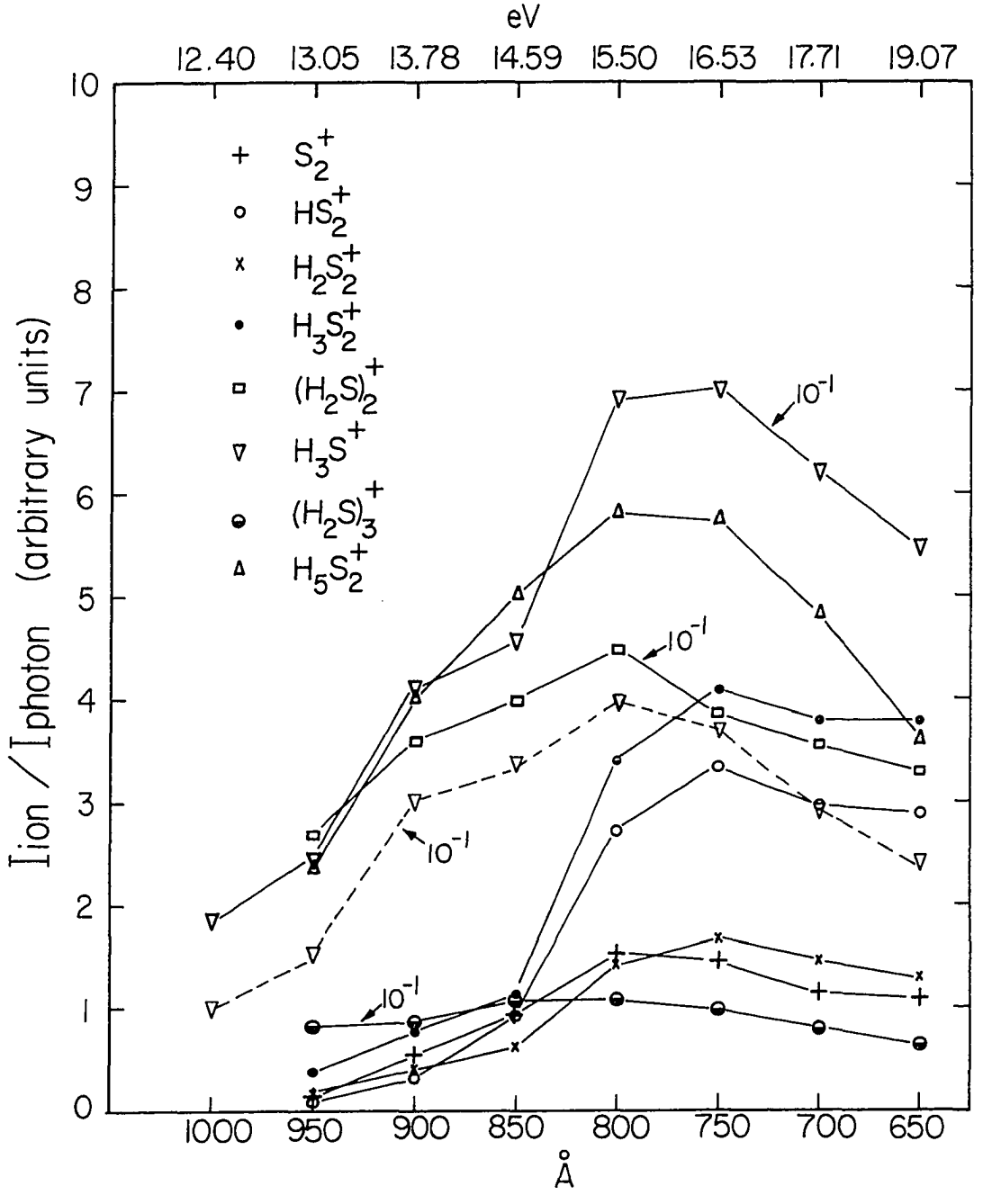
eV
12.40
13.05
13.78
14.59
15.50
16.53
17.71
19.07
S_2^+
HS_2^+
$H_2S_2^+$
$H_3S_2^+$
$(H_2S)_2^+$
H_3S^+
$(H_2S)_3^+$
$H_5S_2^+$
10^{-1}
10^{-1}
10^{-1}
10^{-1}
Iion / Iphoton (arbitrary units)
0
1
2
3
4
5
6
7
8
9
10
1000
950
900
850
800
750
700
650
Å

Table 1. Heats of formation at 0 K in kcal/mol of neutrals and ions[a]

Compound	Neutrals	Ions
$(H_2S)_3$	-14.9 ± 1.0 [36]	203.5 ± 1.1[b]
$H_5S_2^+$		178.9 ± 1.8[b]
$(H_2S)_2$	-9.4 ± 0.7 [36]	211.9 ± 0.9[b]
$H_3S_2^+$		< 238[b]
$H_2S_2^+$		239-246[c] [37]
		< 290[b]
HS_2^+		232-249[c] [6]
		< 248[b]
S_2^+		∿ 246[b]
H_3S^+		193.8 ± 1.4[b]
		188.3-193.3[c] [36,39,40]
H_2S	-4.2 ± 0.2 [40]	237.02 ± 0.21 [14,38]
	-4.9 ± 0.2 [40]	
HS	33.14 ± 1.2 [40]	∿274 [38]
	33.3 ± 1.2[c] [40]	
S	65.66 ± 0.06 [40]	305 [38]
	66.20 ± 0.06[c] [40]	
H	51.631 ± 0.001 [36]	365.236 ± 0.01 [36]
	52.100 ± 0.001[c] [36]	367.186 ± 0.01 [36]

[a]The numbers in []s are the references.

[b]This work. Because of the high degree of rotational and low frequency vibrational relaxation in the supersonic expansion, these values can be considered to be the heats of formation at 0 K.

[c]Heats of formation at 298 K.

Figure 4. PIE curves for (a) the mass 35 ions ($H_2{}^{33}S^+ + H_3{}^{32}S^+$ and (b) the mass 34 ions ($H_2{}^{32}S^+$) in the region ~1178-1240 Å obtained with a wavelength resolution of 1.4 Å (FWHM). The PIEs for the mass 34 and 35 ions have been normalized at 1180 Å. (Nozzle conditions: $P_o \approx$ Torr, $T_o \approx 230$ K)

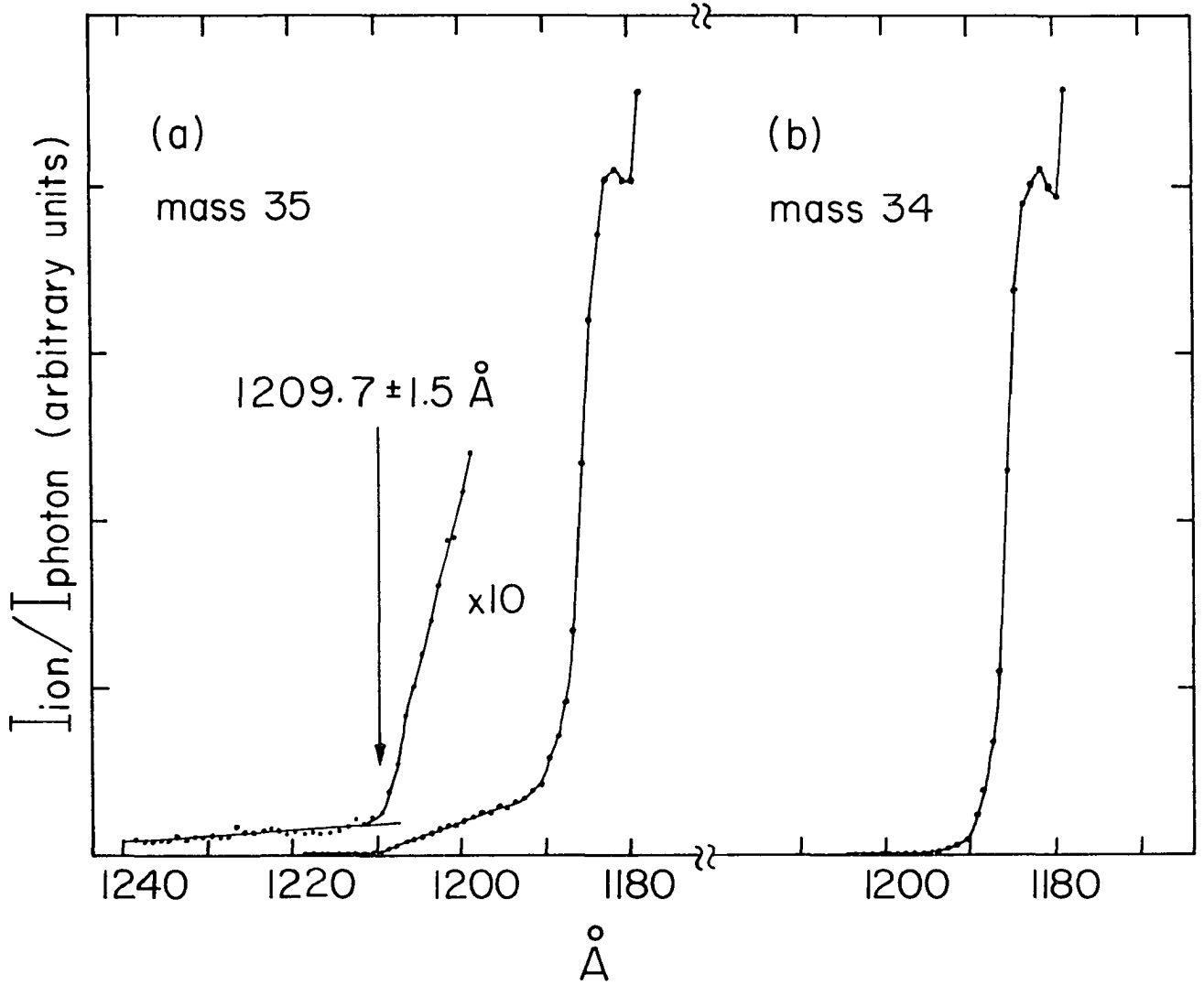
(a)
mass 35
(b)
mass 34
1209.7 ± 1.5 Å
x10
I ion / I photon (arbitrary units)
1240
1220
1200
1180
1200
1180
Å

value, together with the known heats of formation for $(H_2S)_2$ [36] and HS [40] at 0 K (Table 1), the heat of formation for H_3S^+ at 0 K is calculated to be 193.8 ± 1.4 kcal/mole. The proton affinity is equal to the enthalpy change for the reaction

$$H_2S + H^+ \rightarrow H_3S^+ \quad . \tag{12}$$

When the value for $\Delta H^o_{f0}(H_3S^+)$ and the values for $\Delta H^o_{f0}(H_2S)$[40] and $\Delta H^o_{f0}(H^+)$ [36] (Table 1) are used, the absolute proton affinity for H_2S at 0 K is deduced to be 167.2 ± 1.4 kcal/mole. We note that the uncertainty of the proton affinity determined here is largely due to the uncertainties in $\Delta H^o_{f0}(HS)$ and to a smaller extent due to the bond dissociation energy of $H_2S \cdot H_2S$. Conventionally, the proton affinity is referred to 298 K. Assuming an ideal gas model and excluding any vibrational and electronic contributions to the heat capacities of H_2S and H_3S^+, a value of 168.7 ± 1.4 kcal/mole can be obtained for the absolute proton affinity of H_2S at 298 K. The latter value is found to be in agreement with the literature values [41-47].

The PIE curve for the mass 69 ions in the region ∿700-1300 Å is shown in Fig. 2(e). The mass 69 ions observed here mainly consist of the $H_5{}^{32}S_2^+$, $H_2{}^{32}S^+ \cdot H_2{}^{33}S$, $H_2{}^{33}S^+ \cdot H_2{}^{32}S$, $H^{34}S^+ \cdot H_2{}^{32}S$, and $H^{32}S^+ \cdot H_2{}^{34}S$ ions. Similarity in appearance can be found between the PIE curves for the mass 35 and the mass 69 ions in the region ∿700-925 Å. The contributions attributable to the $H^{34}S^+ \cdot H_2{}^{32}S^+$ and $H^{32}S^+ \cdot H_2{}^{34}S$ ions to the intensity of the mass 69 ions observed here in the region ∿700-870 Å are much lower than the corresponding contribution of the $H^{34}S^+$ ion to

the observed intensity of the mass 35 ions. This is consistent with the conclusion that the intensity of the $HS^+ \cdot H_2S$ ions formed by fragmentations of hydrogen sulfide dimers and clusters is much lower than that of HS^+ from H_2S. At photon wavelengths longer than ~890 Å, the contributions of the $H^{34}S^+ \cdot H_2{}^{32}S$ and $H^{32}S^+ \cdot H_2{}^{34}S$ ions become negligible in comparison with those of $H_5{}^{32}S_2^+$, $H_2{}^{32}S^+ \cdot H_2{}^{33}S$, and $H_2{}^{33}S^+ \cdot H_2{}^{32}S$. The ratio of the intensity of $H_5{}^{32}S_2^+$ to that of $H_2{}^{32}S^+ \cdot H_2{}^{33}S + H_2{}^{33}S^+ \cdot H_2{}^{32}S$ is approximately 0.9 at 1190 Å. At 1250 Å, this ratio decreases to ~0.2. After a careful correction for the contributions from the $H_2{}^{32}S^+ \cdot H_2{}^{33}S$ and $H_2{}^{33}S^+ \cdot H_2{}^{32}S$ ions, the AE for the formation of $H_3S^+ \cdot H_2S$ by reaction (6) is determined to be 1260 ± 5 Å (9.84 ± 0.04 eV). By using the latter value and the known heats of formation for $(H_2S)_3$ and HS at 0 K (Table 1), $\Delta H^o_{f0}(H_5S_2^+)$ is calculated to be 178.9 ± 1.9 kcal/mole. The latter value and $\Delta H^o_{f0}(H_3S^+)$ determined here allow a value of 10.7 ± 2.2 kcal/mole to be calculated for the enthalpy change of the association reaction at 0 K.

$$H_3S^+ + H_2S \rightarrow H_3S^+ \cdot H_2S \qquad (13)$$

In a study by pulsed, high-pressure mass spectrometry, Meot-Ner and Field [48] obtained a value of 12.8 ± 1.5 kcal/mole for the enthalpy change of reaction (13) at approximately 370 K. Assuming an ideal-gas model and excluding any vibrational and electronic contributions to the heat capacities of H_3S^+, H_2S, and $H_3S^+ \cdot H_2S$, it can be shown that the latter value corresponds to a value of 10.6 ± 1.5 kcal/mole for ΔH^o_0 which is in excellent agreement with the value derived from this study.

The relative PIEs for $(H_2S)_3^+$, $H_5S_2^+$, $(H_2S)_2^+$, $H_3S_2^+$, $H_2S_2^+$, HS_2^+, S_2^+, and H_3S^+ in the region 650-1000 Å obtained with $P_o \approx 360$ Torr and $T_o \approx 230$ K are plotted in Fig. 3 at intervals of 50 Å. Although the PIEs of these ions have not been corrected for isotopic contributions, these measurements show that S_2^+, HS_2^+, $H_2S_2^+$, and $H_3S_2^+$ are minor fragment ions from the hydrogen sulfide dimer and cluster ions. In the nozzle expansion conditions used here, the hydrogen sulfide dimers and trimers are the dominate cluster species in the beam. At $T_o \approx 230$ K, the relative intensities of these ions measured at a given wavelength were found to be strongly dependent upon P_o which in effect determines the distribution in concentration of the hydrogen sulfide clusters in the beam. This observation is consistent with the interpretation that not only can the S_2^+, $H_2S_2^+$, HS_2^+, $H_3S_2^+$, and H_3S^+ ions be formed by reactions (1)-(5), but that they also can be produced by fragmentations of higher cluster ions such as $(H_2S)_3^+$.

$$(H_2S)_3 + h\nu \rightarrow (H_2S)_3^+ + e^- \rightarrow S_2^+ + H_2S + 2H_2 + e^- \quad (14)$$

$$\rightarrow HS_2^+ + H_2S + H_2 + H + e^- \quad (15)$$

$$\rightarrow H_2S_2^+ + H_2S + H_2 + e^- \quad (16)$$

$$\rightarrow H_3S_2^+ + H_2S + H + e^- \quad (17)$$

$$\rightarrow H_3S^+ + H_2S + HS + e^- \quad (18)$$

Nevertheless, the PIE curves for S_2^+, HS_2^+, $H_2S_2^+$, and $H_3S_2^+$ were found to be quite insensitive to changes in P_o at $T_o \approx 230$ K in the range of

$P_o \approx$ 200-460 Torr. Stemming from the expectation that the AEs of the above reactions are higher than those for the corresponding reactions (1)-(5), the existence of $(H_2S)_3$ and higher hydrogen sulfide clusters in the beam should not affect the AE measurements for fragment ions from $(H_2S)_2$. The finding that the AE for H_3S^+ is in accordance with the expected thermochemical value for reaction (4) can be taken as evidence in support of the above expectation.

The PIE curves for S_2^+, HS_2^+, $H_2S_2^+$, and $H_3S_2^+$ (uncorrected for isotopic contributions) in the region ~650-1000 Å obtained with $P_o \approx$ 350 Torr and $T_o \approx$ 230 K are shown in Figs. 5(a), (b), (c), and (d), respectively. Other than the spectrum for S_2^+, the PIE curves for HS_2^+, $H_2S_2^+$, and $H_3S_2^+$ all suffered from the sulfur isotopic effects. However, because the intensities for the S_2^+, HS_2^+, $H_2S_2^+$, and $H_3S_2^+$ ions are similar and the natural abundances for ^{33}S and ^{34}S are small, the corrections due to isotopic contributions should only introduce minor modifications of the spectra.

The PIE curve shown in Fig. 5(a) represents the true PIE spectrum for S_2^+. Within the sensitivity of the apparatus, an upperbound for the AE for S_2^+ was determined to be 12.98 eV (955 Å). Based on the known values for $\Delta H^o_{f0}(S_2^+)$ [38] and $\Delta H^o_{f0}((H_2S)_2)$ (Table 1), the thermochemical threshold for the formation of S_2^+ by reaction (1) is predicted to be 11.07 eV (1120 Å). The difference of 1.91 eV (44 kcal/mole) between the latter value and the experimental threshold can be taken to be an upper limit for the activation energy for the formation of $S_2^+ + 2H_2$ from the reaction of $H_2S^+ + H_2S$.

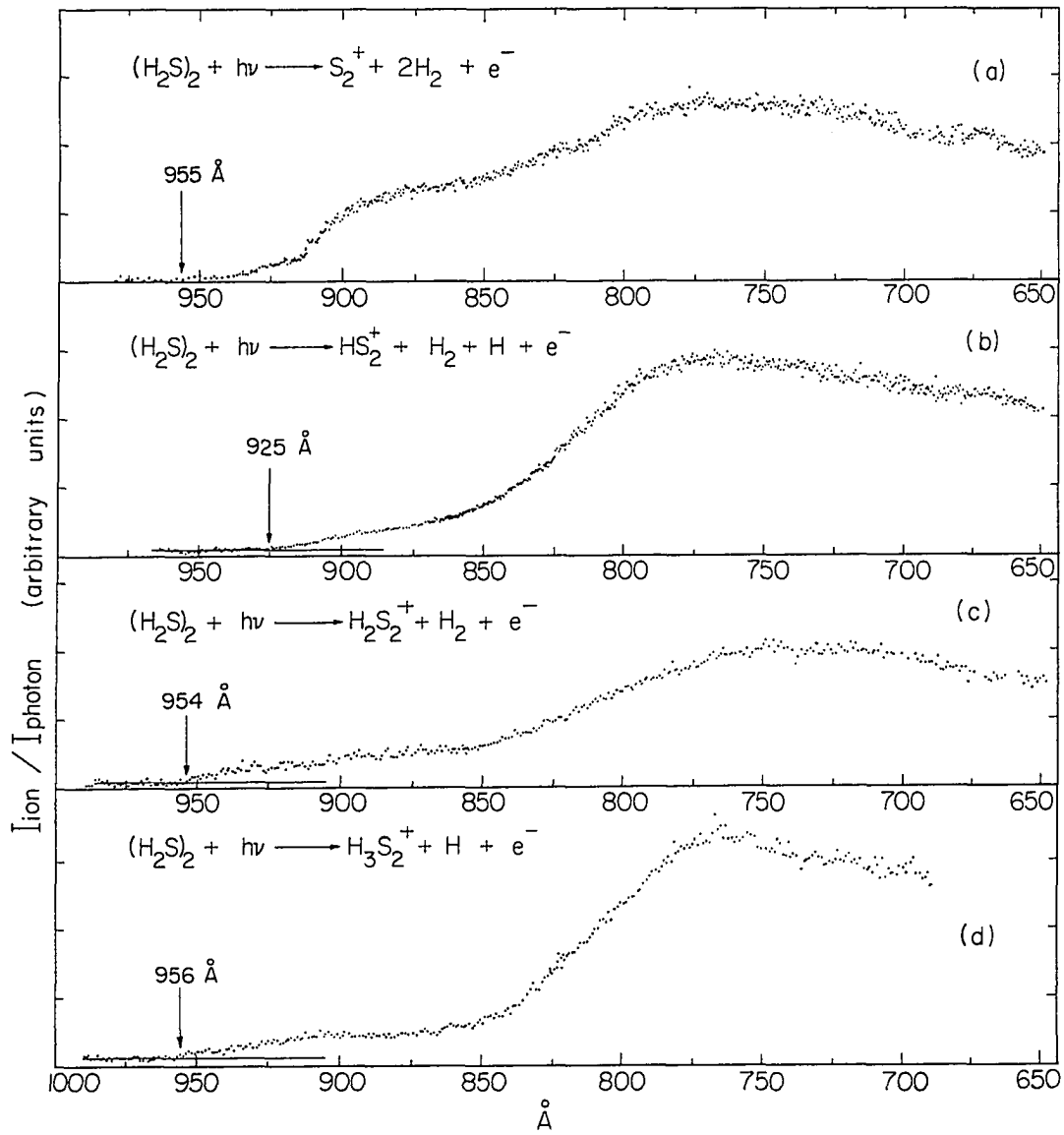

Figure 5. PIE curves for (a) S_2^+, (b) HS_2^+, (c) $H_2S_2^+$, and (d) $H_3S_2^+$ in the region ~650-1000 Å obtained with a wavelength resolution of 1.4 Å (FWHM). (Nozzle conditions: $P_o \approx 360$ Torr, $T_o \approx 230$ K)

In the case of the PIE spectrum for HS_2^+ (Fig. 5(b)), the isotopic contribution from the $^{32}S^{33}S^+$ ion near the threshold region (>900 Å) is more serious. After accounting for the contribution of $^{32}S^{33}S^+$, an upperbound for the AE for the formation of HS_2^+ by reaction (2) was estimated to be 13.40 eV (925 Å). The heat of formation for HS_2^+ is not known. By using the measured AE of HS_2^+ and thermochemical data for $(H_2S)_2$ and H [36], the heat of formation for HS_2^+ is estimated to be 248 kcal/mole. The previous observations of the reactions $S^+ + H_2S \rightarrow HS_2^+ + H$ and $HS_2^+ + H_2O \rightarrow H_3O^+ + S_2$ have placed $\Delta H^o_{f0}(HS_2^+)$ in the range of 232-249 kcal/mole [6]. Thus, the value for $\Delta H^o_{f0}(HS_2^+)$ deduced here is consistent with these limits.

The intensity of the mass 66 ions, which is mostly due to $H_2{}^{32}S_2^+$, is comparable to that of S_2^+. After correcting for minor contributions to the observed PIEs from $^{34}S^{32}S^+$ and $H^{33}S^{32}S^+$, an upperbound for the AE for reaction (3) is estimated to be 13.00 eV (954 Å). According to previous electron impact studies [37], $\Delta H^o_{f0}(H_2S_2^+)$ is in the range 239-246 kcal/mole. These limits imply the AE for $H_2S_2^+$ should be in the range ∿10.77-11.08 eV (1119-1151 Å). The comparison between the latter value and the experimental AE for $H_2S_2^+$ places an upper limit of ∿48 kcal/mole for the activation energy for the formation of $H_2S_2^+ + H_2$ from the reaction $H_2S^+ + H_2S$.

Since the intensity for $H_3S_2^+$ is greater than that of $H_2S_2^+$ and HS_2^+ in the region ∿700-1000 Å (see Fig. 3), the contributions from $H_2{}^{22}S^{33}S^+$ and $H^{32}S^{34}S^+$ to the PIE spectrum for $H_3S_2^+$ (Fig. 5(d)) are minor. The AE for the formation of $H_3S_2^+$ from reaction (5) was found to

be 12.97 eV (956 Å). The heat of formation of $H_3S_2^+$ has not been reported previously. The measured AE for $H_3S_2^+$ makes possible the calculation of a value of 238 kcal/mole for $\Delta H^o_{f0}(H_3S_2^+)$. In view of the large activation energies observed for the formation of S_2^+ and $H_2S_2^+$ from reaction (1) and (3), respectively, the values for $\Delta H^o_{f0}(HS_2^+)$ and $\Delta H^o_{f0}(H_3S_2^+)$ derived from AE measurements here are likely to be upper limits.

The reactions of HS^+ and S^+ with H_2S

$$HS^+ + H_2S \rightarrow H_3S^+ + S \quad (19)$$

$$\rightarrow HS_2^+ + H_2 \quad (20)$$

$$\rightarrow H_2S_2^+ + H \quad (21)$$

$$S^+ + H_2S \rightarrow S_2^+ + H_2 \quad (22)$$

$$\rightarrow HS_2^+ + H \quad (23)$$

have been observed previously [3,5,6]. The AEs for the formations of S^+ and HS^+ from H_2S by photoionization have been reported to have the values of 13.37 eV (927 ± 1.5 Å) and 14.30 eV (867 ± 1.5 Å), respectively. The PIE spectra for S_2^+, HS_2^+, $H_2S_2^+$, $H_3S_2^+$, and H_3S^+ only show minor resemblance to the PIE spectra for S^+ and HS^+. Based on the observations that the AEs for S_2^+, HS_2^+, $H_2S_2^+$, and $H_3S_2^+$ are close to the AEs of S^+ and HS^+ and that the intensities of S^+ and HS^+ produced in this region are much higher than that of $(H_2S)_2^+$, it is reasonable to suspect that the S_2^+, HS_2^+, and $H_2S_2^+$ ions might originate from reactions

(20)-(23). In order to examine the possible influence of these secondary reactions, the PIE curves for S_2^+, HS_2^+, and $H_2S_2^+$ were measured again in an experimental arrangement without differential pumping. This was achieved by removing the skimmer and placing the nozzle in the photoionization chamber. The distance between the nozzle and the photoionization center was shortened to approximately 2 cm instead of ∿4.5 cm when differential pumping is maintained. In this experimental arrangement, the background H_2S pressure in the photoionization chamber is slightly less than 10^{-4} Torr at $P_o \approx 250$ Torr. The signals for S_2^+, HS_2^+, and $H_2S_2^+$ were found to be more than 20 times higher than the observed signals with the differential pumping arrangement. The relative intensities for S_2^+, HS_2^+, and $H_2S_2^+$ measured at ∿810 Å were 1:0.35:0.16, respectively.

Figures 6(a), (b), and (c) show the PIE spectra for S_2^+, HS_2^+, and $H_2S_2^+$ in the region 600-975 Å obtained at $P_o \approx 250$ Torr and $T_o \approx 230$ K without the differential pumping arrangement. The PIE spectrum for S_2^+ shown in Fig. 6(a) is found to be nearly identical to that for S^+ [14], indicating that the secondary reaction (22) is mainly responsible for the formation of S_2^+. The PIE curve for HS_2^+ shown in Fig. 6(b) is also similar to the S^+ spectrum [14]. The hump starting at approximately 875 Å, which is close to the AE for HS^+ from H_2S, is likely to arise from the reaction $HS^+ + H_2S$. Thus, we conclude that HS_2^+ can be formed by reactions (20) and (23), a conclusion consistent with previous studies [3,5,6]. The ratio of the intensities for S_2^+ and HS_2^+ at 875 Å, which is below the AE for HS^+ from H_2S, is measured to be 3.3. This

Figure 6. PIE curves for (a) S_2^+, (b) HS_2^+, and (c) $H_2S_2^+$ in the region ~600-990 Å obtained without the differential pumping arrangement. (Experimental conditions: $P_o \approx 250$ Torr, $T_o \approx 230$ K, wavelength resolution = 1.4 Å (FWHM))

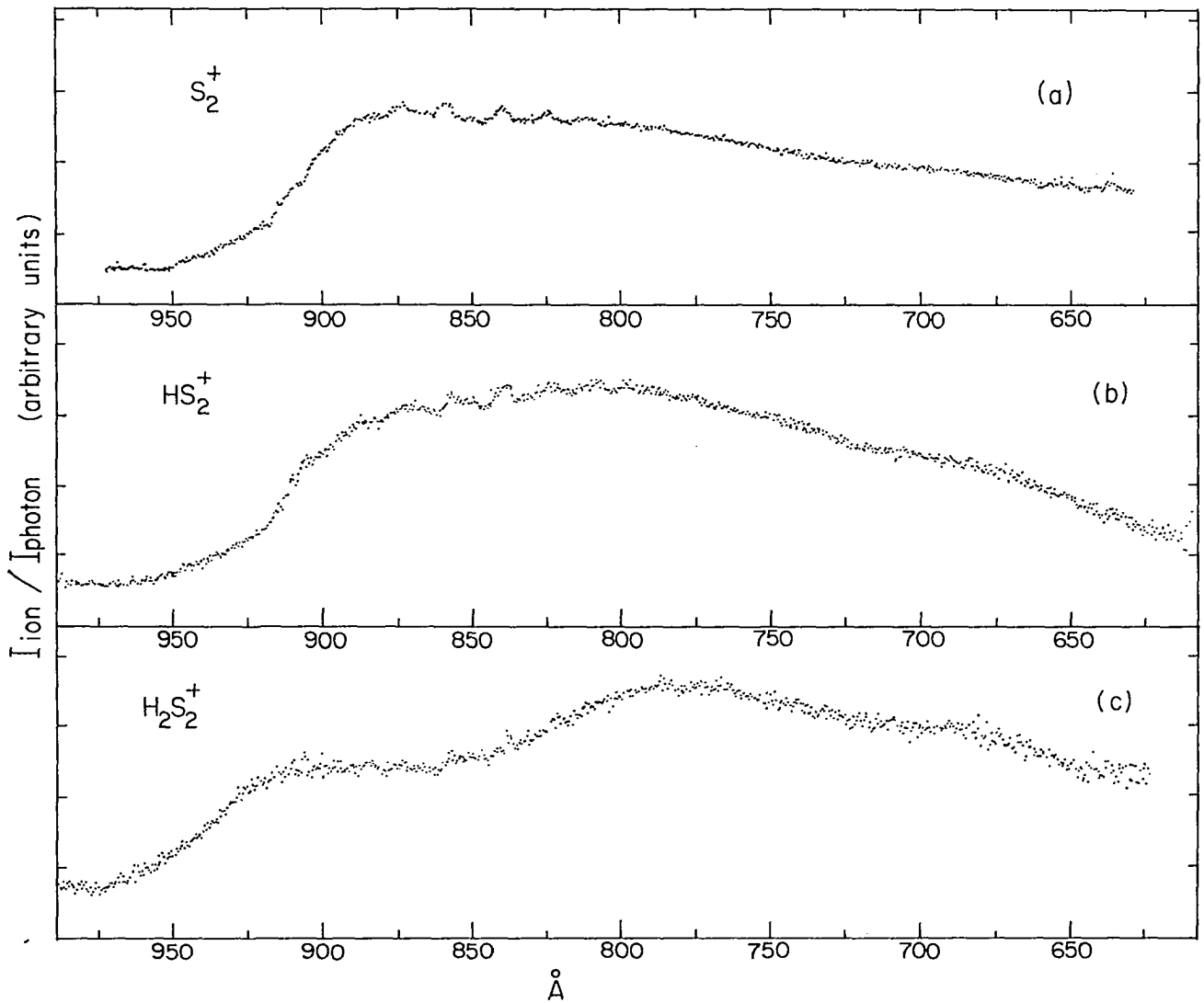
S_2^+
(a)
HS_2^+
(b)
$H_2S_2^+$
(c)
950
900
850
800
750
700
650
I ion / I photon (arbitrary units)
Å

value is also found to be in excellent agreement with previous reported values of 3.2 [3] and 3.8 [6]. The observed intensity for $H_2S_2^+$ at 875 Å, before corrections for the isotopic contributions, is only ∿11% that of S_2^+. Therefore, the finite PIEs observed in Fig. 5(c) at wavelengths longer than ∿875 Å are almost totally due to $H^{33}S^{32}S^+$ and $^{34}S^{32}S^+$. The further increase in PIE of $H_2S_2^+$ at wavelengths shorter than 870 Å can be attributed to reaction (21). In short, the above comparison shows that the formation of S_2^+, HS_2^+, and $H_3S_2^+$ by secondary reactions (20)-(23) have much greater cross sections than the corresponding reactions by $H_2S^+ + H_2S$. Moreover, the substantial differences observed between the spectra of S_2^+, HS_2^+, and $H_2S_2^+$ shown in Figs. 5(a)-(d) and those in Figs. 6(a)-(c) support the conclusion that reactions (20)-(23) contribute little to the spectra observed in Figs. 5(a)-(d). The above investigation also demonstrates the importance of using the differential pumping arrangement for the study of unimolecular decompositions of dimer and cluster ions such as reactions (1)-(6).

The adiabatic IEs for the $\tilde{A}^2A_1$ and $\tilde{B}^2B_2$ states of H_2S^+ obtained by photoelectron spectroscopy [30] are 12.777 eV (970 Å) and 14.643 eV (847 Å), respectively. The AEs for the S_2^+, $H_2S_2^+$ and $H_3S_2^+$ ions are found to be close to the IE of the $\tilde{A}^2A_1$ state. As the photon energy increases to approximately the IE of the $\tilde{B}^2B_2$ state, the PIE curves for the S_2^+, HS_2^+, $H_2S_2^+$, and $H_3S_2^+$ all exhibit further increases in PIE. Qualitatively, one may conclude that reactions (1)-(5) proceed with higher probabilities when the H_2S^+ moiety in $H_2S^+ \cdot H_2S$ is prepared in the $\tilde{A}^2A_1$ and $\tilde{B}^2B_2$ states than when H_2S^+ is formed in the $\tilde{X}^2B_1$ state.

Furthermore, since the productions of S^+ and HS^+ are believed to arise from fast predissociation of H_2S^+, it is likely that many of the fragmentation reactions might be stepwise processes such as

$$H_2S^+ \cdot H_2S \rightarrow S^+ \cdot H_2S + H_2 \rightarrow S_2^+ + 2H_2 \quad (24)$$

$$\rightarrow S^+ \cdot H_2S + H_2 \rightarrow HS_2^+ + H_2 + H \quad (25)$$

$$\rightarrow HS^+ \cdot H_2S + H \rightarrow HS_2^+ + H_2 + H \quad (26)$$

$$\rightarrow HS^+ \cdot H_2S + H \rightarrow H_2S_2^+ + 2H \quad . \quad (27)$$

In order to measure the relative reaction probabilities of reactions (1)-(5) as a function of ionizing photon energy without the interference of processes such as reactions (14)-(18), it is necessary to operate the H_2S nozzle beam under conditions which minimize the formation of hydrogen sulfide trimers and higher clusters. The intensities for $(H_2S)_2^+$, $H_3S_2^+$, H_3S^+, $H_2S_2^+$, HS_2^+, and S_2^+ were measured at $P_o \approx 200$ Torr and $T_o \approx 230$ K at wavelength intervals of 50 Å in the region 650-950 Å. Under these beam conditions, the intensities of $H_2S_2^+$, $(H_2S)_3^+$, and higher hydrogen sulfide cluster ions were all found to be within the noise level, indicating that the concentrations of $(H_2S)_n$, $n \geq 3$ were negligible. After careful corrections for isotopic contributions, the true intensities for $(H_2S)_2^+$, $H_3S_2^+$, H_3S^+, $H_2S_2^+$, HS_2^+, and S_2^+ were obtained. The differences in transmission of these ions through the mass spectrometer used in this experiment have not been corrected for. Since the masses of these ions with the exception of H_3S^+ differ only by a few mass units, the transmission factors are expected to have minor

effects on the measured relative intensities of $(H_2S)_2^+$, $H_3S_2^+$, $H_2S_2^+$, HS_2^+, and S_2^+. The relative abundances, $I((H_2S)_2^+/\Sigma$, $I(H_3S_2^+)/\Sigma$, $I(H_3S^+)/\Sigma$, $I(H_2S_2^+)/\Sigma$, $I(HS_2^+)/\Sigma$, and $I(S_2^+)/\Sigma$ for $(H_2S)_2^+$, $H_3S_2^+$, H_3S^+, $H_2S_2^+$, HS_2^+, and S_2^+, respectively, in percentage as a function of photon energy in the region 650-950 Å are plotted in Fig. 7. Here $I((H_2S)_2^+)$, $I(H_3S_2^+)$, $I(H_3S^+)$, $I(H_2S_2^+)$, $I(HS_2^+)$, $I(S_2^+)$ represent the true intensities of $(H_2S)_2^+$, $H_3S_2^+$, H_3S^+, $H_2S_2^+$, HS_2^+, and S_2^+, respectively, and Σ is the sum of $I((H_2S)_2^+)$, $I(H_3S_2^+)$, $I(H_3S^+)$, $I(H_2S_2^+)$, $I(HS_2^+)$, and $I(S_2^+)$. As shown in Fig. 7, $H_3S^+ + HS$ is found to be the dominant product channel with only minor variation in fragmentation probability in this region. This analysis also confirms the above conclusions that the $S_2^+ + 2H_2$, $HS_2^+ + H_2 + H$, $H_2S_2^+ + H_2$, and $H_3S_2^+ + H$ are weak product channels which have higher reaction probabilities when H_2S^+ in $H_2S^+ \cdot H_2S$ is formed in the $\tilde{A}^2A_1$ or $\tilde{B}^2B_2$ states.

In summary, the study of the unimolecular decomposition of $(H_2S)_2^+$ using the molecular beam photoionization method has allowed the unambiguous identification of the S_2^+, HS_2^+, $H_2S_2^+$, H_3S^+, and $H_3S_2^+$ ions as the primary product ions from the reactions of $H_2S^+ + H_2S$. From the AE and IE measurements of various ions, the energetics of HS_2^+, $H_3S_2^+$, $H_5S_2^+$, H_3S^+, $(H_2S)_2^+$, and $(H_2S)_3^+$ have been calculated. This study also reveals that the ion-molecule reactions between H_2S^+ and H_2S to form S_2^+, HS_2^+, $H_2S_2^+$, and $H_3S_2^+$ is strongly favored for H_2S^+ in the $\tilde{A}^2A_1$ and $\tilde{B}^2B_2$ states in comparison to the $\tilde{X}^2B_1$ state. Furthermore, the decompositions of the $H_2S^+ \cdot H_2S$ complexes to form S_2^+, HS_2^+, and $H_2S_2^+$ are likely to proceed by stepwise processes as shown in reactions (24)-(27).

Figure 7. The variations of the relative abundances for $(H_2S)_2^+$ (□), $H_3S_2^+$ (○), H_3S^+ (▽), $H_2S_2^+$ (X), HS_2^+ (●), and S_2^+ (+) as a function of the photon energy, Σ is the sum of $I((H_2S)_2^+)$, $I(H_3S_2^+)$, $I(H_3S^+)$, $I(H_2S_2^+)$, $I(HS_2^+)$, and $I(S_2^+)$, where $I((H_2S)_2^+)$, $I(H_3S_2^+)$, $I(H_3S^+)$, $I(H_2S_2^+)$, $I(HS_2^+)$, and $I(S_2^+)$ represent the intensities for $(H_2S)_2^+$, $H_3S_2^+$, H_3S^+, H_2S_2, HS_2^+, and S_2^+, respectively, after the corrections for isotopic contributions. I_i = $I((H_2S)_2^+$, $I(H_3S_2^+)$, $I(H_3S^+)$, $I(H_2S_2^+)$, $I(HS_2^+)$, or $I(S_2^+)$. (Experimental conditions: $P_o \approx 200$ Torr, $T_o \approx 230$ K, wavelength resolution 1.4 Å (FWHM))

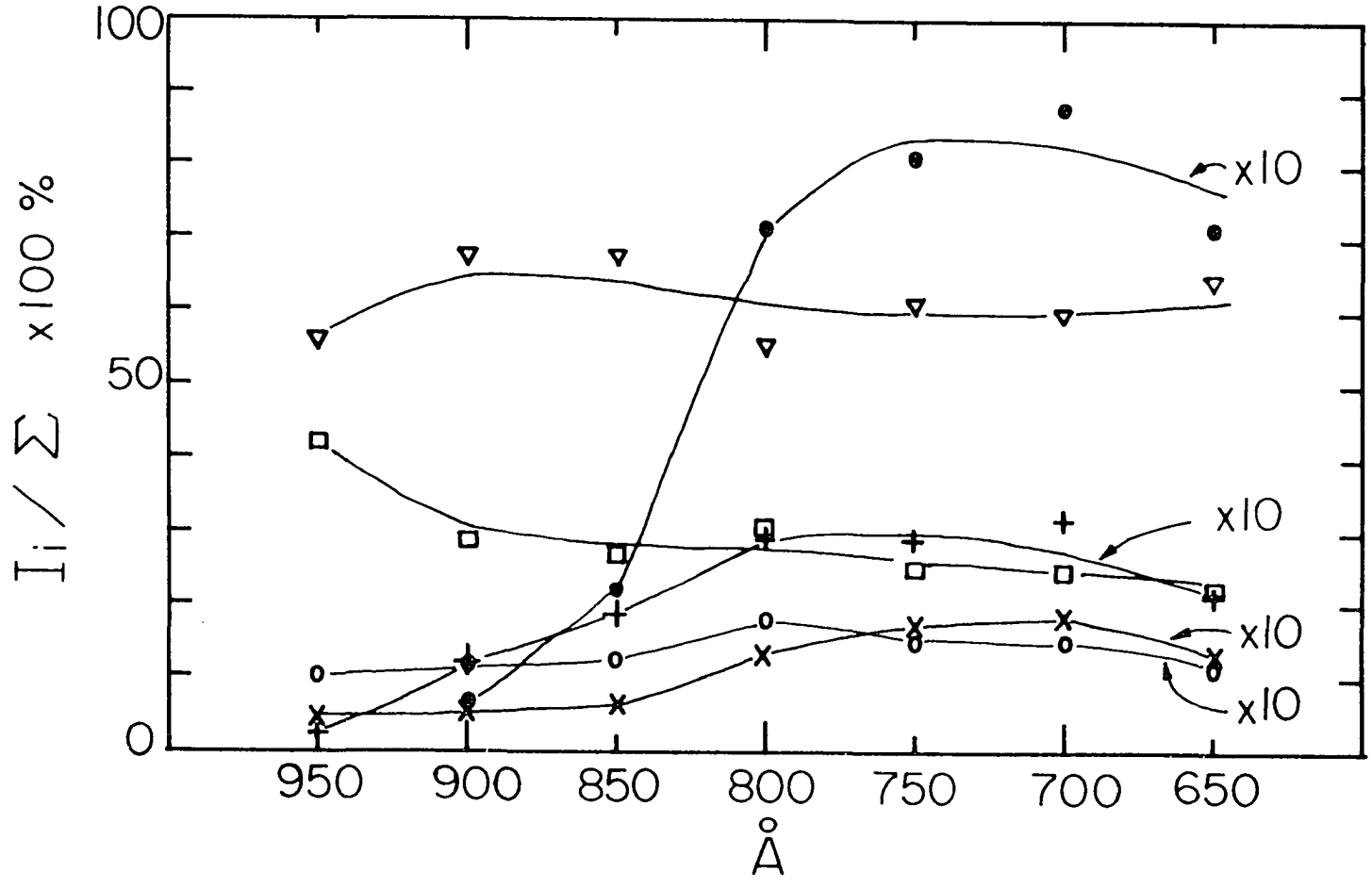
100
50
0
I_i / Σ x100 %
x10
x10
x10
x10
950
900
850
800
750
700
650
Å

References

1. W. E. W. Ruska and J. L. Franklin, Int. J. Mass Spectrom. Ion Phys. 3, 221 (1969).

2. S. K. Gupta, E. G. Jones, A. G. Harrison and J. J. Myher, Can. J. Chem. 45, 3107 (1967).

3. D. Smith, N. G. Adams and W. Lindinger, J. Chem. Phys. 75, 3365 (1981).

4. J. L. Beauchamp and S. E. Buttrill, Jr., J. Chem. Phys. 48, 1783 (1967).

5. A. G. Harrison, Int. J. Mass Spectrom. Ion Phys. 6, 297 (1971).

6. W. T. Huntress, Jr. and R. F. Pinizzotto, Jr., J. Chem. Phys. 59, 4742 (1973).

7. Y. Ono, S. H. Linn, H. F. Prest, M. E. Gress and C. Y. Ng, J. Chem. Phys. 74, 1125 (1981).

8. S. T. Ceyer, P. W. Tiedemann, C. Y. Ng, B. H. Mahan and C. Y. Ng, J. Chem. Phys. 70, 2138 (1979).

9. Y. Ono and C. Y. Ng, J. Chem. Phys. 77, 2947 (1982).

10. Y. Ono and C. Y. Ng, J. Am. Chem. Soc. 104, 4752 (1982).

11. C. Y. Ng, Adv. Chem. Phys. 52, 263 (1983).

12. Y. Ono, S. H. Linn, H. F. Prest, M. E. Gress and C. Y. Ng, J. Chem. Phys. 73, 2523 (1980).

13. Y. Ono, S. H. Linn, H. F. Prest, C. Y. Ng and E. Meischer, J. Chem. Phys. 73, 4855 (1980).

14. H. F. Prest, W.-B. Tzang, J. M. Brom, Jr. and C. Y. Ng, Int. J. Mass Spectrom. Ion Phys. 50, 315 (1983); V. H. Dibeler and S. K. Liston, J. Chem. Phys. 49, 482 (1968). Refer to Section I of Part I.

15. K. E. Schubert and R. D. Hudson, "A Photoelectric Atlas of the Intense Lines of the Hydrogen Molecular Emission Spectrum from 1025 to 1650 Å at a Resolution of 0.1 Å," Report No. ATN-64(9233)-2 (Aerospace Corp., Los Angeles, 1963).

16. G. Friedlander, J. W. Kennedy and J. M. Miller, "Nuclear and Radiochemistry" (Wiley, New York, 1964), Appendix E.

17. S. H. Anderson, T. Hirooka, P. W. Tiedemann, B. H. Mahan and Y. T. Lee, J. Chem. Phys. 73, 4779 (1980).

18. S. H. Linn, Y. Ono and C. Y. Ng, J. Chem. Phys. 74, 3348 (1981).

19. S. H. Linn, Y. Ono and C. Y. Ng, J. Chem. Phys. 74, 3342 (1981).

20. S. H. Linn and C. Y. Ng, J. Chem. Phys. 75, 4921 (1981).

21. E. A. Walters and N. C. Blais, J. Chem. Phys. 75, 4208 (1981).

22. J. Harada and N. Kitamura, J. Phys. Soc. Jpn. 19, 328 (1964).

23. F. Khoury and D. B. Robinson, J. Chem. Phys. 55, 834 (1971).

24. P. Seal and P. K. Bandyopadhyay, Indian J. Phys. 48, 684 (1974).

25. J. E. Lowder, L. A. Kennedy, K. G. P. Sulzmann and S. S. Penner, J. Quantum Spectrosc. 10, 17 (1970).

26. R. C. Kerns and L. C. Allen, J. Am. Chem. Soc. 100, 6587 (1978).

27. J. R. Sabin, J. Am. Chem. Soc. 93, 3613 (1971).

28. G. Leroy, G. Louterman-Leloup and P. Ruelle, Bull. Soc. Chim. Belg. 85(4), 219 (1976).

29. B. van Hensbergen, R. Block and L. Jansen, J. Chem. Phys. 76, 3161 (1982).

30. L. Karlsson, L. Mattsson, R. Jadrny, T. Bergmark and K. Siegbahn, Phys. Scr. 13, 229 (1976).

31. H. Masuko, Y. Morioka, M. Nakamura, E. Ishiguro and M. Sasanuma, Can. J. Phys. 57, 745 (1979).

32. C. Y. Ng, D. J. Trevor, P. W. Tiedemann, S. T. Ceyer, P. L. Kronebush, B. H. Mahan and Y. T. Lee, J. Chem. Phys. 67, 4235 (1977).

33. Y. Ono, E. A. Osuch and C. Y. Ng, J. Chem. Phys. 74, 1645 (1981).

34. J. Erickson and C. Y. Ng, J. Chem. Phys. 75, 1650 (1981).

35. S. Tomoda, Y. Achiba and K. Kimura, Chem. Phys. Lett. 87, 197 (1982).

36. JANAF Thermochemical Tables, Nat. Stand. Ref. Data Ser. 37, Nat. Bur. Stand., June 1971.

37. J. L. Franklin, J. G. Dillard, H. M. Rosenstock, J. T. Herron, K. Draxl and F. H. Field, Nat. Stand. Ref. Data Ser. 26, Nat. Bur. Stand., June 1969.

38. H. M. Rosenstock, K. Draxl, B. W. Steiner and J. T. Herron, J. Phys. Chem. Ref. Data 6, Suppl. 1 (1977).

39. R. Walder and J. L. Franklin, Int. J. Mass Spectrom. Ion Phys. 36, 85 (1980).

40. D. S. Marynick, K. Scanlon, R. A. Eades and D. A. Dixon, J. Phys. Chem. 85, 3364 (1981).

41. M. W. Chase, Jr., J. L. Curnutt, J. R. Downey, Jr., R. A. McDonald, A. N. Syverud and E. A. Valenzuela, J. Phys. Chem. Ref. Data 11, 695 (1982).

42. M. A. Haney and J. L. Franklin, J. Chem. Phys. 50, 2028 (1969).

43. J. L. Beauchamp and S. K. Butrill, J. Chem. Phys. 48, 1783 (1968).

44. K. Tanaka, G. I. Mackay and D. K. Bohme, Can. J. Chem. 56, 193 (1978).

45. L. Y. Wei and L. I. Bone, J. Phys. Chem. 78, 2527 (1974).

46. J. M. Hopkins and L. I. Bone, J. Chem. Phys. 58, 1473 (1973).

47. A comparison of values for the proton affinity of H_2S reported previously can be found in Ref. 39.

48. M. Meot-Ner and F. H. Field, J. Am. Chem. Soc. 99, 998 (1977).

PART II. THE ROTATING SOURCE CROSSED MOLECULAR BEAM APPARATUS

> The object renders in material form the preexistent intention that gave birth to it, and its form is accounted for by the performance expected of it even before it takes shape.
>
> Jacques Monod

Introduction

The experimental situation and corresponding design reflect the particular information sought in the collisional event. The theoretical interpretation of the physical observations refines our scientific insight and directs our interest. Thus, theory is the "guiding hand" of experiment and experiment is the "cutting edge" of theory. This principle of fruitful interaction between experiment and theory is readily apparent in the success of molecular beam scattering in providing detailed insight into elastic, inelastic, and reactive processes.

Consider the asymptotic states of the general collision

$$A(\vec{V}_A,\alpha) + B(\vec{V}_B,\beta) \rightarrow C(\vec{V}_C,\gamma) + D(\vec{V}_D,\delta) \quad . \qquad (1)$$

The collision transforms reactants A and B in $\vec{V}_A$ and $\vec{V}_B$ translational states and internal states α and β into products[1] C and D in γ and δ

---

[1]It may be that no change occurs in the identity (i.e., A = C and B = D) or internal state ($\alpha = \gamma$, $\beta = \delta$) of the participants and the collision (classically) altered only the velocities so the event is referred to as elastic. If again there is no change in identities but α and β change (to γ and δ here), the event was inelastic. Changes in identity and internal state qualify the collision as reactive.

internal states with velocities $\vec{V}_C$ and $\vec{V}_D$. In the laboratory perspective, the number of C species appearing in state γ per unit time with velocity $\vec{V}_C$ is

$$N^{LAB}_{C(\gamma)}(\vec{V}_C;\vec{V}_A,\vec{V}_B) = n_A(\alpha)n_B(\beta)|\vec{V}_A - \vec{V}_B|\tau_Z\{I^{CM}_{C(\gamma)}(\alpha,\beta \to \gamma,\delta,\vec{u}_C;|\vec{V}_A - \vec{V}_B|) \times \left[\frac{d\vec{u}_C}{d\vec{V}_C}\right] d\vec{V}_C\} \quad (2)$$

where $n_J(\rho)$ represents the number density of species J of internal state ρ in the interaction volume τ_Z, and $[d\vec{u}_C/d\vec{V}_C]$ is the Jacobian for transformation from the laboratory (LAB) to the center of mass (CM) frame [1,2,3] in which the C product has velocity $\vec{u}_C$. The connection to theory is made through the center of mass differential cross section, $I^{CM}_{C(\gamma)}(\alpha,\beta \to \gamma,\delta,\vec{u}_C;|\vec{V}_A - \vec{V}_B|)$, which is independent of the experimental specifics. $I^{CM}_{C(\gamma)}(....)$ contains all the dynamical information (connecting the initial to the final state) of the collision and to (re-) produce the CM differential cross section from first principles is the theorists' aspiration. Likewise, an apparatus which can, in the general case, produce and examine the experimental situation represented by Eq. (1) is the experimentalists' "Golden Fleece". However, as past experience has shown, increasing the degree of inquiry into the collision event dictates an overall increase in complexity and/or specialization of the experimental design. Easily obtained is angular information which requires only definition of trajectories prior to and post collision. The first "primitive" [4] reactive beam-beam experiment of Taylor and Datz [5] on K + HBr → KBr + H involved just that and revealed

"the preference for forward scattering" in the center of mass. "Not so primitive" [4] experiments involved the additional ability, and complexity, of velocity selection beginning with selection of one reactant (e.g., $K(\vec{V}_K) + CH_3I,C_2H_5I \rightarrow KI + CH_3,C_2H_5$ [6]), but eventually including both a reactant and a product (e.g., $K(\vec{V}_K) + CH_3I \rightarrow KI(\vec{V}_{KI}) + CH_3$ [7], $K(\vec{V}_K) + HBr,DBR \rightarrow KBr(\vec{V}_{KBr}) + H,D$ [8]). Among the corresponding experimental "rewards" were refined observation of the angular and energy dependence of the cross section and partitioning of the available energy. This led to the theoretical "payoffs" in development of explanations such as the 'rebound', 'stripping', etc. mechanisms for the alkali reactions [9,10] as well as stimulating advances in scattering theory and calculation [11]. Leaving the specialization of the "alkali age" required more diverse (e.g., noncondensable) reactant systems and, consequently, a more "universal" detector. Strenuous differential pumping and the electron bombardment ionizer [12,13] provided the passport.

A variety of apparati, the "supermachines", have appeared incorporating to some degree these two features, however, a particularly successful arrangement has been the in-plane rotating detector apparatus of Y. T. Lee, J. D. McDonald, P. R. LeBreton, and D. R. Herschbach [14]. Mimicry alone serves as testament [15,16,17]. Since this apparatus elegantly manifests the general considerations of beam-beam experiments, it shall be described in detail to illustrate the design criteria.

References

1. R. K. B. Helbing, J. Chem. Phys. 48, 472 (1968) and J. Chem. Phys. 50, 4123 (1969).

2. T. T. Warnock and R. B. Bernstein, J. Chem. Phys. 49, 1878 (1968) and J. Chem. Phys. 51,

3. G. L. Catchen, J. Husain and R. N. Zare, J. Chem. Phys. 69, 1737 (1978).

4. D. R. Herschbach, in "Reactive collisions of thermal neutral systems", Molecular Beams and Reaction Kinetics, edited by Charles Schlier (Academic Press, New York, 1970).

5. E. H. Taylor and S. Datz, J. Chem. Phys. 23, 1711 (1955).

6. D. R. Herschbach, J. Chem. Phys. 34, 1842 (1961).

7. A. M. Rulis and R. B. Bernstein, J. Chem. Phys. 57 5497 (1972).

8. K. T. Gillen, C. Riley and R. B. Bernstein, J. Chem. Phys. 50, 4019 (1967).

9. J. L. Kinsey, International Review of Science: Phys. Chem. 9, 173 (1972).

10. R. Grice, "Reactive Scattering" in Advances in Chemical Physics (J. Wiley, New York, 1975), Vol. XXX.

11. M. Karplus and L. M. Raff, J. Chem. Phys. 41, 1267 (1964).

12. R. Weiss, Rev. Sci. Instr. 32, 397 (1961).

13. G. O. Brink, Rev. Sci. Instr. 37, 857 (1966).

14. Y. T. Lee, J. D. McDonald, P. R. LeBreton and D. R. Herschbach, Rev. Sci. Inst. 40, 1402 (1969).

15. C. F. Carter, M. R. Levy and R. Grice, J. Chem. Soc. Faraday Disc. 55, 277 (1973).

16. R. Behren, Jr., Ph.D. Dissertation, University of California, Berkeley, CA, 1975.

17. Y. T. Lee, Physics of Electronic and Atomic Collisions, VII I.C.P.E.A.C. (North-Holland, Amsterdam, 1971), p. 357.

SECTION I. GENERAL CONSIDERATIONS AND DESIGN CRITERIA

Signal Considerations

The in-plane scattering situation (for unselected beams) is shown in Fig. 1. Source apertures define the beams and collision volume from which the scattered particles are observed by a detector similarly defined. Ideally, the detector signal would be solely due to the scattering between the species of the two beams in the interaction zone. However, in reality, there are background considerations due to the nonzero pressures experienced by the beams and the detector.

In the collision region, typical thermal beam densities (n_i) correspond to about 10^{-5} Torr. If the total cross section for some event (σ_{TOT}) is 1 $\mathring{A}^2$ and the collision volume τ_Z is $\sim 10^{-3}$ cm^3, the total number of scattered particles per second N_S^{TOT} is (refer to Eq. (2))

$$N_S^{TOT} = n_A n_B \sigma_{TOT} v \tau_Z \tag{3}$$

$$= \left(\sim \frac{10^{11} \#}{cm^3} \right) \left(\frac{10^{11} \#}{cm^3} \right) (10^{-16} \text{ cm}^2) \left(\frac{10^4 \text{ cm}}{s} \right) (10^{-3} \text{ cm}^3)$$

$$= 10^7 \text{ product species per second}$$

which corresponds to a pressure of $\sim 10^{-7}$ Torr in the collision zone. A detector of effective area A_d equal to 0.25 cm^2 a distance 25.0 cm from the collision region would see the product pressure as $\sim 10^{-12}$ Torr (or $\sim 10^2$ product molecules arrive per second). 'Loss' of product molecules and angular information by secondary collisions is minimized by low ambient pressures ($\sim 10^{-7}$ Torr in the collision chamber), yet

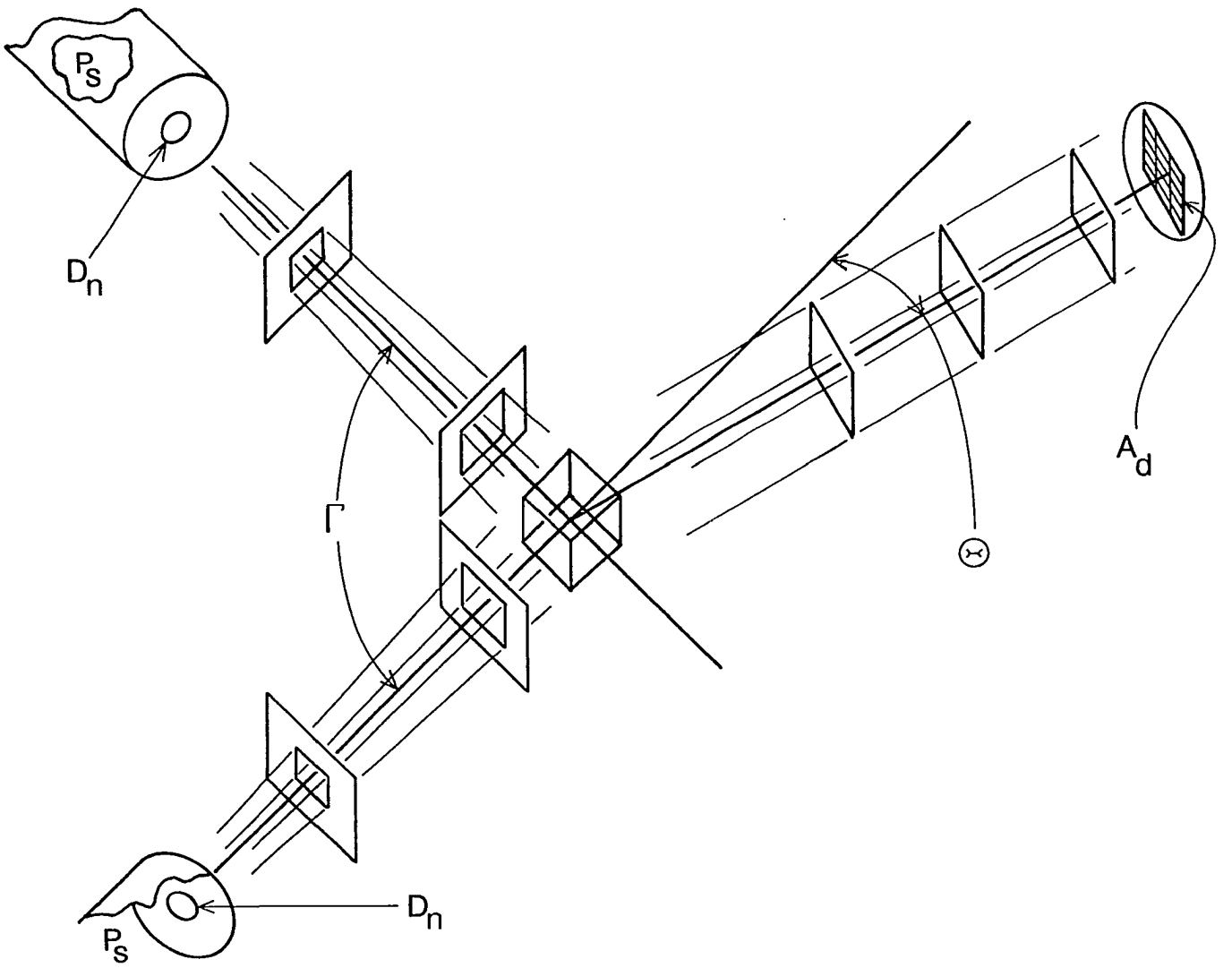

Figure 1. Schematic of the in-plane crossed beam experiment

interference from background remains unavoidable and must be assessed. Modulation (e.g., [1]) of one or both (e.g., [2]) of the beams is one scheme to take background into account.

Modulating a beam chops the detector count rate into that of an 'open' channel in which both the signal and background contribute, and a 'closed' channel ascribed to background. The number of counts during a counting time t in the closed channel is

$$N^C = bt$$

where b is the background count rate, and in the open channel

$$N^O = (s + b)t$$

where s is the signal count rate. The ratio of the signal to noise (r) indicates experimental feasibility. Because the signal and background are small, their random fluctuations are the limiting source of noise (i.e., thus, the 'error' in N is $N^{1/2}$). For a counting time t, the signal to noise ratio r is

$$r = \frac{N^O - N^C}{(N^O + N^C)^{1/2}}$$

$$= \frac{st}{[(s + 2b)t]^{1/2}} \qquad (4)$$

or

$$\frac{r^2}{t} \equiv R = \frac{s^2}{s + 2b} \quad . \qquad (5)$$

Because s and b are proportional to their actual densities, n_s and n_b, respectively, at the detector, e.g.,

$$s = \xi n_s$$

by the efficiency of the detector ξ, Eq. (5) may be written

$$R = \xi \left(\frac{n_s^2}{n_s + 2n_b} \right) \quad . \tag{6}$$

Evaluating the fractional change in R, $\Delta R/R$, due to a given fractional change for each of the experimentally controlled parameters gives [3]

$$\frac{\Delta R/R}{\Delta n_s/n_s} = 1 + \frac{2n_b}{n_s + 2n_B} \equiv \left(\frac{\Delta R}{R} \right)_s$$

$$\frac{\Delta R/R}{\Delta \xi/\xi} = 1 \equiv \left(\frac{\Delta R}{R} \right)_\xi$$

$$\frac{\Delta R/R}{\Delta n_b/n_b} = - \frac{2n_b}{n_s + 2n_b} \equiv \left(\frac{\Delta R}{R} \right)_b \quad .$$

On the basis of the improvement in the signal-to-noise for a fixed counting time, these can be ordered

$$\left(\frac{\Delta R}{R} \right)_s > \left(\frac{\Delta R}{R} \right)_\xi > \left(\frac{\Delta R}{R} \right)_b \quad . \tag{7}$$

The implication is that in attempting to improve, or in facing design compromises for an experiment, one gains most by improving the scattered signal, next by increasing detector efficiency, and to a lesser extent by lowering the background. This is a statement of the pertinent design criteria. And, therefore, intense beams, sensitive detection,

and low backgrounds via strong pumping becomes the crossed beam experimental design strategy.

Source Considerations

Intense sources represent the compromise between high throughputs and available pumping speed. From the viewpoint of loss due to beam-background scattering, the pumping requirements for sources becomes apparent.

In a region where the mean free path is $\bar{\ell}$, the probability a particle will successfully travel a distance ℓ unaffected is

$$P(\ell,\bar{\ell}) = \exp\{-\ell/\bar{\ell}\} \quad . \tag{8}$$

At room temperature, the product of the mean free path $\bar{\ell}$ (in cm) and the pressure P (in Torr) in a region is on the order of

$$\bar{\ell} \cdot P \simeq 5 \cdot 10^{-3} \text{ cm Torr}$$

(for species about the size and weight of Ar or O_2). Thus, the probability of being transmitted becomes

$$P(\ell,P) = \exp\{-\frac{\ell \cdot P}{5 \cdot 10^{-3} \text{ cm Torr}}\} \quad . \tag{9}$$

If a beam is to traverse, for instance, 5 cm from the source orifice to the first collimating slit with less than 10% attentuation, a background pressure of about 10^{-4} Torr is required in that region. An effusive source is restricted, by definition (e.g., [4,5]), such that the mean free path behind the nozzle orifice is about an order of magnitude greater than the characteristic orifice dimension, D_N:

$$\bar{\ell}\{P_S\} = \bar{\ell}\{P_{EB}\} \gtrsim 10\ D_N$$

where $\bar{\ell}\{P_S\}$ is the mean free path at a (source) pressure P_S which, for an effusive beam, is P_{EB}. Therefore, effusive source throughputs Q_{EB} are less than or equal to 10^{-2} Torr liter per second (hereafter Torr l s^{-1}) and moderate effective pumping speeds S_{eff} achieve the necessary pressure and, thereby, high transmissions:

$$Q_{EB} \div P = S_{eff} \tag{10}$$

$$(10^{-2}\ \text{Torr l s}^{-1}) \div (10^{-4}\ \text{Torr}) = 10^{2}\ \text{l s}^{-1} \quad .$$

However, the low throughput generates a correspondingly low intensity (number density or pressure) for the beam species at the collision region ($\sim 10^{15}$ species cm^{-2} s^{-1}, $\sim 10^{11}$ species cm^{-3}, $\sim 10^{-6}$ Torr). On the other hand, nozzle sources are not similarly constrained and operate at high source pressures (i.e., the nozzle source pressure P_N is such that $P_N \simeq 1000\ P_{EB}$ and so $\bar{\ell}\{P_N\} << D_N$), hence, with large throughputs

$$Q_N \gtrsim 1\ \text{Torr l s}^{-1} \quad .$$

Thus, nozzle beams offer one or two orders of magnitude higher intensities, but also the concomitant problem of removing large quantities of gas. If 'all' the gas were to be removed to a pressure of 10^{-4} Torr in one 'stage' of pumping, after the source orifice and before the first defining slit, an unrealistic effective pumping speed would be required; $S_{eff} > 10^{4}$ l s^{-1}. Mechanical considerations, available pumping speed, and expense (see Appendix A) make this an unprofitable prospect.

Reasonable effective pumping speeds are of the magnitude 10^3 l s^{-1}, so apparently the dilemma faced is either to lower the throughput and sacrifice intensity or suffer the higher background and accompanying attenuation - a losing proposition either way.

Recasting the Eq. (9) in terms of the effective pumping speed, S_{eff} and throughput reveals an alternative

$$P(\ell,Q_N,S_{eff}) = \exp\{ - \frac{\ell \cdot [Q_N \div S_{eff}]}{\bar{\ell} \cdot P} \}$$

$$\exp\{ - \frac{\ell \cdot [(1 \text{ Torr l } s^{-1}) \div (10^3 \text{ l } s^{-1})]}{5 \cdot 10^{-3} \text{ cm Torr}} \} \quad .$$

By decreasing the length of travel in the region of higher pressure, here from 5 cm in P = 10^{-4} Torr to 0.5 cm in P = 10^{-3} Torr, high transmission (>90%) is maintained. Moving the nozzle closer to the first aperture has two effects. First, the density of flowing gas at the first defining aperture increases necessitating special mechanical design of this aperture; i.e., development of the skimmer [6,7]. Second, the (remaining) throughput problem reappears, although greatly diminished in magnitude, between the first aperture (now the skimmer) and the second aperture. Therefore, in a nozzle source, the apertures have the additional function of dividing the gas load into <u>different</u> regions and, thereby, tractable amounts. The success of nozzle sources and their superiority over effusive sources is dependent on strong <u>differential</u> pumping.

Detector Design Considerations

From Eq. (5), it can be seen that counting time t, for a particular signal-to-noise ratio r, goes as

$$t \propto r^2/s^2 \qquad b >> s$$

for the background b being larger than the signal s, while if they are comparable

$$t \propto r^2/s \qquad b \sim s \quad .$$

If the detector were exposed directly to the (main) collision chamber, b >> s and unreasonably long counting times would be required. As illustrated for the sources, differential pumping can lower the ambient pressure at the detector.

For example, if the outer detector aperture exposed to the (main) collision chamber pressure of 10^{-7} Torr is of area 0.25 cm^2, the throughput is approximately $3 \cdot 10^{-7}$ Torr l s^{-1}. If behind that aperture and before the next, an effective pumping speed[1] of 50 l s^{-1} is available, this (first) region will have a pressure of $6 \cdot 10^{-9}$ Torr which is lower than the main chamber pressure by an order of magnitude. If two more stages of differential pumping are provided, the ambient pressure at the detector is reduced to $\sim 10^{-11}$ Torr and now s $\sim$ b. Note, this is the total pressure based on total effective pumping speeds. In actuality,

---

[1]The necessary cleanliness of the detector and for ultra-high vacuum in the detector chamber requires specialized pumping techniques for which high pumping speeds are hard to come by. Refer to Appendix A.

pumping speeds are species dependent[1]. So, in fact, the situation may be more or, possibly less, favorable depending on the actual species pumping speed.

This is of special importance in view of the fact that previous considerations of signal and background are species specific. It is the ambient partial pressure of the species being detected that produces the background. The relative ease of the 'alkali age' becomes readily apparent. High pumping speeds, via liquid nitrogen cryopumping, were readily available to suppress interfering background and the highly specific and efficient ($\xi > 90\%$) surface ionization detector [8] obviated apparati complexities introduced by multiple stages of differential pumping. Advancing to 'universality' required the advent of high, nonspecific pumping speeds and complex apparati to efficiently exploit them as well as universal detection. The electron bombardment ionizer enables universal detection, although with low efficiency ($\xi \sim 0.1\%$), and in conjunction with mass discrimination high selectivity for the species of interest. It can now be seen how universality effects design.

The Rotating Detector Apparatus

As stated in the Introduction to this Part, the apparatus of Lee, McDonald, LeBreton and Herschbach [9] represents a particularly successful implementation of the critical criteria described above. Vertical and

---

[1]For example, cryogenic pumping with liquid nitrogen 'removes' a negligible amount of helium while for condensables (e.g., the alkali halides of the alkali age), the pumping speed is proportional to the area at 77°K (which can be made as large as required.

horizontal cross sectional views are shown in Figs. 2a and 2b [9], respectively, and to aid visualization, a perspective drawing is provided in Fig. 3 [10]. This rotating detector apparatus (RDA), as well as noteworthy modifications in its descendants, will be described briefly.

Apparatus description

The beams generated by the sources cross at the fixed angle of 90 degrees in a (main) collision chamber pumped by a single gate-valved "10 inch" oil diffusion pump ($S \sim 4200$ l s^{-1}). Each source can be doubly differentially pumped. The first stage by a "6 inch" oil diffusion pump ($S \sim 2500$ l s^{-1}) {which in later designs was replaced by a "10 inch" oil diffusion pump ($S \sim 5300$ l s^{-1})}. The second stage by a "4 inch" oil diffusion pump ($S \sim 1200$ l s^{-1}). Changing apertures in the source chambers alters the beam widths and collision volume.

Besides supporting the source chambers in rigid, 3.7 cm thick walls, the stainless steel main chamber has a 6.4 cm thick "lid" machined for a 63.5 cm inside diameter (i.d.) bearing and two differentially pumped seals. The bearing supports the rotating plate of the detector chamber which is sealed [11] by two graphite embedded Teflon 'Ted Rings' seals. Three contiguous differentially pumped regions, each by a 50 l s^{-1} ion pump {increased to 220 l s^{-1} in later larger versions}, compose the detector chamber. The third or, innermost region, is also pumped by a cylindrical liquid nitrogen trap {supplemented in later apparati by helium cryopumping} to which a copper block has been vacuum brazed. The electron bombardment ionizer [12] is mounted on the copper block in the third region and the positive ions

Figure 2a. Vertical cross section of the Lee et al. rotating detector apparatus [9]. (A) - electron bombardment ionizer; (B) - quadrupole mass filter; (C) - ion counter; (D) - isolation valve; (D) - molecular beam source; (F) - beam flag; (G) - cold shield; (H) - to ion pumps; (J) - to oil diffusion pump; (K) - liquid nitrogen trap; (L) - ball bearing support of rotatable lid; (M) - rotating vacuum seal; and (N) - to liquid nitrogen reservoir

Figure 2b. Horizontal cross section of Lee et al. rotating detector apparatus [9] showing arrangement of differential pumping for detector and source chambers and beam geometry. The scanning range of the detector covers 140°, from 20° beyond the atom beam to 30° beyond the molecule beam

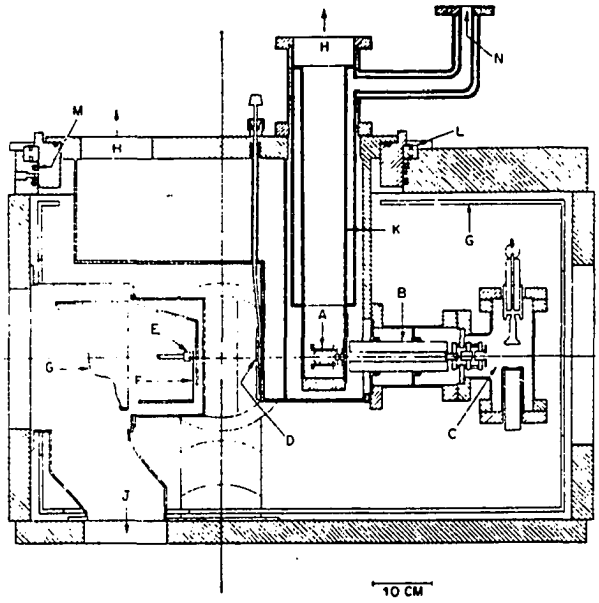
H
N
M
H
L
K
G
B
A
E
G
F
D
C
J
10 CM

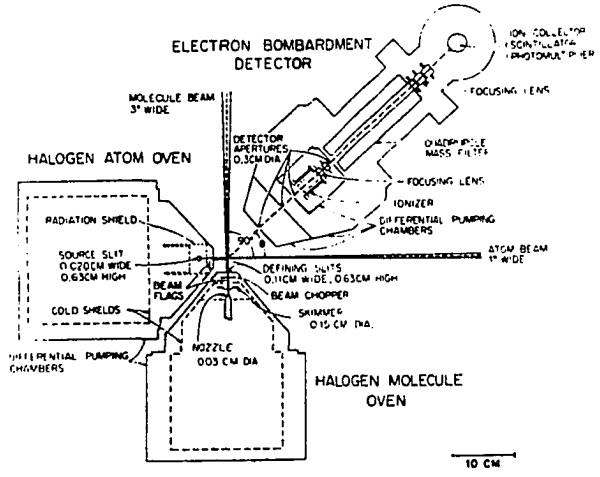
ELECTRON BOMBARDMENT
DETECTOR
MOLECULE BEAM
3° WIDE
HALOGEN ATOM OVEN
DETECTOR
APERTURES
0.3CM DIA
FOCUSING LENS
IONIZER
DIFFERENTIAL PUMPING
CHAMBERS
RADIATION SHIELD
90°
ATOM BEAM
1° WIDE
SOURCE SLIT
0.020CM WIDE
0.63CM HIGH
DEFINING SLITS
0.11CM WIDE, 0.63CM HIGH
BEAM
FLAGS
BEAM CHOPPER
COLD SHIELDS
SKIMMER
0.15 CM DIA.
NOZZLE
.003 CM DIA
HALOGEN MOLECULE
OVEN
10 CM

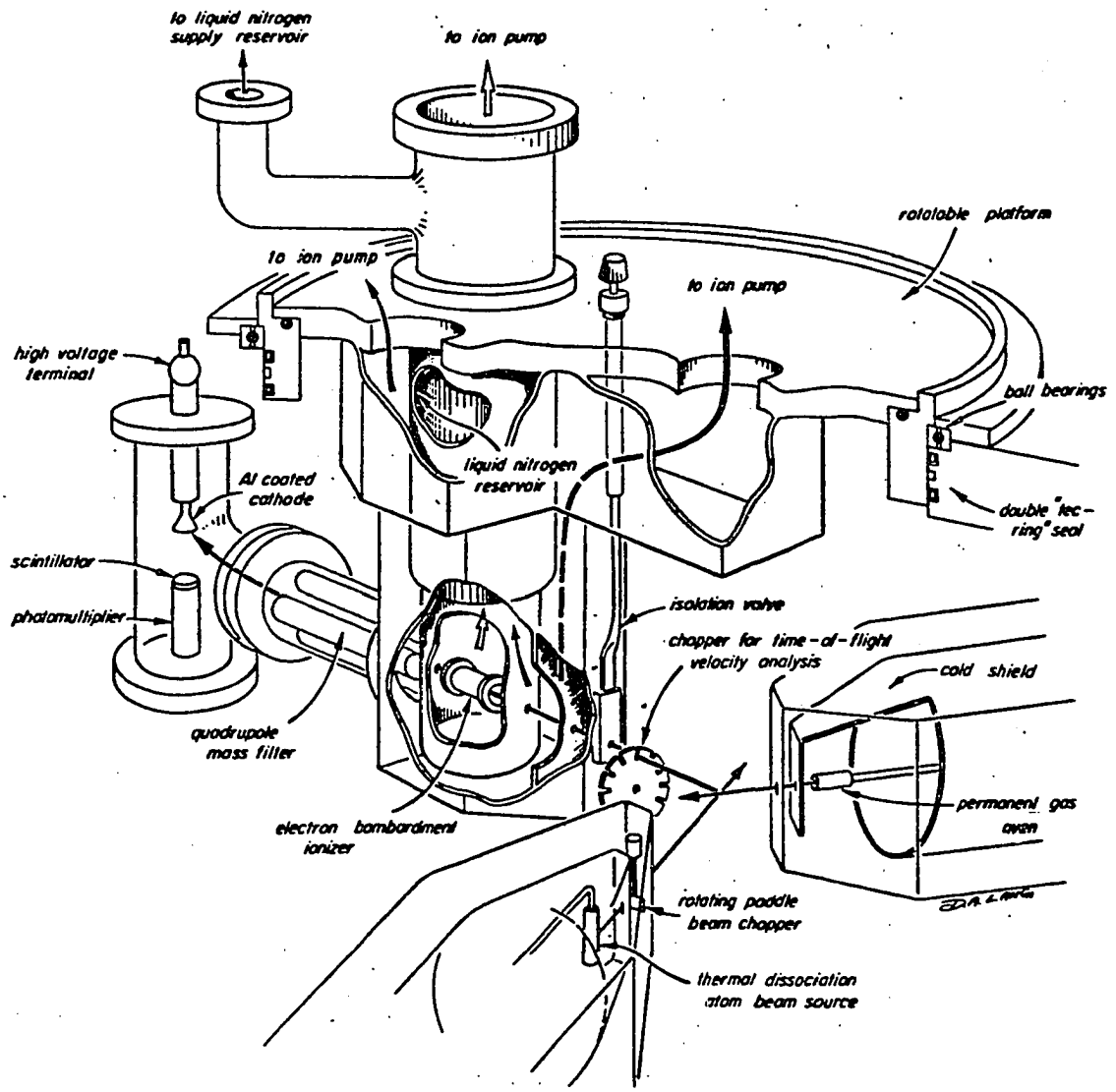

Figure 3. Perspective drawing of the Lee et al. rotating detector apparatus from McDonald et al. [10]

formed are injected into the second differentially pumped region where a quadrupole mass filter [13] sorts them according to mass-to-charge ratio before counting by a Daly ion scintillation counting system [14, 15]. Each of the three detector regions has changeable slits for altering angular resolution. Energetic resolution is accomplished by time-of-flight utilizing a single multi-slotted wheel prior to the first detector aperture and driven by a motor mounted on the bottom of the detector chamber.

Rotating detector apparatus advantages

The strong differential pumping in the source regions allowed by the fixed configuration provides intense beams and permits a variety of beam source designs (e.g., [16,17]) to be accommodated. Similarly, the strong differential pumping of the detector and its close proximity to the collision region has made studies with high angular resolution ($\sim$1/2 degree) over a large laboratory range ($\sim$140 degrees) of relatively low cross section events possible. The overall mechanical convenience of the design in operation and assembly is high.

Rotating detector apparatus disadvantages

The fixed beam intersection angle of 90 degrees requires utilizing heated and/or seeded (e.g., [18]) beam techniques to change the relative velocity of the collision. Heating can alter the beam character, while seeding necessarily modifies beam composition. Ultimately, the fixed crossing angle limits the available kinetics and kinematics of the collision. The detector differential pumping is inherently limited

both in nature and degree by the rotating lid. Another more severe limitation of the rotating detector is the fixed ionizer position; a consequence of the fixed bearing diameter. Since the scattered signal is proportional to the inverse square of the detector distance L, and assuming the background is unchanged with L, the counting time t for a signal-to-noise ratio r goes as

$$R^{-1} = \frac{t}{r^2} \propto L^2 \left[1 + 2 \left(\frac{b}{s} \right) \right] \quad .$$

In terms of the prior formulation, it can be shown

$$\left| \frac{\Delta R/R}{\Delta n_s/n_s} \right| = \left| \frac{\Delta R/R}{\Delta L/L} \right|$$

thus, emphasizing, although expectedly, the importance of detector distance. Even in the course of a single experiment, the scattered intensity can vary by $\sim 10^3$ (e.g., the elastic scattering studies [19]). Therefore, the inescapable experimental compromise, that must be made on a case by case basis, between the desired angular and/or energetic resolution and 'reasonable' counting times based on signal and noise is greatly restricted. Greater time-of-flight resolution via a longer flight path is obtained only by the expensive and formidable task of the design and construction of another larger apparatus. Further, age has set in; the design is about fifteen years old and new approaches have evolved as is the usual course of science. Most noteworthy are the ever increasing capabilities of lasers [20]. The RDA detector design is based on the electron bombardment ionizer; the youthful and promising

detection scheme of that time. However, this limits the ability of the apparatus to incorporate new schemes such as those involving laser techniques. It is time for crossed beam apparatus design to evolve.

References

1. J. N. Smith and W. L. Fite, Proceedings of the Third International Symposium on Rarefied Gas Dynamics (Academic Press, New York, 1963), Vol. I, p. 430.

2. E. W. Rothe and R. K. B. Helbing, J. Chem. Phys. 49, 4750 (1968).

3. J. L. Kinsey, M.T.P. International Review of Science, edited by J. C. Polanyi (University Park Press, Baltimore, 1972), Vol. 9, p. 173.

4. L. B. Loeb, The Kinetic Theory of Gases (Dover Publications, Inc., New York, 1961), 3rd Ed.

5. N. F. Ramsey, Molecular Beams (Oxford University Press, London, 1956).

6. J. B. Anderson, R. P. Andres and J. B. Fenn, in Advances in Chemical Physics, edited by J. Ross (J. Wiley and Son, New York, 1966), Vol. X, p. 275.

7. J. B. Anderson, in Molecular Beams and Low Density Gasdynamics, edited by P. P. Wegener (M. Dekker, Inc., New York, 1974).

8. I. Langmuir and K. H. Kingdon, Proc. Roy. Soc. (London) A107, 61 (1925) and J. B. Taylor, Z. Physik 57, 242 (1929).

9. Y. T. Lee, J. D. McDonald, P. R. LeBreton and D. R. Herschbach, Rev. Sci. Instr. 40, 1402 (1969).

10. J. D. McDonald, P. R. LeBreton, Y. T. Lee and D. R. Herschbach, J. Chem. Phys. 56, 769 (1972).

11. The original design of the sealing of the rotating lid: D. E. Armstrong and N. C. Blais, Rev. Sci. Instr. 34, 319 (1963). For a recent design see: D. J. Auerbach, C. A. Becker, J. P. Cowin and L. Wharton, Rev. Sci. Instr. 49, 1518 (1978).

12. G. O. Brink, Rev. Sci. Instr. 37, 857 (1966).

13. W. Paul and M. Raether, Z. Physik 140, 262 (1955).

14. N. R. Daly, Rev. Sci. Instr. 31, 264 (1960).

15. H. M. Gibbs and E. D. Commins, Rev. Sci. Instr. 37, 1385 (1966).

16. S. J. Sibener, R. J. Buss, C. Y. Ng and Y. T. Lee, Rev. Sci. Instr. 51, 167 (1980).

17. J. M. Farrar and Y. T. Lee, J. Chem. Phys. 56, 5801 (1972).

18. J. B. Anderson, R P. Andres and J. B. Fenn, in Advances in Chemical Physics, edited by J. Ross (J. Wiley and Son, New York, 1966), Vol. X, p. 308.

19. C. H. Chen, P. E. Siska and Y. T. Lee, J. Chem. Phys. 59, 601 (1973).

20. Physics Today, Vol. 33, No. 11, November 1980, Special Issue - Laser Chemistry.

SECTION II. THE ROTATING SOURCE APPARATUS

Another approach to in-plane molecular beam scattering is via rotating sources and a stationary detector chamber. Some early 'primitive' effusive beam apparati used ovens attached to a single rotating lid (e.g., [1]). Advancing to nozzle sources requires more strenuous differential pumping, but mechanical problems associated with this pumping (e.g., moving diffusion pumps) have limited previous modern apparati to a single stage of source pumping. This deficiency greatly limits source character. Continuous sources suffer reduced intensity and/or higher background. Pulsed sources surmount throughput problems but are limited in, among other things, universality. The prospect of sacrificing variety in the beam sources is very unattractive. And the previous arguments concerning signal demonstrate losses in source intensity are also highly undesirable. Clearly, source differential pumping must be incorporated.

Although source design presents a problem, detector chamber considerations are very encouraging. A stationary chamber permits great freedoms in terms of the nature and degree of pumping desired. Also, some of the (aforementioned) problems associated with the rotating detector apparatus detection scheme become soluble.

With this in mind, a rotating source crossed beam apparatus has been designed, fabricated and, to an advanced stage, assembled incorporating electron bombardment ionization as a universal detection tool. The sources are both doubly differentially pumped and the detector chamber is triply differentially pumped. A brief description of the

mechanical arrangement and vacuum system is given, followed by operational considerations, specifically resolution, unique to this particular apparatus.

Apparatus Description

On the basis of the vacuum system, the rotating source apparatus (RSA) can be divided in two; the main and source chambers and the detector chamber. For clarity, they will be described separately and throughout this discussion, emphasis will be on the major mechanical and vacuum features. Mechanical details may be found by reference to the original drawings [2] which are listed by number (RSM-XXXX) for important items. Model numbers of commercially available items as well as the names and locations of the fabricators of custom items are included as references. All figures are to scale, however, a certain degree of restraint has been used in order to aid comprehensibility so, in general, they are schematic and not meant to substitute for the original drawings.

Main and source chambers

Schematic horizontal and vertical cross sectional views emphasizing the main and source chambers are shown in Figs. 1a and 1b.

The main chamber (RSM-MC007) is essentially a rectangular box 128.3 cm in length, 147.3 cm in height, and 66.0 cm wide fabricated (RSM-MC006) [3] with 3.8 cm thick 304L stainless steel plate. The thickness of the plates and their arrangement minimize distortion, thereby, guaranteeing alignment integrity is maintained after pump down. Access to the interior is through the flanged open end, hereafter the

Figure 1a. Horizontal cross sectional view of the rotating source apparatus. Indicated in the figure are:

DC - the detector chamber within which 1d, 2d, and 3d indicate the first, second, and third detector regions

ES - the east beam source chamber for which the first and second stages of differential pumping are indicated by 1s and 2s, respectively

WS - the west beam source chamber pointing upwards and positioned at 90° to the east beam source chamber

RP - rotating plate

GD - worm gear drive

SC - aluminum source chamber

IP - intermediate plate

DS - second stage source differential seal

CD - (33.0 cm x 27.9 cm) differential pumping cross

6 - 2500 l s^{-1} diffusion pump

400 - 8000 l s^{-1} diffusion pump

Q - indicates the detail shown in Figure 2

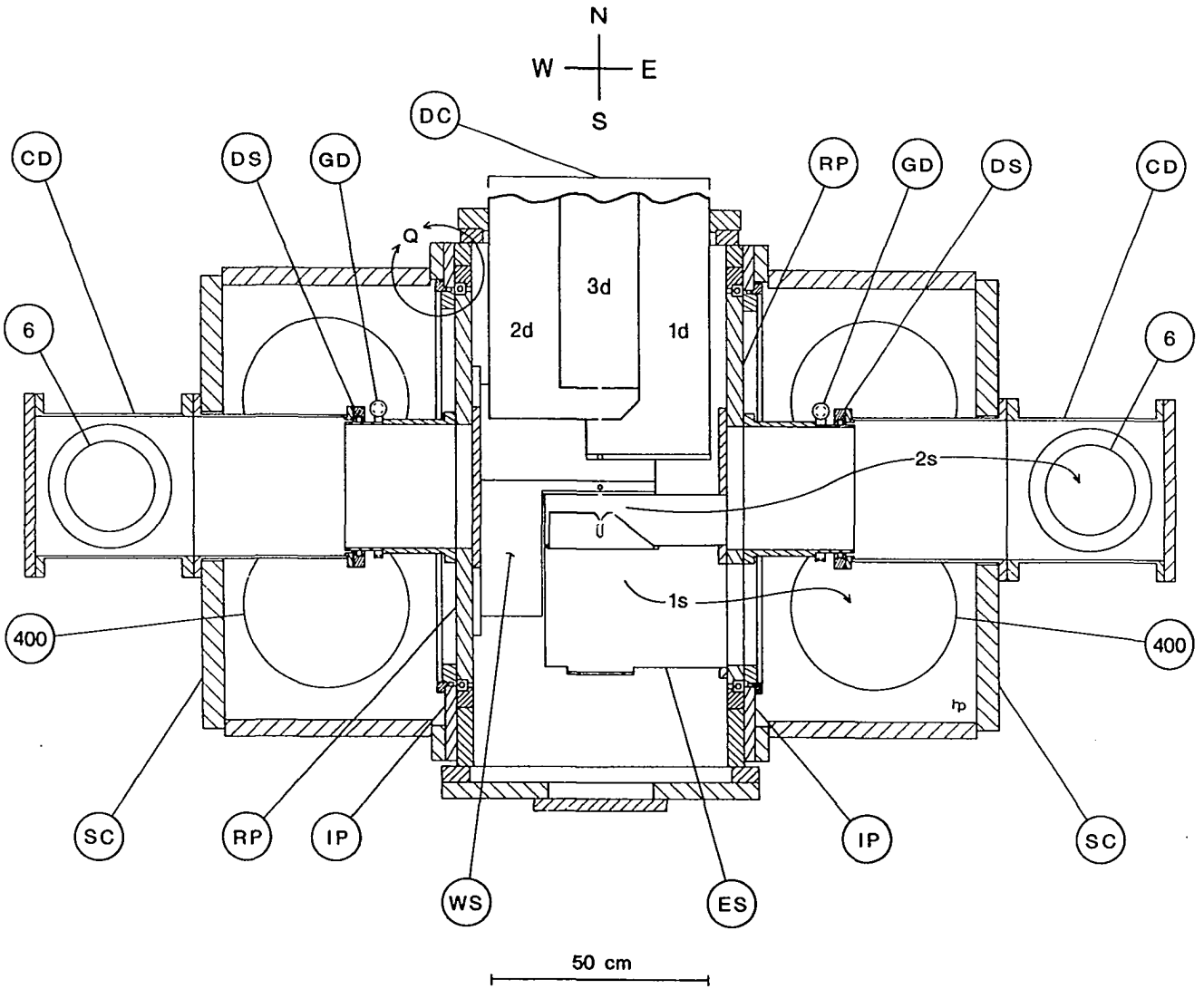

Horizontal cross sectional view of the rotating source apparatus

Figure 1b. Vertical cross sectional view of the rotating source apparatus (looking east to west). Indicated in the figure are:

DC - the detector chamber within which 1d, 2d, and 3d indicate the first, second, and third detector regions

SB - one of two 'strongbacks'

NP - the main chamber north plate

RP - (the west) rotating plate

RR - the 101.600 cm o.d. ring

AF - the main chamber aluminum flange

ES - the east beam source chamber

WS - the west beam source chamber

10 - a gate-valved 5300 l s^{-1} diffusion pump

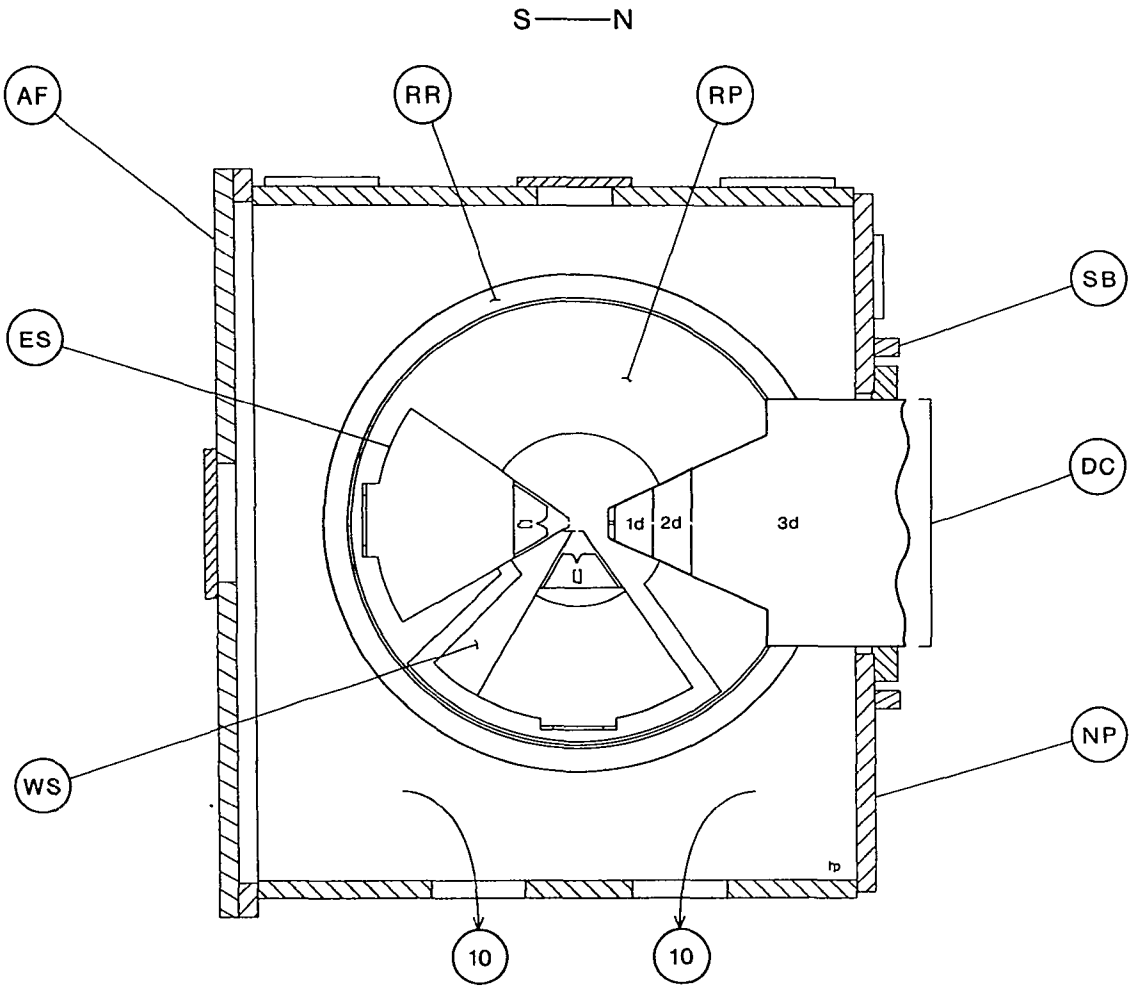

Vertical cross sectional view of the rotating source apparatus

'South'[1] end of the apparatus (RSM-MC011), by removal of the 153.0 cm high, 73.0 cm wide, 3.8 cm thick aluminum alloy 6061-T6 'door' (RSM-MC013). A vacuum seal is made by a 0.953 cm wall diameter, 127.3 cm inside diameter (i.d.), custom ground and spliced [4] Viton V747 O-ring held by a rectangular groove in the aluminum flange. Directly opposite the (south) entry is a 53.340 cm diameter bore through the 'North' wall of the chamber (RSM-MC009). This bore and the 66.0 cm diameter spotface perpendicular to the bore axis on the exterior of the north wall serve to locate the detector chamber. Since the position of the detector chamber is critical, two 3.81 cm wide by 5.08 cm high strongbacks are welded continuously along the entire 63.5 cm width of the north plate 34.3 cm above the 53.340 cm bores center to provide additional rigidity. Above the upper strongback are two 10.2 cm i.d. ports. The top plate of the main chamber (RSM-MC010) has an additional five 15.2 cm i.d. ports for various feedthroughs. Attached to the bottom plate (RSM-MC012) are two gate valved [5] "10 inch", 5300 l s^{-1} oil [6] diffusion pumps [7] backed by a single, 12.61 l s^{-1}, two stage [8] rotary vane pump. The ('East' and 'West') side walls (RSM-MC008) each have a 101.600 cm diameter through hole 'line-bored' such that the axes of the bores coincide within $2.5 \cdot 10^{-3}$ (total). The axis of the 53.340 cm diameter bore of the north wall is perpendicular to the axes of the two 101.600 cm diameters of the side walls within $5.1 \cdot 10^{-3}$ cm (total). Both sides

---

[1]The four major points of the compass combined with up and down proved extremely useful in (long-distance) discussions with chamber fabricators and so will be retained here.

have a flat about 7.0 cm wide machined along the outer edge of the plates exterior face which serves both sealing and locational purposes. These surfaces are flat within $1.5 \cdot 10^{-2}$ cm total and parallel within $1.5 \cdot 10^{-2}$ cm overall. To within these (extremely 'tight') tolerances, the main chamber has reflection symmetry in the vertical plane running north-south equidistant between both side walls. Therefore, most other pieces are mirror images of each other.

Bolted to each side is a 144.1 cm high, 119.4 cm wide, $\sim$2.5 cm thick 304 stainless steel plate referred to as the intermediate plate (RSM-BS001, RSM-BS002) [9]. The side of the intermediate plate, hereafter the I plate, against the machined surface of the main chamber is flat to $1.3 \cdot 10^{-2}$ cm total and bears a rectangular 109.2 cm by 134.0 cm O-ring groove. The seal i.d. is approximately 472 cm and made with a single splice from 0.95 cm wall diameter butyl cord stock using Eastman 910 adhesive. Because the machined flats do not extend across the entire surface of the east and west main chamber sides, the I plates are 'relieved' to approximately 0.6 cm depth inside the rectangular O-ring groove to prevent mechanical interference on assembly. The gas normally entrapped in the space between each I plate and the main chamber wall is evacuated via 0.9 cm i.d. copper tubing connected to the main chamber. The important purpose of the I plate(s) will be given following a description of the source chambers.

Bolted to the rear of each I plate, along the same bolt-lines that attach the I plate to the main chamber, is a 132.7 cm high, 107.9 cm long, 52.7 cm wide 6061-T6 aluminum alloy source chamber (RSM-BS006)

[10]. The source chamber is open on the 132.7 cm by 107.9 cm side and bolts to the back of the I plate by a 119.4 cm by 144.1 cm, 3.2 cm thick flange. A rectangular 104.8 cm by 129.5 cm O-ring groove in this flange accommodates another 0.95 cm wall butyl seal of about 452 cm i.d. fabricated as previously described for the I plate seals. This seal between the aluminum source chamber and the I plate is located almost directly above the I plate - main chamber seal. Thus, the huge force due to the atmospheric pressure, $\sim 1.5 \cdot 10^4$ kilograms, completes O-ring compression. Because the seals are near the edges of the main chamber, the total atmospheric force appears essentially as compression and, therefore, results in very little plate deflection, again, important for alignment integrity. The top, 3.8 cm thick plate of the aluminum source chamber (RSM-BS009) has two 10.2 cm, one 25.4 cm, and one 2.5 cm i.d. ports. Similarly, the south 3.8 cm thick wall (RSM-BS010) has a single 15.2 cm and 25.4 cm i.d. port. To avoid the possibility of interference with detector chamber items, the north, 3.8 cm thick wall is featureless. Attached directly to the south side of the (3.8 cm thick) bottom plate (RSM-BS008) is a "16 inch", 8000 l s^{-1} oil [11] diffusion pump [12] backed by a two stage, 17.3 l s^{-1} [13], rotary vane mechanical pump. Enough space has been reserved on the (north side of the) bottom plate to accommodate another diffusion pump of the same [12] or smaller size. The rear (5.1 cm thick!) plate (RSM-BS011) has two 15.2 cm, one 36.2, and one 33.65 cm i.d. ports. Limited rear access to these chambers after assembly is through the 36.2 cm i.d. port. A 33.0 cm outside diameter (o.d.) 304 stainless steel 0.32 cm wall tube

(RSM-BS022) is inserted into each aluminum source chamber through the 33.65 cm port. Also, mounted on this port at the rear of the 33.0 cm o.d. tube is a 33.0 cm o.d. by 27.9 cm o.d. 304 stainless steel cross (RSM-BS015) [14]. Hanging vertically from the cross 27.9 cm arm is a "6 inch" 2500 l s^{-1}, oil [11] diffusion pump [15] backed by a two stage, 12.6 l s^{-1} [8], rotary vane mechanical pump. Mounted on the bottom plate corners of both aluminum source chambers are four [16] ball bushings on two 137.2 cm long, 3.175 cm o.d. case-hardened steel rods. The rods are perpendicular to the main chamber sides within $5.1 \cdot 10^{-3}$ cm in 30.5 cm and parallel within $2.5 \cdot 10^{-3}$ cm total. This bushing system allows assembly and disassembly of the aluminum source chamber and I plate as well as aids the removal and installation of the I plate. The very low friction of the bushings permit the massive ($\sim 8 \cdot 10^{2}$ kgs) source chamber and I plate to be easily moved. General manipulation and assembly of all the chambers, stands, pumps, etc. was assisted by a translating overhead i-beam system with a movable one-ton electric hoist. These two systems are so efficient and convenient, a single (competent) researcher can perform all the required operations.

Now that the I plate is understood to be an independent piece sandwiched between the main and source chamber, its singularly important purpose can be described in detail. Off the center of the I plate to the north is a raised ($\sim$0.28 cm high, 93.980 cm diameter) circular step. A 304 stainless steel ring (RSM-MC016) precisely 'keys' to this step on its i.d. The concentric outer diameter of the ring is precisely fit, with less than $2.5 \cdot 10^{-3}$ cm clearance, to the 101.600 cm bore of the

main chamber. The rings outer diameter is tapered 1/2 degree to aid installation, however, because the ring-I plate assembly is fairly massive and the fit very 'tight', the entire unit is made self-aligning on assembly by a spring loaded carriage. (Attempting to force the pieces together or apart would destroy the locational nature of the fit at the very least.) Also, precisely fit to the inner (93.980 cm) diameter of the ring is an X contact [17] bearing. Fitted to the 88.900 cm bore of the bearing facing the main chamber is the rotating plate (RSM-BS020, RSM-BS021) and on the side toward the aluminum source chamber is the rotating retaining ring (RSM-BS026). The stainless steel rotating ring has two purposes; first to secure the rotating plate to the bearing and second to provide a sealing surface. The other sealing surface is a polished 90.115 cm bore in the I plate concentric with the raised circular step and, therefore, also the bearing. The seal is made by a graphite embedded Teflon [18] Tec-Seal. This design permits all heavy steel items to be assembled prior to installation of the delicate Tec-Seal. Movement of the Tec-Ring from the groove is prevented by an aluminum retaining ring (RSM-BS037) bolted to the source chamber side of the I plate. The situation is diagrammed in Fig. 2. Bolted to the center of the rotating ring, extending into the aluminum source chamber, is a 30.2 cm o.d., 1.3 cm wall tube 'keyed' to be concentric with the 88.900 cm diameter of the rotating plate which contacts the bearing. This tube has two functions; first to drive the rotating plate and second, as will be discussed later, to provide pumping. Pressed onto the tubes o.d., about 19 cm from the rear face of the rotating plate, is a

Figure 2. Detail of the rotating plate, bearing, and seal assembly. Indicated in the figure are:

1 - (north wall of the) main chamber

2 - intermediate plate

3 - aluminum source chamber

4 - 'relieved' section of intermediate plate

5 - Tec-Seal aluminum retaining ring

6 - Tec-Seal

7 - rotating retaining ring

8 - rotating plate

9 - beam source chamber (this position is inaccessible after detector chamber assembly)

10 - bearing

11 - 101.600 cm o.d. ring

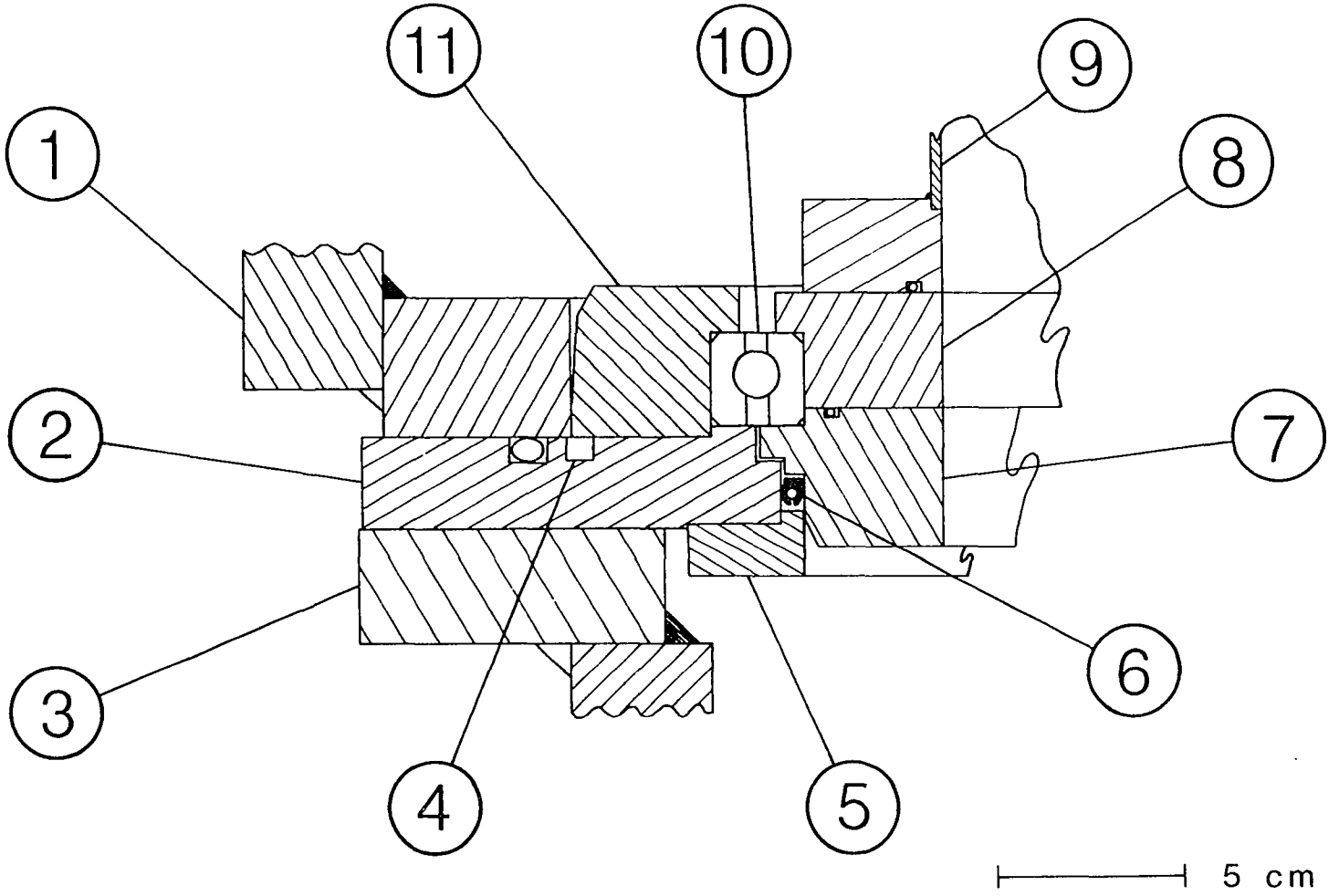

Detail of the rotating plate, bearing, and seal assembly

phosphor bronze, 100 tooth, 8 diametral pitch, worm gear. Engaging the worm gear is a mating hardened steel worm [19] mounted on a stainless steel shaft. This drive shaft is coupled through the 2.5 cm port of the top plate of the aluminum source chamber to a microprocessor controlled (refer to Appendix B) stepping motor [20]. Thus, both (east and west) rotating plates are independently rotatable. Beyond the worm gear, the 30.2 cm o.d. tube is connected to the 33.0 cm o.d. tube inserted through the 33.2 cm i.d. port of the aluminum source chamber. The connection is made vacuum tight by a movable O-ring face seal attached to the 33.0 cm o.d. tube and another O-ring shaft seal on the o.d. of the 30.2 cm tube. This arrangement isolates the interior of both tubes from the interior of the aluminum source chamber, allows the rotation of the inner 30.2 cm tube, and is designed to be self-aligning on assembly and during operation. The face view of the rotating plate (Fig. 3) shows a cutout beginning at a radius of 17.1 cm and ending at 40.6 cm. The angular span of this 'window' is 80 degrees total. Along the line 35 degrees from the edge of the 'window' and on either side of the 29.2 cm bore are 1.27 cm diameter 'tool' steel dowel pins. The beam source chamber is located by these dowel pins on this surface (facing into the main chamber) of each rotating plate.

Since the shapes of the beam source chambers are irregular, they are difficult to describe. Reproductions of front and rear photographs, Figs. 4a and 4b, respectively, and the dimensional schematic top view of Fig. 4c should aid visualization and, thereby, an understanding of the function. Essentially, the beam source chamber is a 65 degree wedge

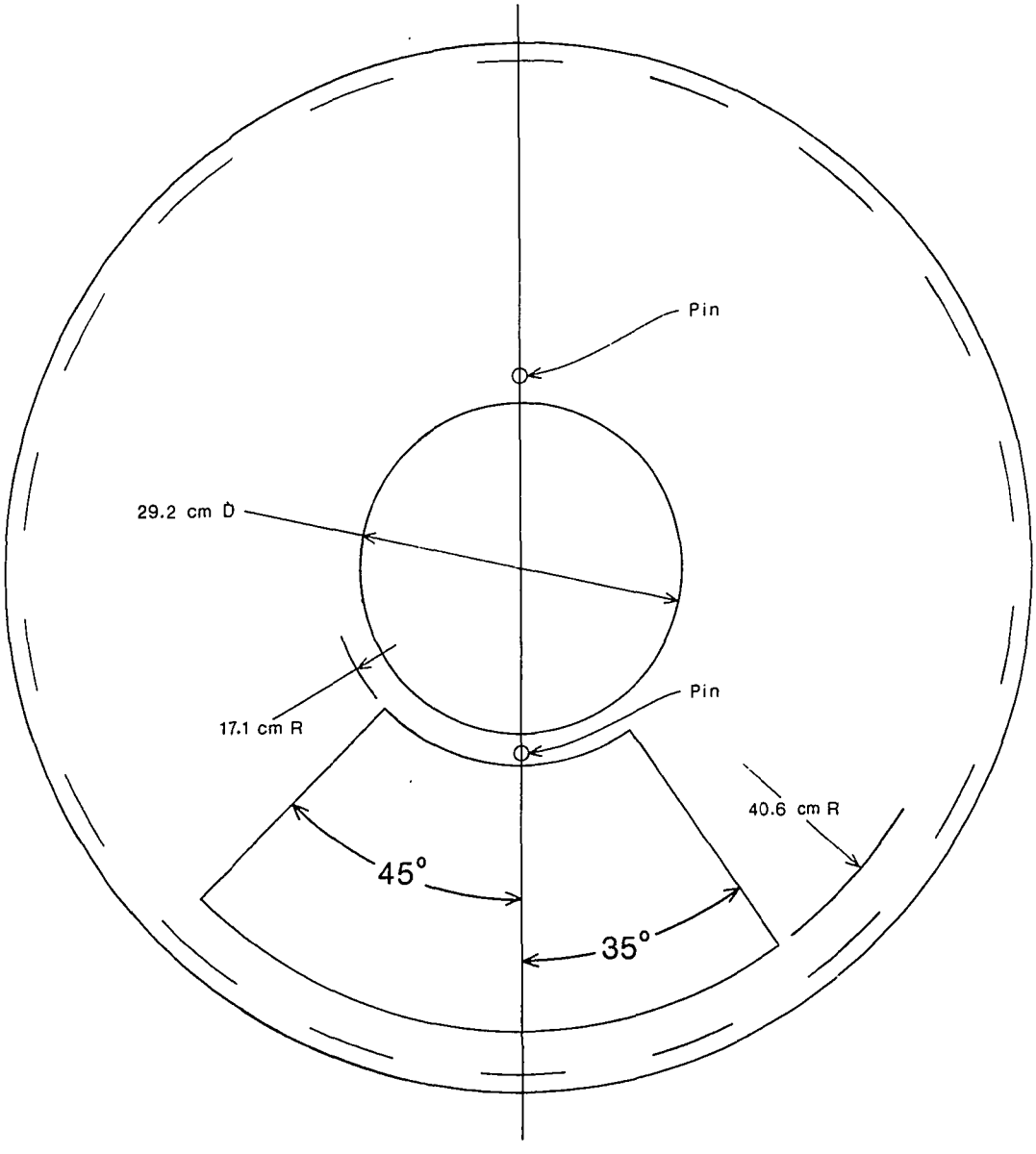

Figure 3. Front face of the rotating plate (dashed circle indicates the inside diameter of the bearing)

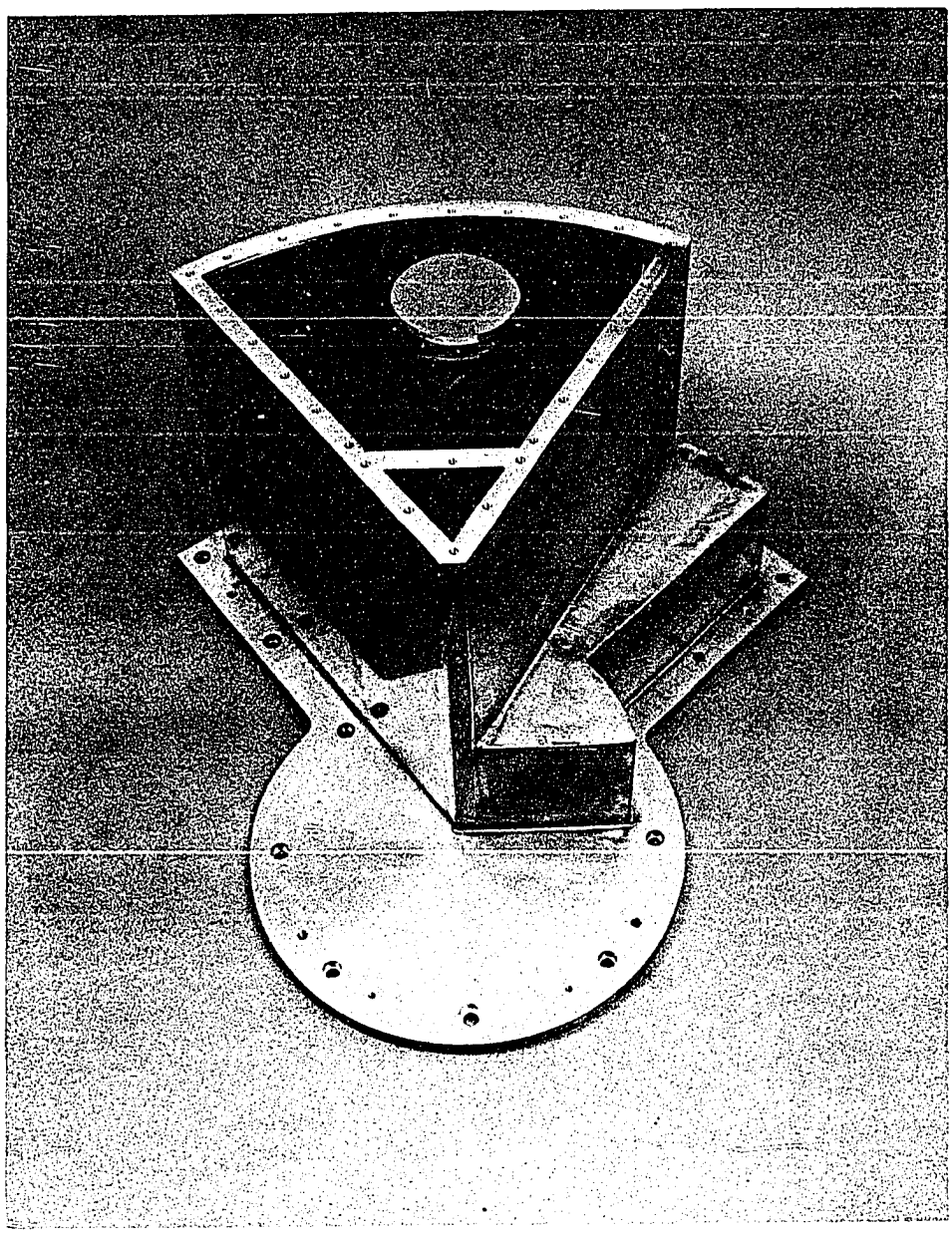

Figure 4a. Front view of beam source chamber

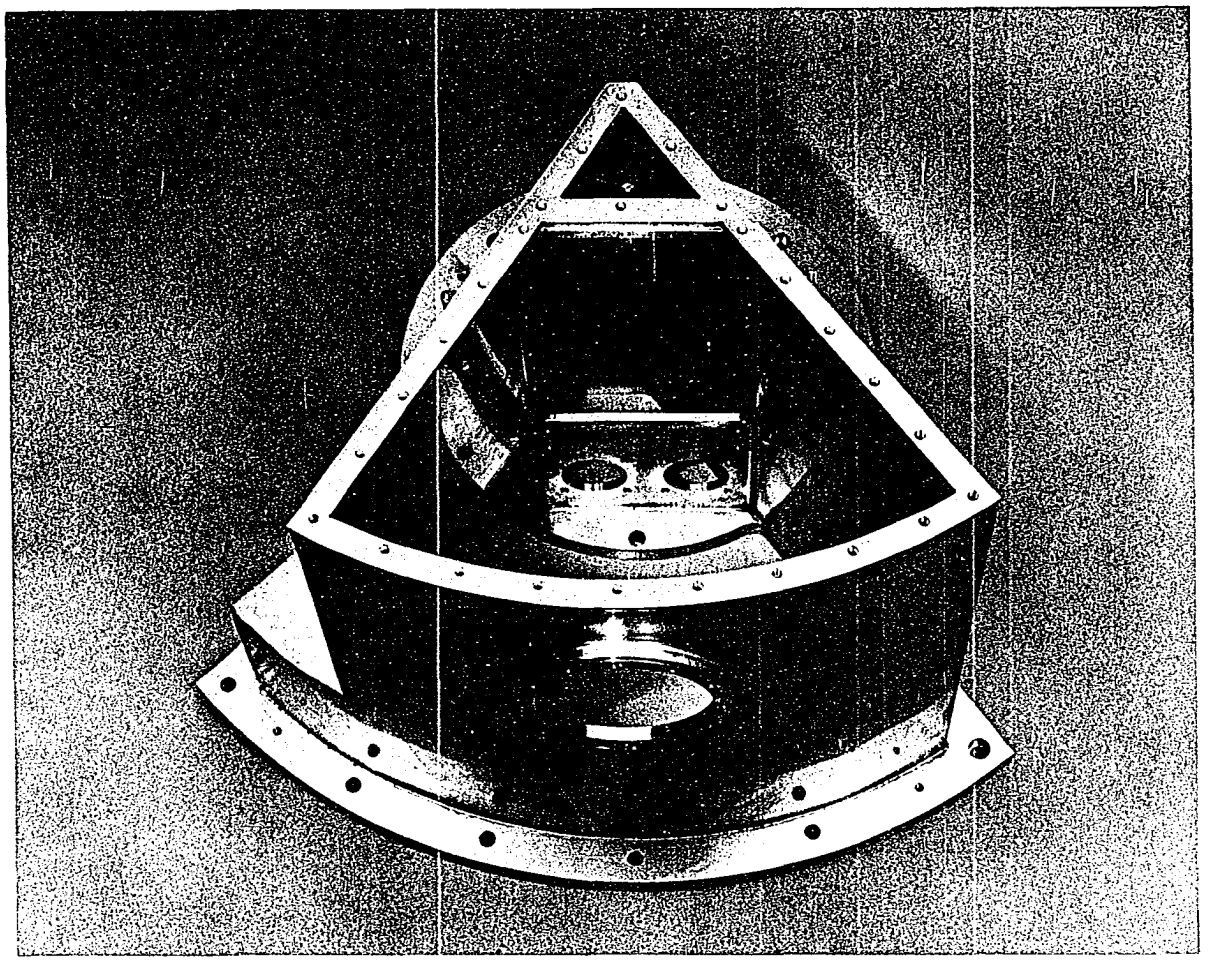

Figure 4b. Rear view of beam source chamber (notice the nosepiece and rotating plate 'windows')

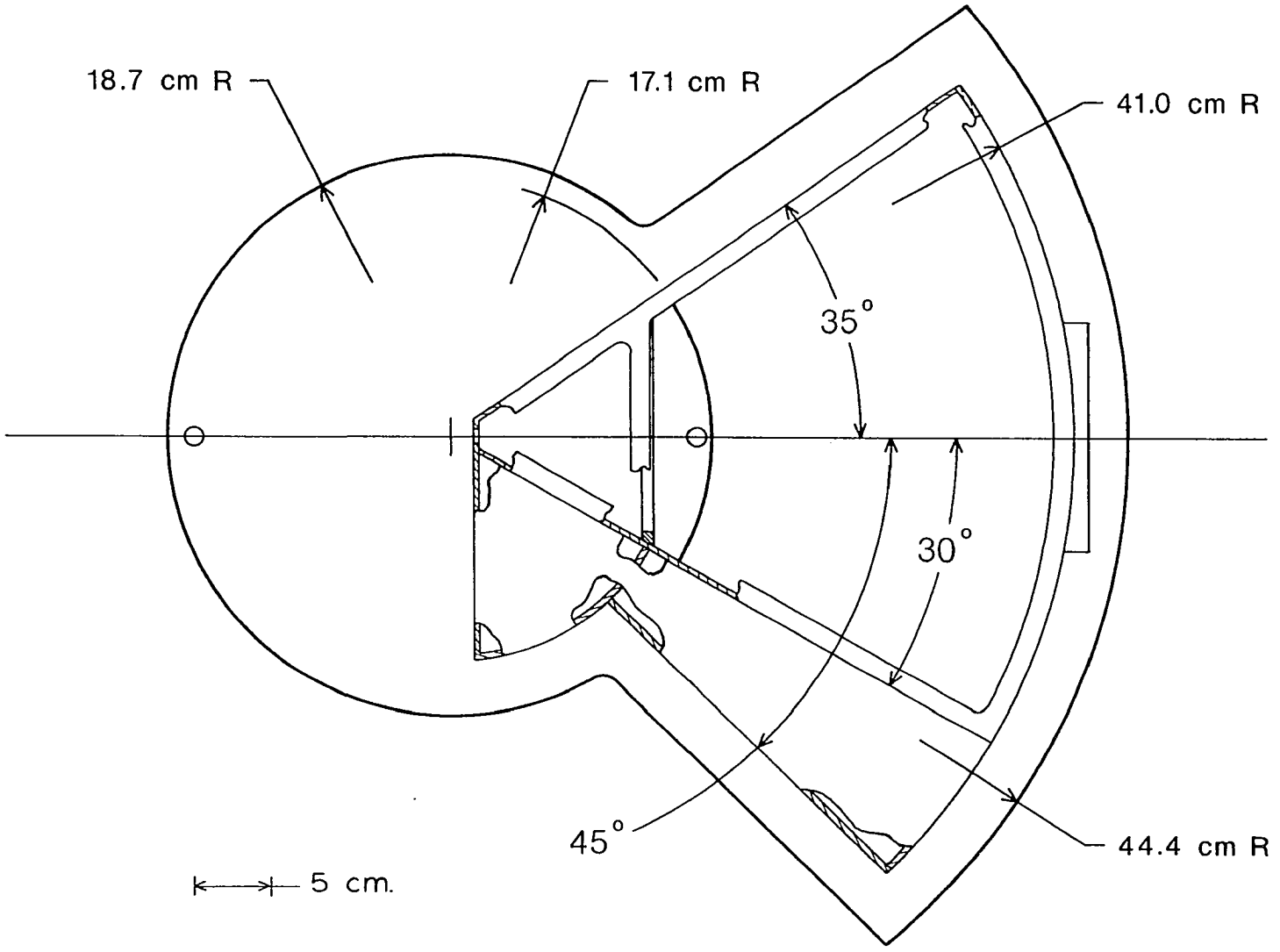

Figure 4c. Top view of beam source chamber

fabricated from 0.32 cm thick 304 stainless steel sheet. One side of the wedge is extended about 26 cm down from the top. The interior is partitioned, top to bottom, into two regions by a 0.63 cm thick wall which meets the 30 and 35 degree side walls (refer to Figs. 4). At 26 cm below the top, a semi-circular wall extends from the 30 degree side of the 0.63 cm wall to the extended (45 degree) wedge wall and beyond. Thus, the beam source chamber consists of two regions. One large trapezoidal region which, when the beam source chamber is installed, is directly above the 'window' of the rotating plate and another smaller volume, shaped like a trapezoid on top and a quarter of a cylinder on the bottom, open to the 29.2 cm diameter of the rotating plate. Bolted into a 14.6 cm wide by 24.1 cm window in the 0.63 cm partition is one of several possible source nosepieces (RSM-BS036, RSM-BS043, RSM-BS044). This is shown in the partial cross section of the front of the beam source chamber, Fig. 4d. These various interchangeable nosepieces precisely position the (nozzle) source (e.g., RSM-BS049) and skimmer [21] system at several discrete distances from the axis of rotation. Continuous adjustment of the (nozzle) source-skimmer distance to optimize beam character, while under vacuum, is made by a drive connected through the rear port of the beam source chamber to a port in the main chamber door when the beam source is alligned with the detector axis. Now one sees the first stage of differential pumping (i.e., between the source and the skimmer) takes place through the large 80 degree 'window' of the rotating plate. The distance from the (crossed) beam plane to the bottom of the rotating plate 'window' is comparatively short and the area

Figure 4d. Cross section of beam source chamber near the axis of rotation. Indicated in the figure are:

1 - beam source chamber 'lid'

2 - lid seal

3 - beam defining aperture

4 - source nosepiece

5 - source alignment fixture

6 - schematic room temperature source

7 - skimmer

8 - first stage of source differential pumping

9 - second stage of source differential pumping

Note: the collision region is located at the intersection of the molecular beam axis, indicated by the horizontal line, and the axis of source rotation indicated by the vertical line

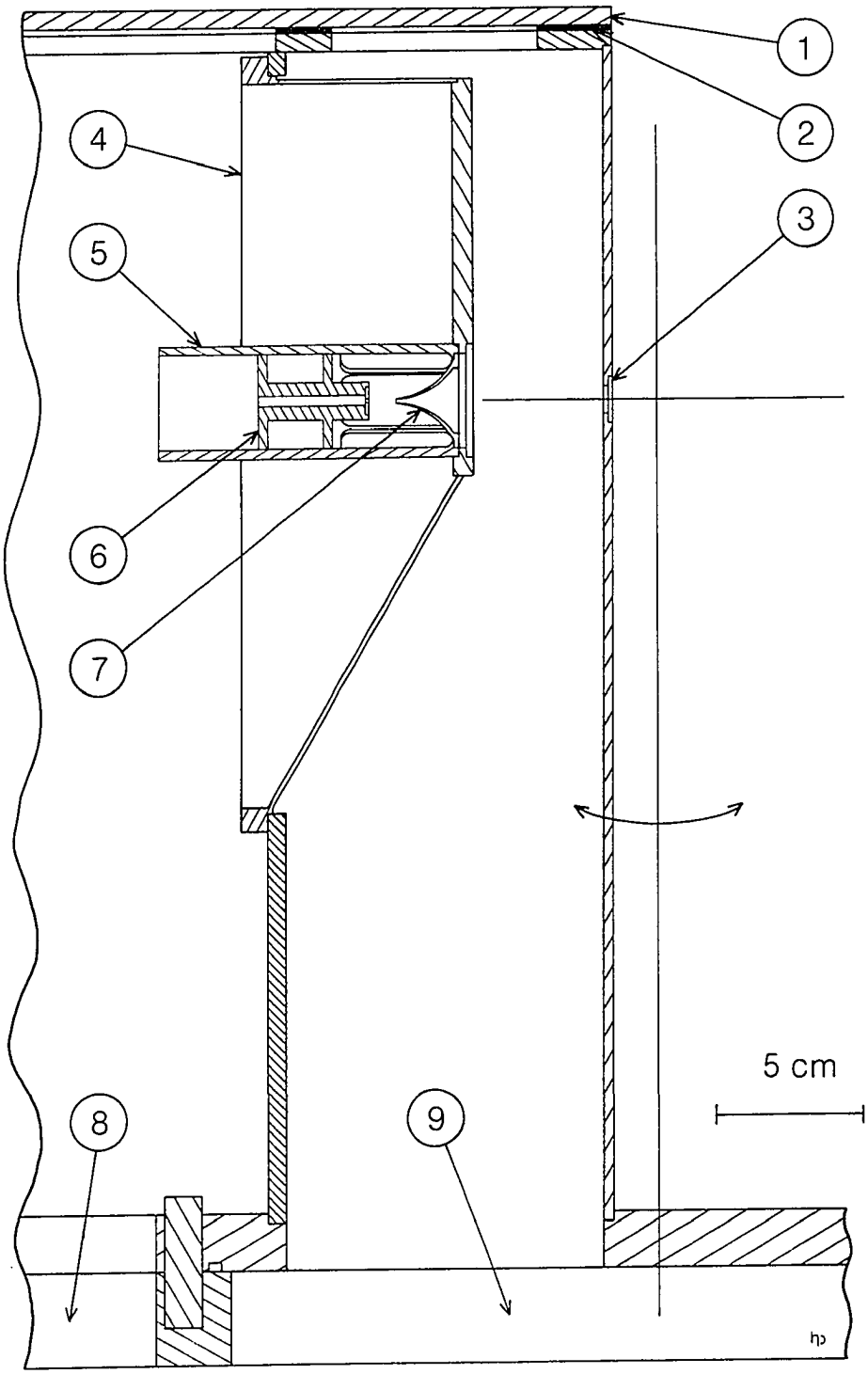

Figure 4d. Cross section of beam source chamber near the axis of rotation

of the 'window' large, so the (effective) pumping speed of the aluminum source chambers 8000 l s^{-1} diffusion pump remains high. In terms of distance, the differential pumping of the second stage (i.e., after the skimmer and before the second, beam defining aperture) appears less favorable (refer to Fig. 1a). Gas exiting the 29.2 cm i.d. bore must travel through the 30.2 cm o.d. rotating tube and stationary 33.0 cm o.d. tube before reaching the 33.0 cm by 27.9 cm cross and the 2500 l s^{-1} diffusion pump. Although the ratio of length-to-radius for the connecting tubes is, unfortunately, high ($L/r \sim 5$, refer to Appendix A), sufficient conductance is maintained by the large value for r.

Notice that although each beam source rotates freely and independently with two stages of differential pumping, there are no moving pumps. The rotating beam source chambers are mounted such that the 30 degree side of the upper wedges can touch. This means the beam crossing angle, Γ of Fig. 1, can be as small as 60 degrees. After choosing a particular beam crossing angle, the beam source chambers remain fixed at that relative angle as they are rotated together about the detector. Contact between the 35 degree side of the beam source chamber with the detector chamber limits the angular range (refer to Fig. 1b). For example, if the beam crossing angle is 90 degrees, a total angular range of 150 degrees is available. If the intersection angle is chosen to be 60 degrees, the permitted angular scan becomes 180 degrees. In fact, any crossing angle between 60 degrees and 240 degrees is mechanically possible.

The photograph of Fig. 5 shows the main and aluminum source chambers, forelines and pumps, etc. as viewed from the 'southwest' corner. Figure 6 shows the apparatus with the west aluminum source chamber retracted and the main chamber door removed. The rotating plate drive and beam source chambers (inside the main chamber) are clearly visible.

A final note about the vacuum system is in order. Special design and operation of the forelines avoids excessive pressure differences in the beam source chambers during pump down. All diffusion pumps are protected against the failure of cooling water, foreline vacuum, and for pump overheating via individual, interlocked diffusion pump controllers (RSM-E001, RSM-E002).

The detector chamber[1]

The horizontal and vertical cross sectional views of the detector chamber shown in Figs. 7a and 7b, respectively, will be helpful in understanding the description that follows.

Essentially, the detector chamber (RSM-D006) [22] is an internally partitioned 50.8 cm o.d., 0.32 cm wall tube with a 50 degree beveled front. The 0.48 cm thick wall of the bevel begins at a 1.3 cm thick front faceplate (RSM-D007) which is, at the closest point, 6.35 cm from the beam source axis of rotation. The bevel continues back 31.8 cm before being joined to the tube by two 0.48 cm thick semicircular plates. At a distance of 53.3 cm from the detector faceplate is a

---

[1]Unless specified otherwise, all materials are 304 or 304L stainless steel.

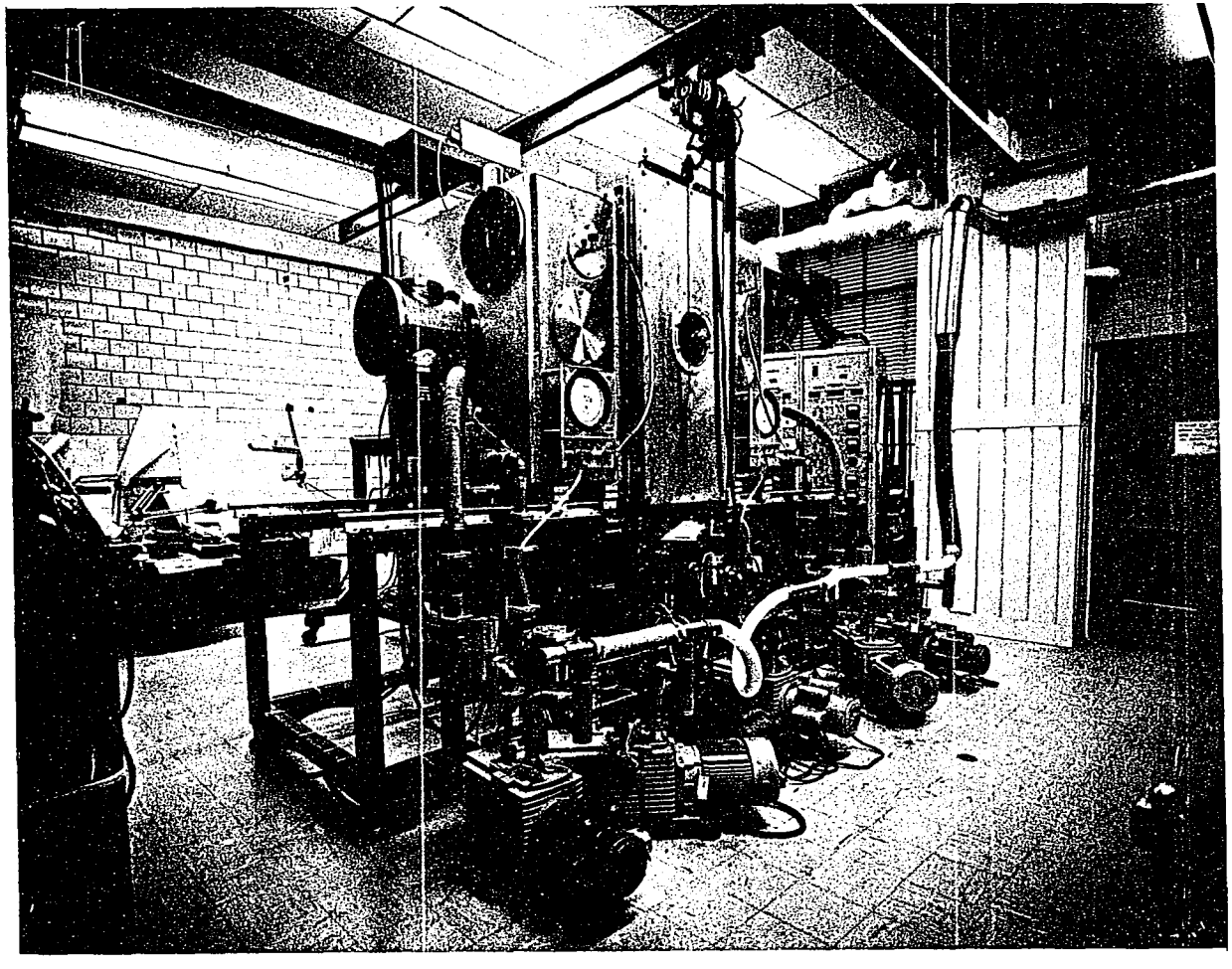

Figure 5. View of main and source chambers (from southwest corner)

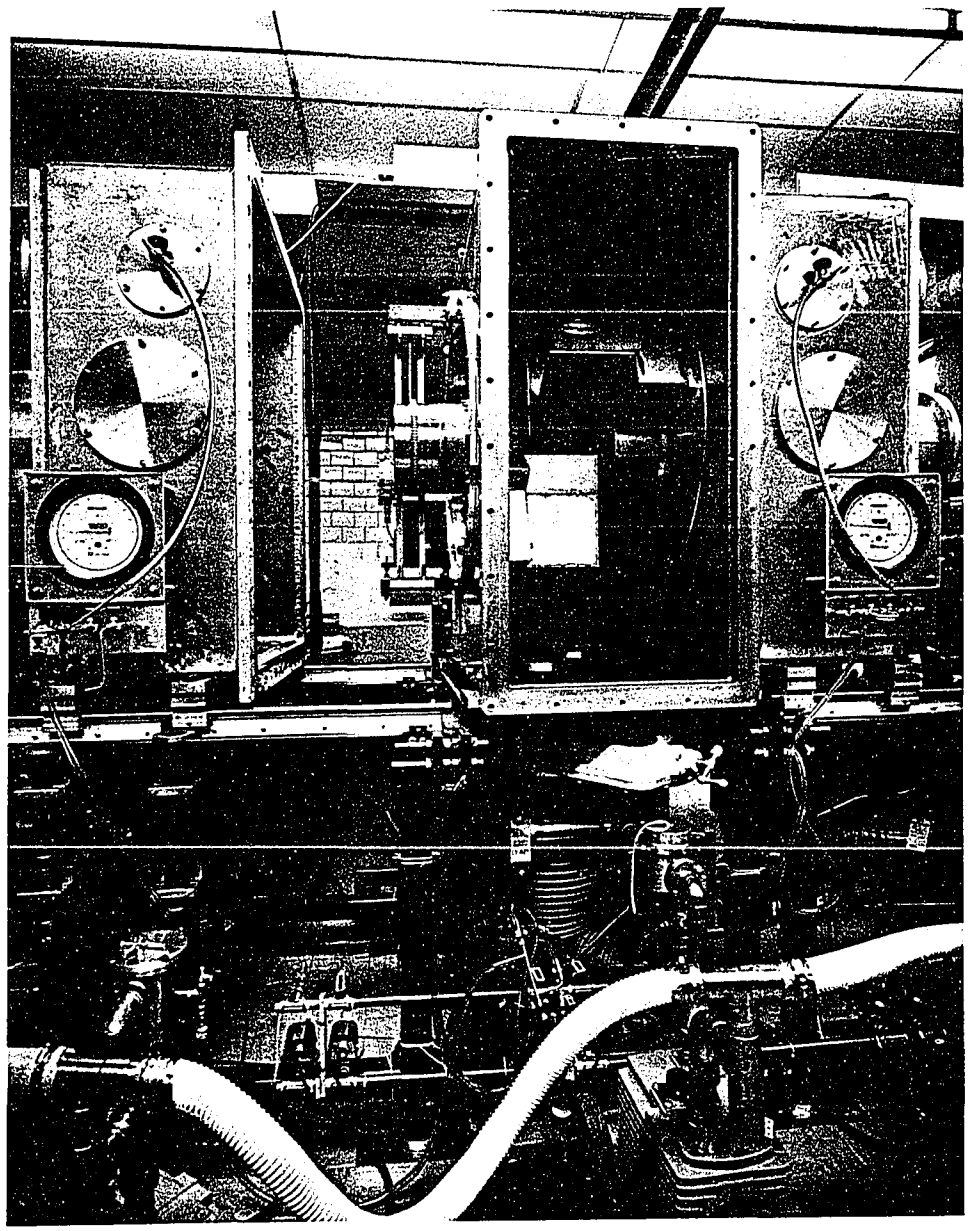

Figure 6. The RSA with the west source chamber retracted and main chamber flange removed

Figure 7a. Horizontal cross sectional view of the detector chamber. Indicated in the figure are:

1st, 2nd, 3rd - the first, second, and third detector regions, respectively

E, W, N - the east, west, and north main chamber plates, respectively

D - the detector

R - (one of the two) rails

1 - faceplate

2 - slide valve

3 - aperture fixture

4 - innermost region flange

5 - liquid nitrogen dewar

6 - one of four vertical 'strongbacks'

7 - detector chamber (64.8 cm o.d.) flange

8 - reinforcing band

9 - 220 l s^{-1} ion pump

10 - electropneumatic gate valve followed by 330 l s^{-1}

11 - wire seal flanges

13 - 220 l s^{-1} ion pump port

14 - rotary motion feedthrough

15 - "10 inch" Conflat flange

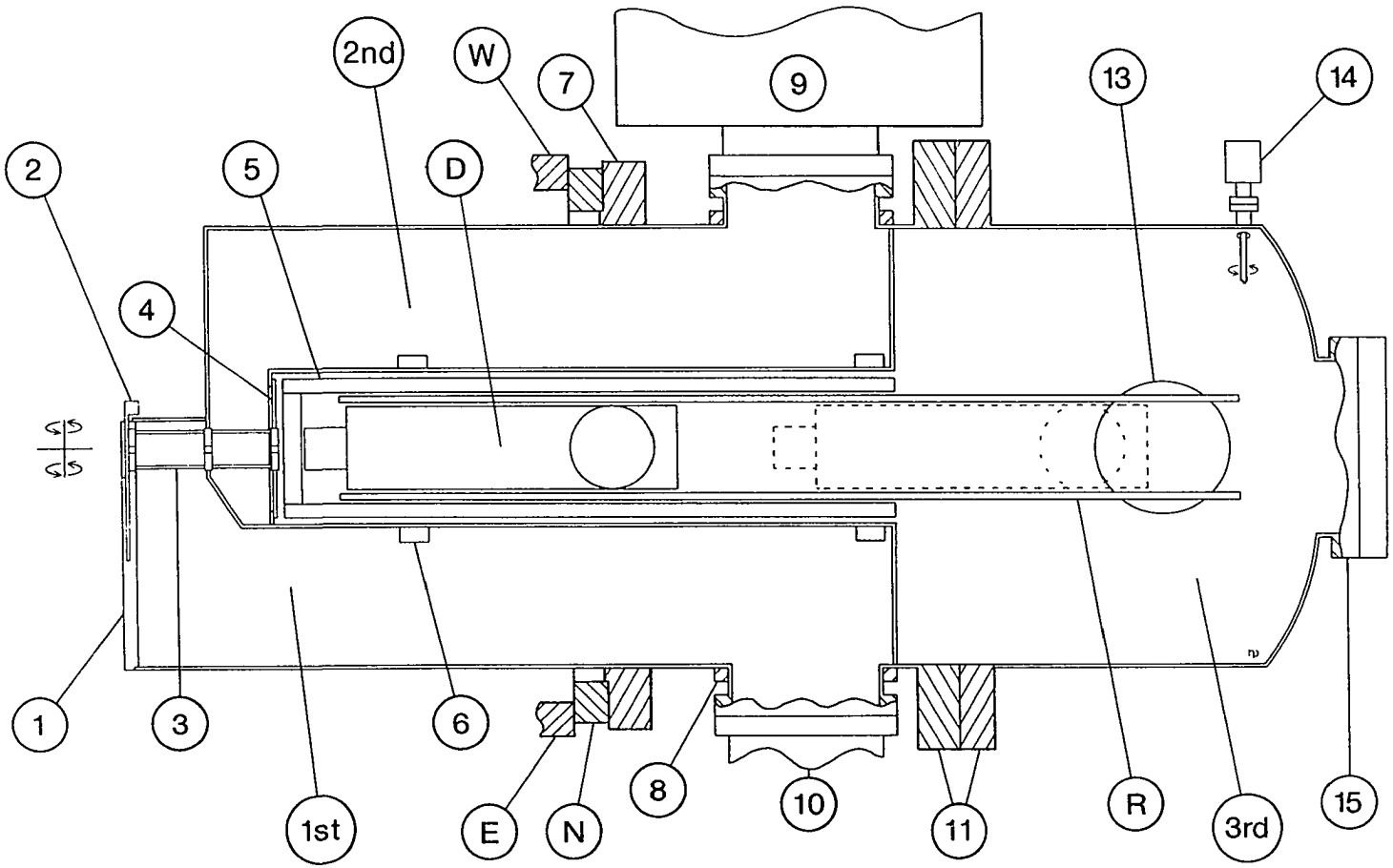

Horizontal cross sectional view of the detector chamber

Figure 7b. Vertical cross sectional view of the detector chamber. Indicated in the figure are:

1st, 2nd, 3rd - the first, second, and third detector regions, respectively

N - the main chamber north plate

D - the detector

R - 'rail'

1 - faceplate

2 - aperture fixture

3 - innermost region flange

4 - liquid nitrogen dewar

5 - (one of two) main chamber strongbacks

6 - detector chamber (64.8 cm o.d.) flange

7 - reinforcing band

8 - wire seal flanges

9 - 220 l s^{-1} ion pump

10 - "10 inch" Conflat flange

11 - liquid helium cryopump

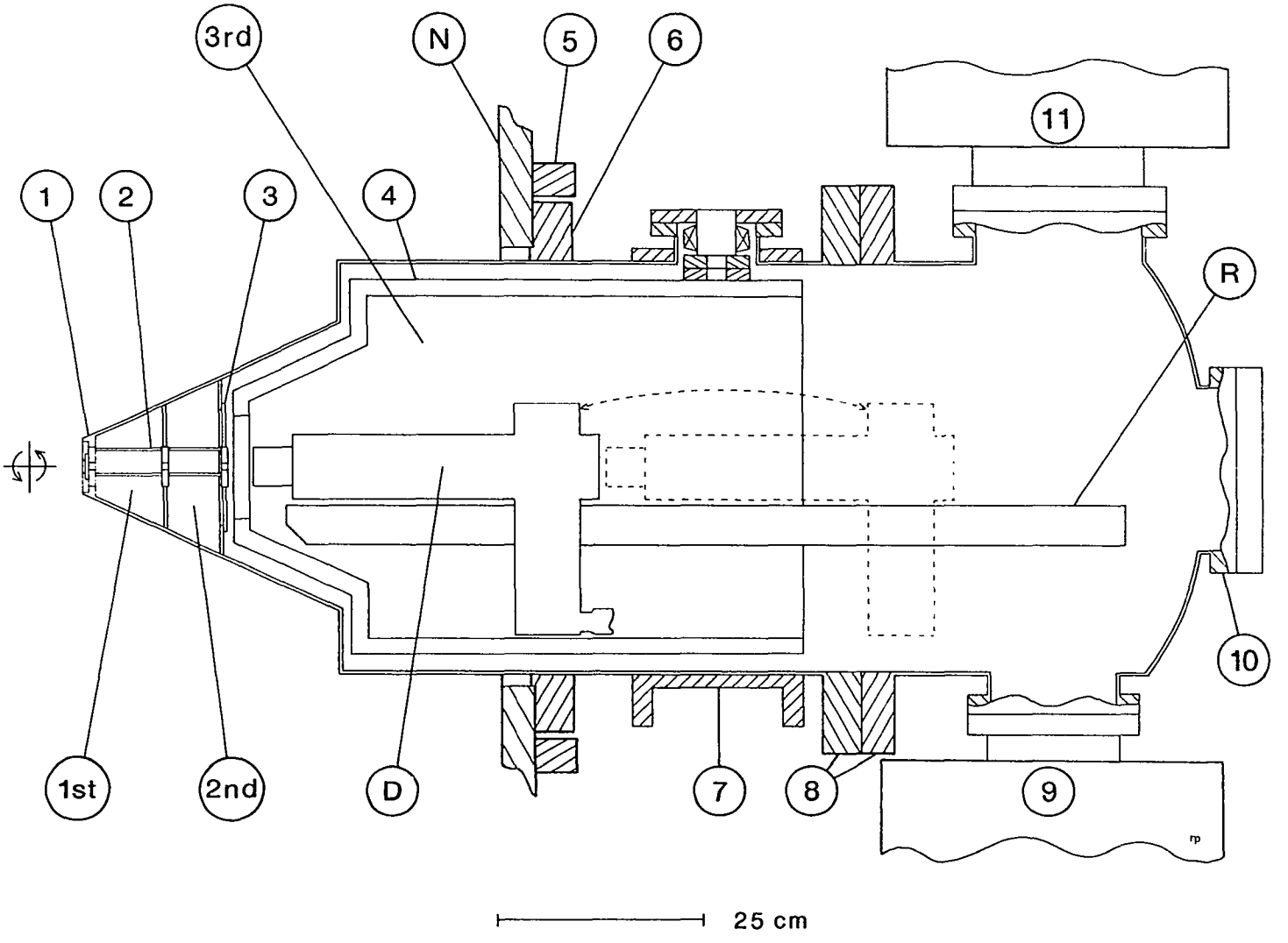

Vertical cross section of the detector

64.8 cm o.d., 4.5 cm thick flange welded to the 50.8 cm tube o.d. A precise circular 'key' machined on this flange locates the detector chamber in the 53.340 cm bore of main chamber north wall. A 0.70 cm wall diameter Viton O-ring in a groove on the detector chamber flange seals against the 66.0 cm spotface. Back 11.4 cm from the flange face, away from the main chamber and outside the vacuum, is a 20.3 cm wide, 1.3 cm thick band welded intermittently about the o.d. of the 50.8 cm tube. This band greatly enhances rigidity and the detector stand, which supports the detector chamber, is attached at the bottom of the band. A "24 inch" female wire seal flange [22] is welded to the 50.8 cm o.d. tube 2.4 cm behind the band. The mating male wire seal flange [22] is welded onto a 31.1 cm long, 50.8 cm o.d. tube of 0.32 cm thickness which forms a separate piece referred to as the detector chamber cap (RSM-D016) [22]. A set of [23] ball bushings on 1.588 cm o.d. case-hardened steel rods mounted to the detector stand, in an arrangement like that of the aluminum source chambers, allows for the assembly of the detector cap with the rest of the detector chamber.

The interior of the 50.8 cm o.d. tube forward of the female wire seal flange is vertically partitioned into three regions (refer to Figs. 7). At distances 8.9 cm and 16.5 cm from the faceplate, and parallel to it, are two 0.48 cm thick vertical walls (RSM-D008). The upper and lower edges of these plates are welded to the two bevel faces. The sides of these plates are joined to two parallel vertical (0.48 cm thick) walls spaced 17.8 cm apart and parallel to (and symmetric about) the tube axis. These two partitions, which run lengthwise in the tube

each end at a perpendicular, half-moon shaped, 0.48 cm thick plate (RSM-D009, RSM-D011). This arrangement of vertical plates divides the detector tube into three separate regions. The first region extends from behind the faceplate and before the parallel wall 8.9 cm behind it, along the east side of the tube in the semicircular channel (16.5 cm at the widest point) to the rear 'half-moon' wall. In the same manner, the second region extends along the other (i.e., west) side of the wall 8.9 cm from the faceplate and in front of the wall 16.5 cm back. The third or innermost region begins 16.5 cm behind the detector face and extends through the 17.8 cm wide central channel into the interior of the detector cap.

Three short ($\sim$2.2 cm), symmetrically oriented 15.2 cm o.d., 0.32 cm wall tubes with "8 inch" o.d. Conflat flanges connect through the 1.3 cm thick band to the first region (RSM-D012). Various feedthroughs are accommodated by the two tubes oriented 45 degrees above and below the horizontal tube. Attached to the "8 inch" o.d. Conflat flange of the horizontal tube is a specially modified (RSM-D030) [24] electropneumatic swing gate valve. Mounted to the rear of this gate valve is a 330 l s^{-1} [25] turbomolecular pump which provides pumping for the first region. A two stage, 3.8 l s^{-1} [26], rotary vane mechanical pump backs the turbomolecular pump via a liquid nitrogen and sieve trapped foreline. A protection circuit (RSM-E004) closes the swing valve and an electromagnetic valve [27] in the foreline upon loss of coolant, power, foreline pressure or turbomolecular pump rotation. In this manner, the turbomolecular pump is isolated from the first region of the detector

chamber and the foreline in the event of an accident, thereby, insuring cleanliness of the detector chamber.

Another horizontal tube and inclined tube of the same description connect through the west side of the band (RSM-D010) into the second region. Again, various feedthroughs enter the "8 inch" o.d. Conflat flange of the inclined tube while the horizontal tube serves for pumping purposes. In this case, attached to the horizontal tube is a 220 l s^{-1} [28] ion pump.

Pumping of the innermost region takes place through the detector cap. Another 220 l s^{-1} [28] ion pump is connected vertically, via an "8 inch" o.d. Conflat flange on a 0.32 cm wall, 15.2 cm o.d. tube, to the bottom of the detector cap. Mounted vertically on the top of the detector cap, via a "10 inch" o.d. Conflat flange on a 0.32 cm wall, 20.3 cm o.d. tube, is a custom fabricated [29] helium cryopump. In the rear view of the detector chamber of the photograph of Fig 8, the detector cap and detector chamber pumping systems are readily visible.

Forward of the wire seal flange is the liquid nitrogen dewar (RSM-D014) [22] which is shaped to fit just inside the contours of the innermost region. Essentially, the dewar is a box within a box with liquid nitrogen filling the space between the box walls (refer to Figs. 7a and 7b). A 'reversed' Conflat flange (RSM-D015) on the top of the dewar and its mate, which is welded to a flexible bellows [30], connect the dewar to the liquid nitrogen source through a 0.32 cm wall, 10.2 cm o.d. tube with a "6 inch" o.d. Conflat flange welded into the top of the innermost region through the band. The liquid nitrogen dewar surrounds the translating detector.

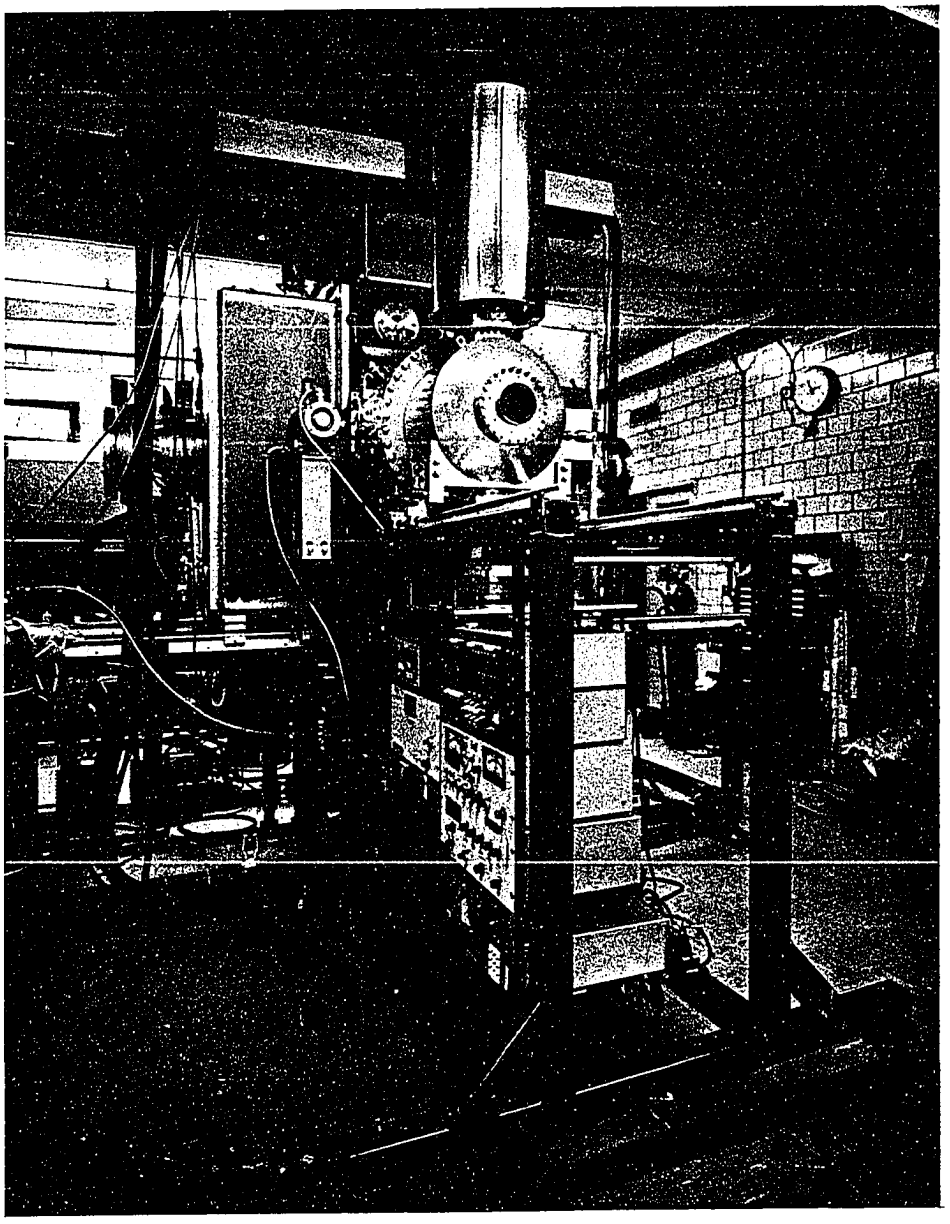

Figure 8. View of the north side of the RSA

The entire detector is carried on four 440C stainless steel wheels which ride on two 0.64 cm thick, 101.6 cm long 'rails'. A 0.635 cm o.d. threaded rod (at 7.87 threads per cm) connected via a right angle drive to a ultra-high vacuum rotary feedthrough [31] mounted on a "mini" (3.38 o.d.) Conflat flange in the detector chamber cap provides translation. (The actual situation is slightly more complex in that special materials and methods are required.) The total movement possible is about 60 cm.

The detector itself (refer to Fig. 9) consists of three parts; the ionizer, quadrupole mass filter, and the Daly [32] scintillation ion counter. The (present) ionizer design was generally provided by Richard J. Buss of Yuan T. Lees' research group at the Lawrence Berkeley Laboratory, Berkeley, CA. All the ion lenses were plated with gold [33] to a thickness of $1.3 \cdot 10^{-3}$ cm. The ionizer filament is a 2% thoriated tungsten, $1.78 \cdot 10^{-2}$ cm diameter wire [34]. Protracted attempts to obtain the cylindrical grid or 'cage' required for construction of the ionizer from a commercial source proved futile. Modifying (RSM-D037, RSM-D038) a mandrel design graciously provided by Randel K. Sparks of the California Institute of Technology in Pasadena, CA allowed a 2.9 cm long, 1.6 cm o.d. cage to be fabricated from $3.81 \cdot 10^{-2}$ cm diameter platinum wire. Spot welding fastened the cage to the appropriate lens. The ionizer is assembled on four 0.157 cm diameter alumina rods mounted to the faceplate (RSM-D035) of the quadrupole 'can' (RSM-D019). A 0.64 cm hole in this plate allows the ions to be injected into the quadrupole mass filter. Located by surfaces inside the quadrupole can are two

Figure 9. Vertical cross section of the detector. Indicated in the figure are:

I. - the ionizer

1 - the filament

2 - the platinum cage

Q.M.F. - the quadrupole mass filter

3 - 'can' faceplate

4 - Macor spacer

5 - quadrupole 'can'

6 - quadrupole rods (2 of 4)

7 - can rearplate

8 - exit lenses

D.S.C. - Daly scintillation counter

9 - 7.6 cm o.d. cross

10 - -30 kV feedthrough

11 - ion target

12 - aluminum coated scintillator

13 - mu-metal shield

14 - glass-to-stainless seal

15 - photomultiplier tube

16 - flexible bellows

17 - dynode 'can'

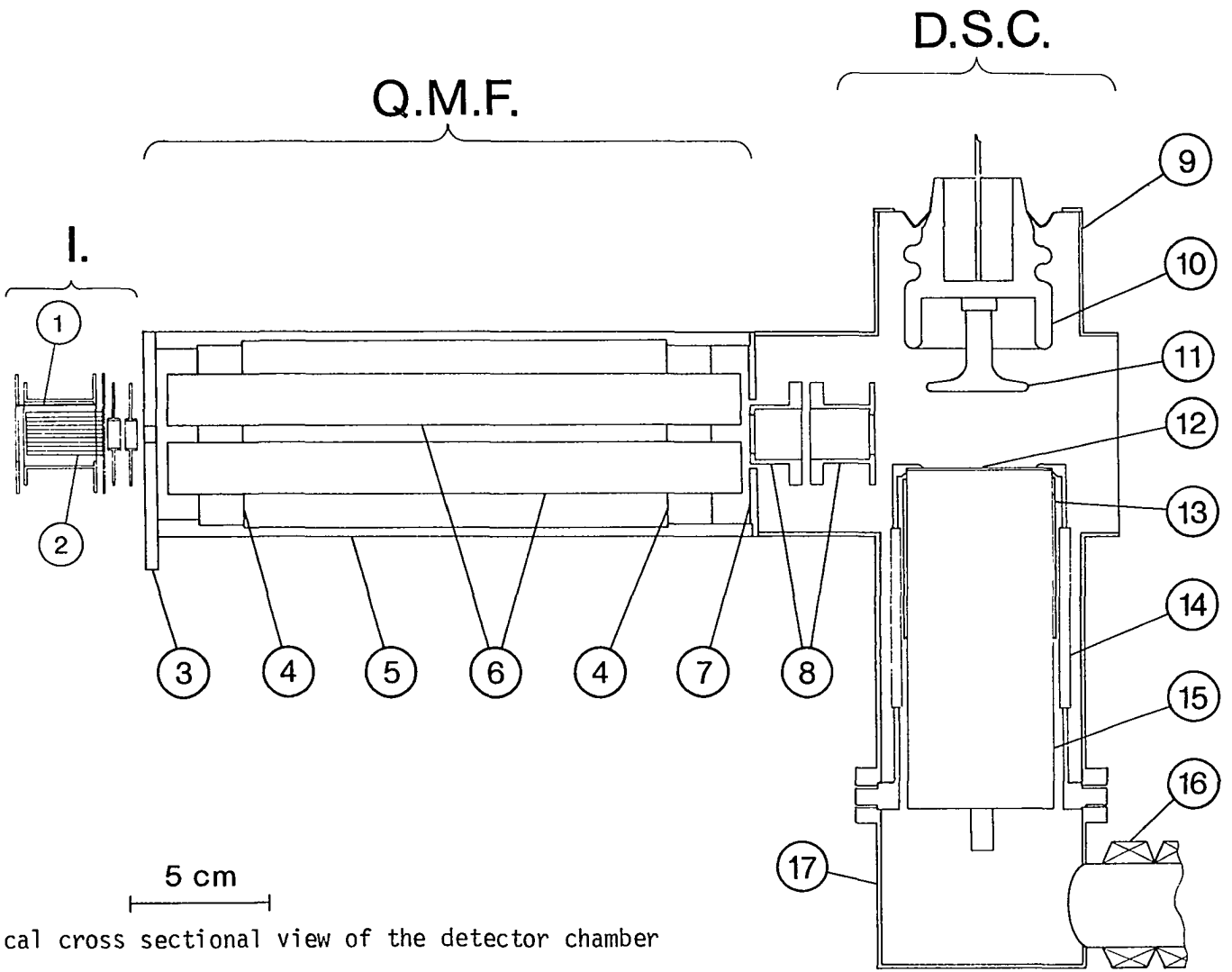

Vertical cross sectional view of the detector chamber

Macor spacers (RSM-D001) which hold the four 21.08 cm long, 1.9055 cm diameter quadrupole rods. Each rod was centerless ground to provide highly accurate cylindrical surfaces which were subsequently polished and gold plated (RSM-D002). Ions transmitted by the mass filter exit the quadrupole can rearplate (RSM-D028) where two gold plated 'exit' lenses (RSM-D003, RSM-D005) accelerate them into the scintillation counting system. A 0.15 cm wall, 7.6 cm cross is attached to the end of the quadrupole can by one arm of the cross (RSM-D002). The -30 kV ion target (RSM-D027) of the counting system is positioned by a high voltage feedthrough [35] welded into a flange mounted at the top of the cross. The 3.81 cm diameter face of the ion target has been vacuum coated [36] with aluminum to a thickness between 2000 Å and 2500 Å. Directly opposite the target, in the lower arm of the cross, is the aluminum coated face of the 4.9 cm diameter, 2.0 mm thick Pilot B plastic scintillator [37]. The uncoated face of the plastic scintillator is cemented (by NE 581 optical cement [37]) directly to the face of an RCA 8850 photomultiplier tube. Since photon counting with the photomultiplier requires the photocathode to be held at about -3 kV, the mu-metal shield around the upper half of the phototube and the aluminized face of the scintillator are floated at this (photocathode) voltage so collection and focusing by the dynodes remains uneffected. The phototube holder (RSM-D020) has a custom glass-to-stainless steel seal [38] to insulate the upper, floated section from the lower, grounded portion which contains the photomultiplier dynode chain. A special Diamonite glazed ceramic socket [39] plugs onto the rear of the 8850 phototube and supports the

high vacuum compatible resistors [40] and capacitors [41] of the dynode chain. Since there is no seal at the aluminized face of the scintillator, this entire section containing the scintillator, phototube, dynode chain and socket is evacuated via a 47.0 cm long, 3.53 cm i.d., 4.80 cm o.d., $1.0 \cdot 10^{-2}$ cm wall flexible bellows [42] to minimize outgassing into the innermost region. (This is the reason for using the special socket and dynode chain components.) The other end of the bellows connects into the first region through a port in the 'half-moon' plate. A ceramic bead insulated, oxygen-free copper wire and a shielded cable [43] inside the bellows provide the phototube voltage and signal connections, respectively, between the dynode chain and feedthroughs mounted on "8 inch" Conflat flanges in the first region. All other connections are outside the bellows and are made to feedthroughs on the first and second region "8 inch" Conflat flanges via feedthroughs in flanges on both 'half-moon' plates. (This arrangement of 'differentially pumped' feedthroughs minimizes connections through the detector chamber wall into the innermost region, thereby, maintaining the highest possible vacuum for this most critical region.) Extension springs (RSM-D041), wound from $1.3 \cdot 10^{-2}$ cm diameter beryllium copper [44], provide voltage for the ion and exit lenses. The springs are supported on 0.48 cm o.d., $8.9 \cdot 10^{-2}$ cm wall insulated stainless steel tubes mounted parallel to the 'rails'. An unsupported extension spring of $5.1 \cdot 10^{-2}$ cm diameter beryllium copper wire supplies the -30 kV of the ion target. The ionizer filament and quadrupole mass filter connecting wires are insulated but unsupported. In this way, electrical connections are secure and permit unimpeded translation of the detector.

At any position of the detector, the detection scheme for the scattered particles in this arrangement is as follows. Particles entering the ionizer are ionized and extracted, then injected into the mass filter. 'Filtered' positive ions leaving the quadrupole are accelerated by the exit lenses into the high field which bends the ions from their axial paths to strike the ion target. The impacting ions liberate several electrons per ion (e.g., ~7 electrons per N_2^+ ion, ~5 electrons per N^+ ion) from the target which accelerated by the field into the plastic scintillator. Thus, bombarded the plastic fluoresces and the resulting photons are multiplied by the phototube into a signal subsequently handled by standard photon counting techniques. A 'molecular beam timer and gate' [45] chops the detector signal at the beam modulating frequency of 150 Hz into 'open' and 'closed' channels which are treated as discussed in the Signal Considerations passage (and refer to Appendix B).

Characteristics of the Rotating Source Apparatus

Two important criteria under which crossed beam apparati may be assessed are resolving power and inherent flexibility. Discussion of resolution in crossed beam experiments centers on angular and energetic matters. These are not separable subjects, however, as a concession to clarity, they will be presented as such. In this approach, motives for particular features of the design and its flexibility will become evident. These topics will be further refined and elaborated on in the Summary and Suggestions for Future Research.

Angular resolution

The extent to which the prior and post collision trajectories are specified determines the angular resolution. As previously indicated, this is one of the dual purposes of the defining apertures and illustrating the criteria which determines their dimensions is the purpose of this section.

Consider the general case of a single beam generated by two symmetrically aligned apertures as shown in Fig. 10. The (in-plane) width of the umbra of the beam, W^u, formed by the rear aperture (i.e., the skimmer) of width S_R a distance d_{RF} from a forward aperture of width S_F, at a distance d_{FZ} beyond the forward aperture is

$$W^u = (S_F - S_R)\left\{\frac{d_{RF} + d_{FZ}}{d_{RF}}\right\} + S_R \quad . \tag{1}$$

Similarly, the penumbra breadth, W^p, at d_{FZ} is

$$W^p = (S_F + S_R)\left\{\frac{d_{RF} + d_{FZ}}{d_{RF}}\right\} - S_R \quad . \tag{2}$$

The ratio of the penumbra width to umbra width for a given configuration may be written as

$$\frac{W^p}{W^u} = \frac{\left(\frac{S_F}{S_R}\right) + 1 - \left(\frac{d_{RF}}{d_{RF} + d_{FZ}}\right)}{\left(\frac{S_F}{S_R}\right) - 1 + \left(\frac{d_{RF}}{d_{RF} + d_{FZ}}\right)} \quad . \tag{3}$$

A sharply defined 'ray' occurs for

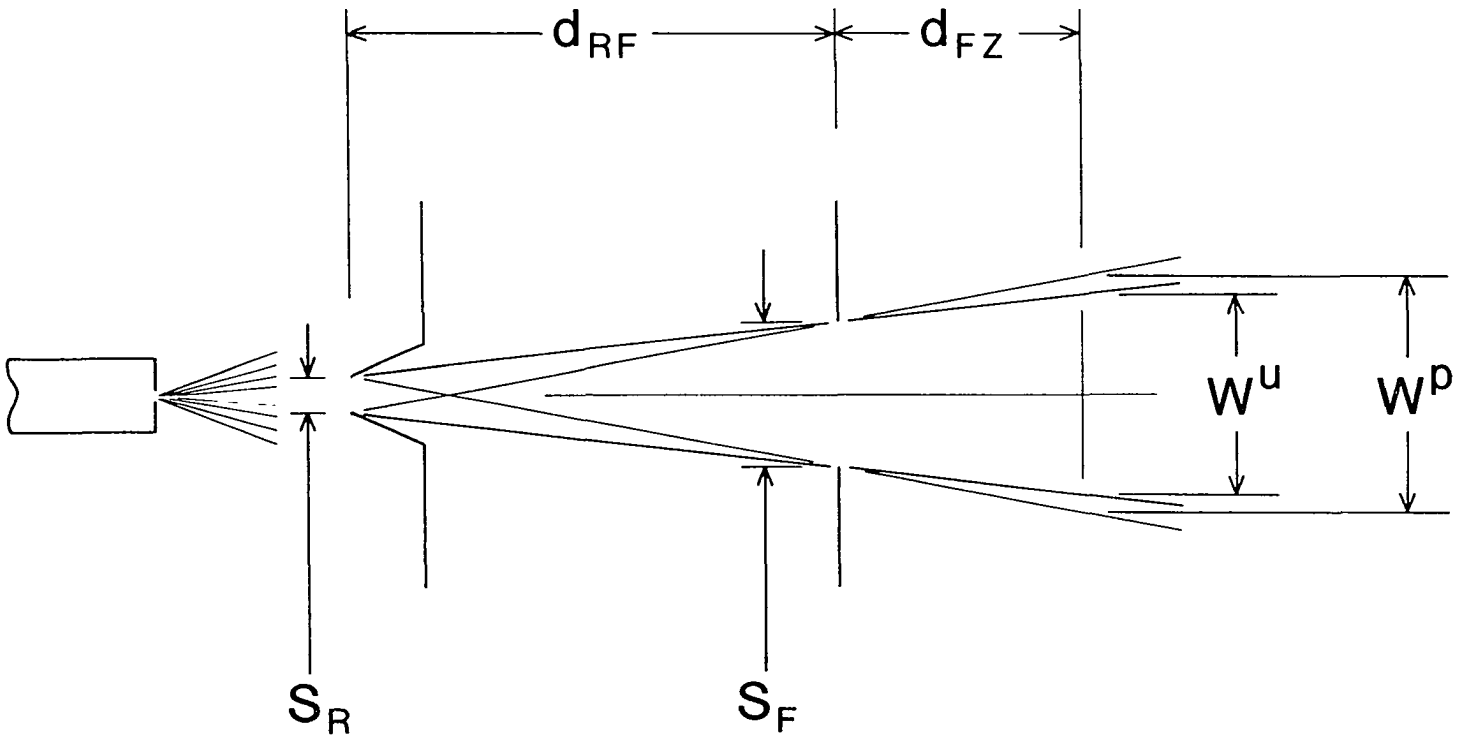

Figure 10. Single defined beam

$$\frac{W^p}{W^u} \simeq 1 \quad . \tag{4}$$

This requires

$$\frac{d_{FZ}}{d_{RF}} \rightarrow 0 \quad . \tag{5}$$

Large values for d_{RF} imply large distances between the (nozzle) source and the collision zone and correspondingly low reactant intensities. Therefore, a relatively small value for d_{FZ} is the preferred choice. The desire for well-defined beams will become apparent shortly and represents one of several arguments for a short distance (d_{FZ}) between the final defining aperture and the collision zone. Now that the single beam configuration is well in hand, the crossed beam situation may be tackled.

Figure 11 shows the (exaggerated) crossed beam situation for beam intersecting angles Γ of $\pi/2$ and $\pi/3$. Changes in Γ are accompanied by changes in the geometry of the collision zone. For a particular set of apertures, the height of the collision region is uneffected, but the area A_Z parallel to the beam plane is angle dependent. Assume, as a first approximation, both beams are sufficiently defined that their widths[1] at the collision zone, W_1 and W_2, are constant over the length of the collision region. This neglect of beam divergence is fairly

---

[1]The arguments that follow are not effected by whether these are the umbra or penumbra widths. The proper choice will become obvious. For the moment, consider Eq. (4) describes the situation.

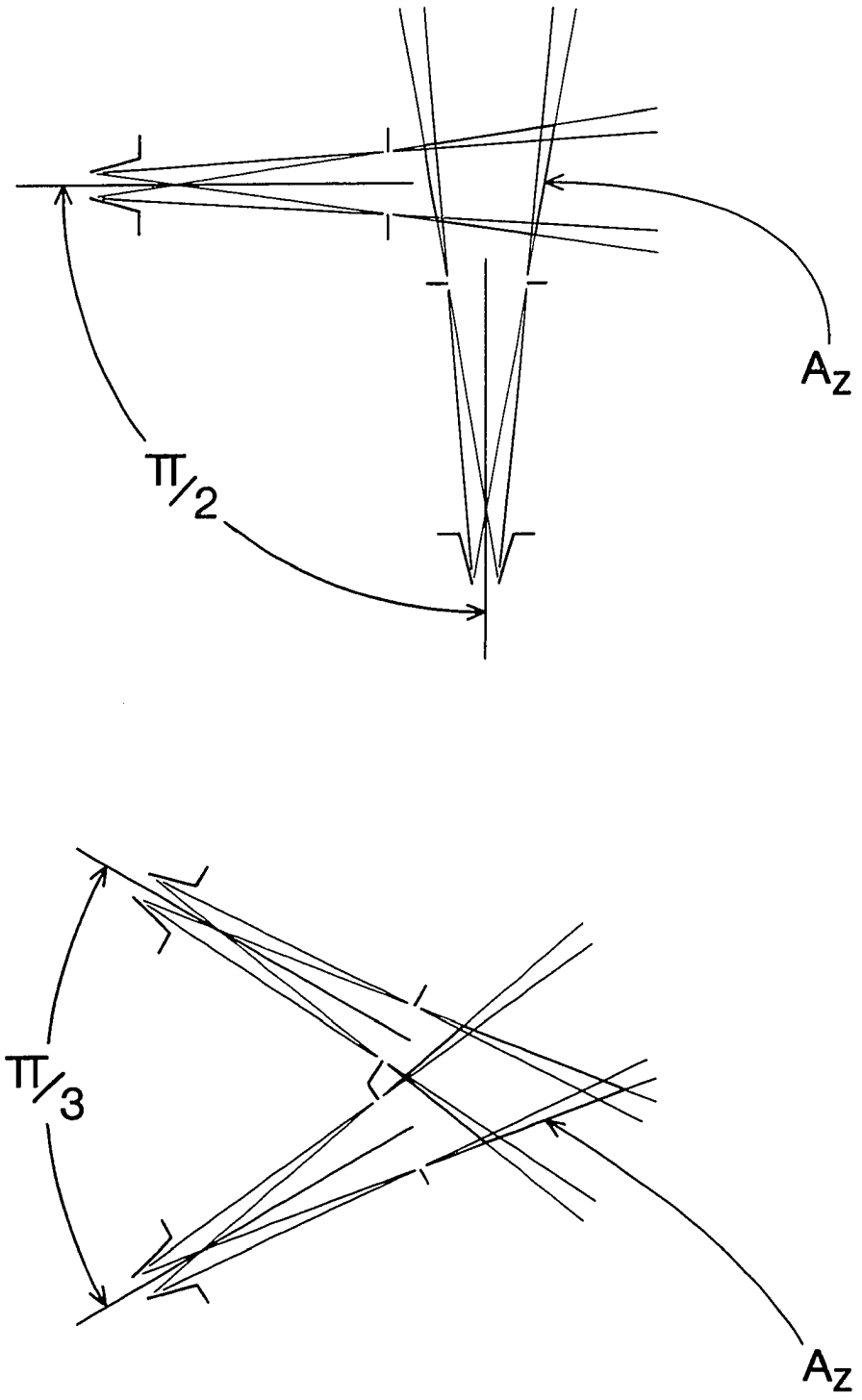

Figure 11. Crossed beam situation for crossing angles of $\pi/2$ and $\pi/3$

well-justified since typical beam angles are less than or approximately equal to 2 degrees. This assumption allows the collision regions (in-plane) area to be simply expressed as a function of the beam widths and crossing angle ($0 < \Gamma < \pi$)

$$A_Z = \frac{W_1 W_2}{\sin \Gamma} \quad . \tag{6}$$

Changing Γ to $\pi/3$ (or $2\pi/3$) increases the collision volume over that of $\Gamma = \pi/2$ by 15%. From the viewpoint of Eq. (3) of Part I, Section I for the number scattering per second, the larger the collision volume τ_Z, the greater the scattering signal. However, all the scattered intensity must be available to the detector to (potentially) be signal. Choosing to guarantee the maximum possible signal by operating with a collision zone larger than the detector 'sees' (pseudo-high resolution) introduces an angular bias into the scattering data. Theoretically, this prejudice may be corrected [46] by calculating the actual collision volume viewed by the detector at each angle (e.g., [47]), but the process is tedious and, in view of the necessary assumptions concerning the experimental geometry and distributions of velocities and densities in the (idealized) zone, is questionable in its utility. The entire issue is best avoided [48]. Thus, one is compelled to compromise between large collision volumes entirely 'visible' to the detector and the desired high angular resolution in detection. It is at this juncture that the issue of resolving angular information in initial and final states and experimental geometry becomes concrete.

Of interest then is the largest dimension of the collision zone. Simultaneous with the increase in collision volume on changing Γ from $\pi/2$ is the distortion of the diagonals of the formerly rectangular in-plane area to the long and short diagonals of the resulting parallelogram. The length of the long diagonal as a function of the crossing angle, $Y(\Gamma)$, and the (nondiverging) beam widths is given by

$$Y(\Gamma) = W_1^2 \{ 1 + [(\frac{W_2}{W_1}) \csc \Gamma + \cos \Gamma]^2 \}^{1/2} \quad . (7)$$

This, potentially, is the limitation of the angular resolution. To decide how large one can allow it to be and, thereby, the crossed beam widths, requires consideration of the detector geometry.

The maximum angular (penumbra) width viewed by the detector Θ_d, if all the (square[1]) defining apertures are perfectly aligned and of equal width S_D, with L_{RF} the distance between the first and last, is (refer to Fig. 12)

$$\Theta_D = 2 \arctan (\frac{S_D}{L_{RF}}) \quad . \quad (8)$$

The angle Θ_D represents the most deviant angle of acceptance for scattered product by the detector and is, by definition, the laboratory angular resolution. As an example, the distance L_{RF} between the forward aperture on the nosepiece (RSM-D029) in the detector chamber faceplate

---

[1]Square detector apertures make the in-plane and out-of-plane laboratory resolutions equal.

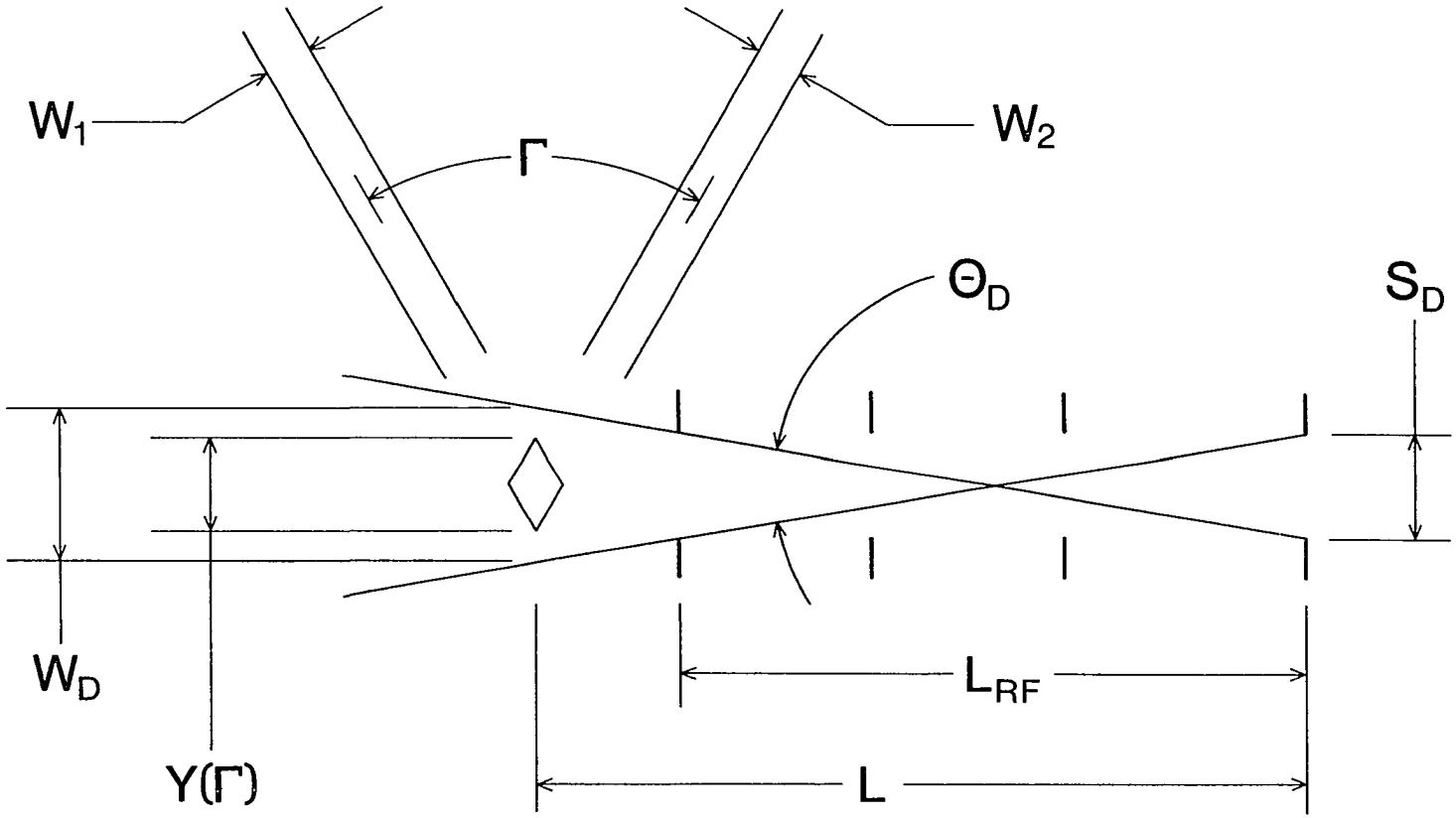

Figure 12. Detector view of the collision zone

(refer to Figs. 7a and 7b) and the aperture on the electron bombardment ionizer of the detector (in the most forward position) is roughly 20 cm. Requiring 2 degree resolution specifies apertures 0.35 cm square. The corresponding maximum width at the collision zone W_D is given by Eq. (2), in which $d_{RF} = L_{RF} = 20$ cm and $d_{FZ} \cong 6.4$ cm $\equiv L_{FZ}$, as 0.57 cm. This becomes the largest allowable value for the transverse dimension of the collision zone $Y(\Gamma)$ and nominally specifies, for $W_1 = W_2$, beam widths of $\sim$0.29 cm at the collision region for $\Gamma = \pi/3$. Increasing the resolution requires reducing the width subtended by the detector W_D and concommitantly the collision volume must contract to avoid the viewing factor problem. In the case of the rotating detector apparatus, the only avenue whereby resolution improves is the reduction of the detector apertures. For a fixed ionizer position, one can see from the equations provided,

$$\Theta_D \propto S_D \tag{9}$$

and

$$W_i \propto W_D \propto S_D \tag{10}$$

where W_i is the ith beams width at the collision zone. Because the signal S observed by a detector of effective area A_d a distance L from a collision region of volume τ_Z follows

$$S \propto \tau_Z \left(\frac{A_d}{L^2} \right) \quad , \tag{11}$$

these relationships are indeed unfortunate. Improving the resolution for the rotating detector experimental arrangement by a factor of two

requires reducing the detector apertures (S_D) and beam widths (W_i) in half. Narrowing the (square) apertures in front of the electron bombardment ionizer by a factor of two decreases the effective area A_d by four. Efficiently using this ionizer[1] means utilizing as much as possible of the total 'active' ionizing volume. The ambient background of the innermost detector region is free to experience this total volume while the scattered signal, after restriction by the apertures, 'sees' an effective area (A_d) multiplied by the active length of the ionizer as the effective volume. Clearly presenting the largest possible area of the ionizer achieves the highest ratio of the effective volume to the available volume, however, this directly opposes the desire for increased resolution. With the decrease in the beam widths, there is also a (requisite) reduction in τ_Z:

$$\tau_Z \propto W_i \quad . \tag{12}$$

Therefore, on the basis of Eqs. (8), (9), 10), and (12), the signal for the fixed detector position, $S^{F.D.}$ (which is the case for the rotating detector apparati), as a function of the angular resolution is

$$S^{F.D.} \propto \Theta_D^5 \quad . \tag{13}$$

and increasing Θ_D by 2 diminishes the signal by a factor of 32.

---

[1]These considerations argue for a 'taylored' ionizer. In view of this and documented [49] unfavorable behavior for this ionizer design (especially in time-of-flight), another taylored ionizer is planned for the future.

The same situation is available to the rotating source apparatus. (In fact, an arrangement for adjustable apertures is planned since there are advantages in terms of conductance.) However, an alternative method of improving resolution is possible by translating the detector without changing the apertures. Equation (8) implies

$$\Theta_D \propto \frac{1}{L} \quad . \tag{14}$$

The expression for the signal, Eq. (11), is encouraging in that A_d remains unchanged but discouraging in view of the inverse square dependence on L. Fortunately, as the ionizer retracts, the geometry of the situation requires only small reductions in the beam widths and, therefore, the collision volume remains substantially undiminished. Then, as a first order approximation, the signal as a function of the resolution in the translating detector scheme follows

$$S^{T.D.} \propto \Theta_D^2 \tag{15}$$

which demonstrates a strong advantage for the rotating source apparatus. Calculations based on the actual geometry show moving the ionizer from the most forward position to that which provides a factor of two improvement in resolution results in a signal diminished by a factor of about six. Nonetheless, the advantage of the translating detector scheme remains apparent in conveniently obtaining higher resolution at lower sacrifices in signal. Further, from an operational standpoint, the experimental situation may be continually optimized on the basis of the available signal and the desired resolution, thereby, obviating the

highly undesirable task of venting the (ultra-clean, ultra-high vacuum of) detector chamber to change the apertures.

Energy resolution

Full treatment of the energetics of the initial and final states of crossed beam experiments requires specific information about internal state distributions. The rotating source apparatus employs supersonic expansion in beam generation and, in the absence of any further initial state selection, can only be said to provide beams with internal state distributions 'relaxed' compared to those of the stagnation conditions in the nozzle to an extent dependent on those conditions and the species involved. Generally, supersonic beam vibrational and rotational distributions correspond to effective temperatures on the order of tens of degrees and degrees Kelvin, respectively. while translational distributions with full widths (ΔV) at half the maximum speed (V) are commonly about 10% ($= \Delta V/V$). Post collision internal state information must be obtained either directly by a state selective technique or inferred by application of conservation of energy to measured translational energy (change) of the products. State selective methods tend to be highly species specific [50,51] while observing kinetic energy (changes) via the time-of-flight technique, utilizing electron bombardment ionization, is presently more comprehensive [52]. The single universal feature of beam experiments is kinematic. In view of this fact and the unique abilities of the rotating source apparatus, a brief review of the role of kinetic energy in crossed beam experiments is in order.

For the initial state of an isolated system composed of A particle(s) of mass m_A and velocity $\vec{V}_A$ and B particle(s) of mass m_B and velocity $\vec{V}_B$, the total laboratory kinetic energy is

$$T_i^{LAB} = \frac{1}{2} m_A V_A^2 + \frac{1}{2} m_B V_B^2 \quad . \tag{16}$$

Although the collision is arranged in the laboratory (LAB), all parameters of physical interest concern the center of mass (CM) frame of reference, so transforming [53,54] allows one to write

$$T_i^{LAB} = T_i^{CM} + T^M \quad . \tag{17}$$

T_M may be considered the kinetic energy of the hypothetical particle containing the total mass of the system, $M = m_A + m_B$, moving in the laboratory at velocity $\vec{R}$; i.e.,

$$T^M = \frac{1}{2} M\vec{R}^2 \quad . \tag{18}$$

In the absence of external forces, T^M is unchanging in time and, consequently, uninteresting. T_i^{CM} represents the initial kinetic energy of a hypothetical particle of (initial) reduced mass μ_i approaching a scattering center (which is the origin of the CM frame) with velocity $\vec{r}_i$:

$$T_i^{CM} = \frac{1}{2} \mu_i \vec{r}_i^2 \tag{19}$$

where

$$\mu_i = \frac{m_A m_B}{M} \quad . \tag{20}$$

In a (more physical) two particle picture, the collision occurs ('head on' in the CM frame) between the A particle approaching with velocity $\vec{u}_A$, the B particle moving at velocity $\vec{u}_B$, where

$$\vec{u}_A = \left(\frac{\mu_i}{m_A} \right) \vec{r}_i \tag{21}$$

and

$$\vec{u}_B = - \left(\frac{\mu_i}{m_B} \right) \vec{r}_i \quad . \tag{22}$$

The situation may be summarized in velocity space by the Newton diagram, given in Fig. 13 and from which one sees

$$\vec{r}_i = \vec{V}_A - \vec{V}_B \quad . \tag{23}$$

Then, in terms of the experimental parameters, i.e., the laboratory speeds and their directions, the initial center of mass kinetic energy may be expressed as[1]

$$T_i^{CM}(V_A,V_B,\Gamma) = \frac{1}{2} \mu_i V_A V_B \left[\left(\frac{V_A}{V_B} + \frac{V_B}{V_A} \right) - 2 \cos \Gamma \right] \quad . \tag{24}$$

As previously defined, Γ is the beam intersection angle. Although the rotating detector apparati have Γ fixed at $\pi/2$, the rotating source apparatus allows variation of Γ and so the change in $T_i^{CM}(\Gamma)$ with beam

---

[1] A vectorial quantity will continue to be indicated by an arrow while absence of the arrow indicates magnitude only:

i.e., $\quad V \equiv |\vec{V}| \quad .$

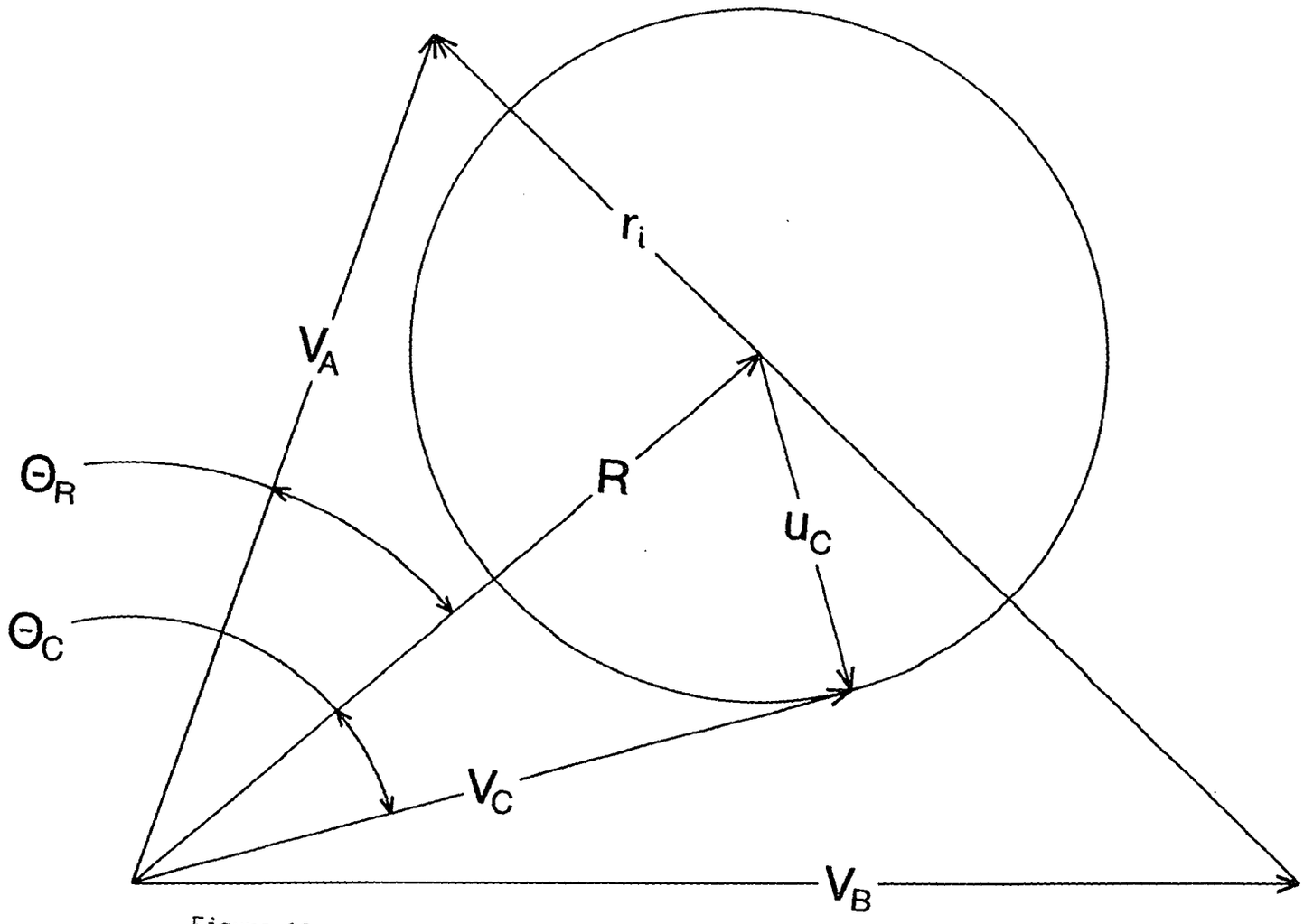

Figure 13. Newton diagram of the general two body collision

crossing angle is of interest. Comparison on the basis of the ratio of the initial CM kinetic energy at Γ to that at $\Gamma = \pi/2$ is instructive:

$$\frac{T_i^{CM}(\Gamma)}{T_i^{CM}(\Gamma = \pi/2)} = 1 - 2 \cos \Gamma \left[\left(\frac{V_A}{V_B} + \frac{V_B}{V_A} \right) \right]^{-1} \quad . \quad (25)$$

If the magnitudes of the initial LAB velocities differ greatly, altering the intersection angle will have little effect on the collision. This is obvious from the physical situation in which V_A becomes substantially greater than V_B such that V_B contributes little to the relative velocity r_i regardless of the orientation of V_B. For V_A vastly greater than V_B, the B species appear essentially as stationary targets and $\vec{r}_i \simeq \vec{V}_A$. From the point of view of manipulating the CM kinetic energy, the most advantageous case occurs for equal LAB beam speeds; $V_A = V_B$. For this case, one has, for example,

$$\frac{T_i^{CM}(\pi/3)}{T_i^{CM}(\pi/2)} = \frac{1}{2} \qquad \text{and} \qquad \frac{T_i^{CM}(2\pi/3)}{T_i^{CM}(\pi/2)} = \frac{3}{2}$$

which demonstrates the greatly increased range of accessible collision energies.

Beyond this idealized case of mono-energetic, perfectly defined beams is the actual situation involving distributions in beam velocities which consequently create uncertainty in T_i^{CM}. Is the acquired asset of flexibility in Γ accompanied by a degradation in the ability to specify T_i^{CM}? To address this problem, consider the velocity of one of the beams, say V_A, separated into speed and angular components. Then, the

relative 'error' in the CM kinetic energy due to a distribution in speed of width ΔV_A is

$$\left.\frac{\Delta T_i^{CM}}{T_i^{CM}}\right)_\Gamma = 2\left(\frac{\Delta V_A}{V_A}\right)\frac{\eta - \cos\Gamma}{(\eta + \frac{1}{\eta}) - 2\cos\Gamma} \qquad (26)$$

where $\eta \equiv (V_A/V_B)$. For the special case of $\eta = 1$, the dependence on Γ vanishes and 'speed error' affects all beam crossing angles equally. Further inspection shows variation in the value for η induces little angular dependence for essentially the same physical reason previously given. Angular error may be taken as deviation in the crossing angle, i.e., $\Delta\Gamma$, and the induced relative error is

$$\left.\frac{\Delta T_i^{CM}}{T_i^{CM}}\right)_\Gamma = \frac{\sin\Gamma}{\frac{1}{2}(\eta + \frac{1}{\eta}) - \cos\Gamma}\Delta\Gamma \quad . \qquad (27)$$

Again, if $\eta = 1$, for $\Gamma = \pi/2$, there is a factor of 1.7 increase in sensitivity to angular aberration over that for the usual case of $\Gamma = \pi/2$. This effect is actually due to the more rapid decrease in the CM kinetic energy for Γ less than $\pi/2$. For crossing angles greater than $\pi/2$, the situation becomes more tolerant of beam divergence (e.g., if $\eta = 1$, at $\Gamma = 2\pi/3$, $\Delta T_i/T_i = (1/\sqrt{3})\Delta\Gamma$). Nonetheless, the argument demonstrates in utilizing intersection angles less than $\pi/2$ well-defined beams become even more highly desirable justifying statements previously made in the discussion of beam geometry and source design.

Although a general discussion of the kinetic preparation of the initial state is possible, considerations of the laboratory appearance

of the final state can become highly specific. The reason lies in the fact that the final center of mass kinetic energy, T_{f}^{CM}, is dependent on the change ($\Delta\varepsilon$) of the products final internal state energy from that of the reactants initial internal state:

$$T_{f}^{CM} = T_{i}^{CM} - \Delta\varepsilon \quad . \tag{28}$$

The value of $\Delta\varepsilon$ is determined by the nature of the particular collision process. For example, by definition $\Delta\varepsilon = 0$ for an elastic process, and $\Delta\varepsilon$ is on the order of 1 meV and 100 meV for rotationally and vibrationally inelastic collisions, respectively, while $\Delta\varepsilon \sim \pm 5$ eV (i.e., bond energies) for reactive events. Generally, the collision produces some product species C, in some final internal state, recoiling in the CM frame with speed u_C given by

$$u_C = \left(\frac{\mu_f}{m_C}\right)\{\mu_f[\mu_i(\vec{V}_A - \vec{V}_B)^2 - 2\Delta\varepsilon]\}^{1/2} \tag{29}$$

where μ_f is the final state reduced mass for the products C and D of masses m_C and m_D, respectively. In the LAB frame, C appears with a velocity $\vec{V}_C$ given by

$$\vec{V}_C = \vec{u}_C + \vec{R} \quad . \tag{30}$$

This means the maximum LAB angular extent, relative to the center of mass vector $\vec{R}$, is (see Fig. 13)

$$\Theta_C = \arcsin\left|\frac{\vec{u}_C}{R}\right| \quad . \tag{31}$$

And the angle between the vector $\vec{R}$ and the $\vec{V}_A$ vector is

$$\Theta_R = \arctan \frac{\sin \Gamma}{\left(\frac{m_A V_A}{m_B V_B} \right) + \cos \Gamma} \quad , \tag{32}$$

$(m_A V_A \geq m_B V_B)$.

There are several implications, the first of which concerns laboratory angular resolution. In the previous discussion of this topic, it was emphasized that the largest dimension of the collision zone <u>potentially</u> represented the limitation of the angular resolution. Equation (31) implies if $|u_C| < |R|$, the distribution of C in the laboratory is limited and the entire collision zone need not be viewed allowing an improvement in resolution for the scattered C. However, if $|u_C| > |R|$, 'backscattering' occurs in the laboratory and the collision volume must be viewed at all permitted angles to obtain the utmost information. A second significant implication is the ability of the rotating source apparatus to alter the laboratory 'display' of the scattering at a given initial CM kinetic energy. This is illustrated in Fig. 14. There are two effects arising essentially from the same cause. First, the scattering intensity and, therefore, the angular information may be 'compressed' or 'expanded' in the laboratory via the choice of crossing angles and beam speeds. Second, the LAB speeds observed for the product may be, to a certain extent, controlled (refer to Eqs. (29) and (30) and Fig. 14). Both these kinematic effects are results of the (improved) control of the center of mass velocity vector, $\vec{R}$, available through the additional ability to change Γ. One may acquire a physical feeling for

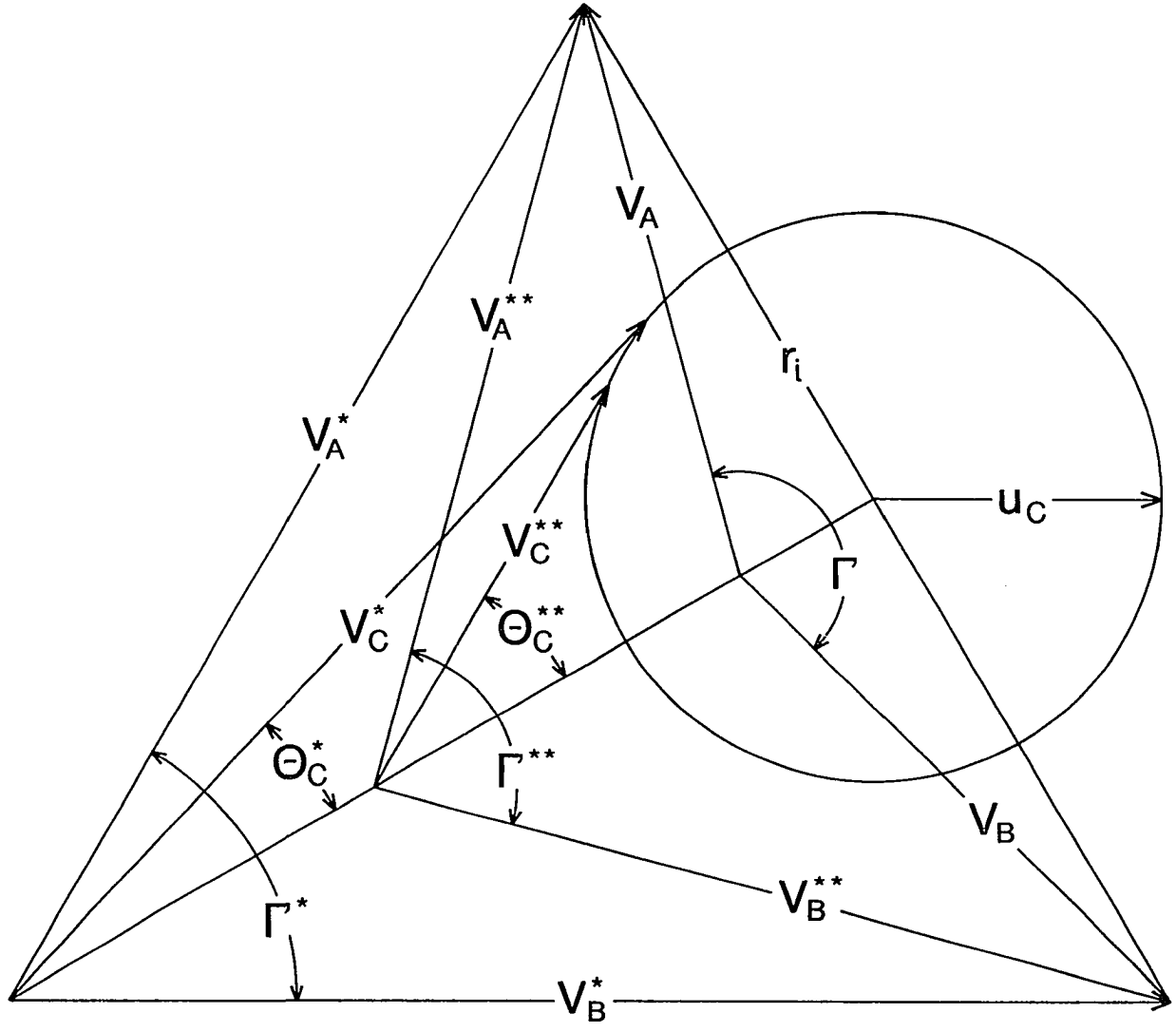

Figure 14. Altering the LAB appearance of the scattering information at fixed collision energy

the character of changes in $\vec{R}$ by considering the limiting cases of Γ = 0, in which all scattering is strongly focused 'forward' and $\Gamma = \pi$, for which the laboratory and center of mass frames are of the greatest similarity.

While manipulation of the angular intensity is important in considering scattering signals, the laboratory speed of the detected product is of concern in final state energetic analysis. The rotating source apparatus is capable of measuring product kinetic energy by the time-of-flight (TOF) technique using both single [55-58] and cross-correlation [59,60] 'chopping'. The TOF technique is a standard one (e.g., [50]) and salient features of the method as applied in the RSA may be illustrated for 'single shot' scattered beam modulation. Presently, a $3.8 \cdot 10^{-2}$ cm thick stainless steel disk, 17.8 cm in diameter has $2.5 \cdot 10^{-2}$ cm wide slots along its periphery.[1] An A.C. hysteresis synchronous [62] motor mounted in a water-cooled copper block (RSM-MC032) drives the disc at frequencies on the order of 300 Hz. The gating provides an open time Δt_G of about 10 μs (full width at half maximum) for the scattered product. After traversing a flight path of length L_F, the species is ionized somewhere along the ionizer length L_I and, subsequently, (the ion is) extracted and counted. Nominally, the flight time t_F and the path length give the species laboratory speed:

---

[1]Arrangements for the fabrication of thinner discs with highly accurate photochemically machined slots in a material with a greater ratio of tensile strength to density (i.e., beryllium copper), which allows higher angular velocities, have been made [61].

$$V = \frac{L_F}{t_F} \quad . \tag{33}$$

However, the scattered products, for a particular final state, have (because the prepared reactant beams have) velocity distributions of width ΔV such that the time-of-arrival is 'smeared' by Δt_P about the nominal flight time t_F for the most probable velocity:

$$\frac{\Delta t_P}{t_F} = \frac{\Delta V}{V} \quad . \tag{34}$$

Further, the TOF signal is distorted by the nonzero width of the gating time Δt_G, and the response time of the detection system Δt_D. If the extraction and counting of the ions is relatively rapid, then the major contribution to Δt_D arises from the finite length of the ionizer:

$$\Delta t_D \propto L_I \quad . \tag{35}$$

The contributions of these factors to the width of the time-of-arrival Δt_{TOF} for a nominal flight time t_F becomes the resolution in time:

$$\left(\frac{\Delta t_{TOF}}{t_F} \right) = \left(\frac{\Delta t_G}{t_F} \right) + \left(\frac{\Delta t_D}{t_F} \right) + \left(\frac{\Delta t_P}{t_F} \right) \quad . \tag{36}$$

The relative severity of these effects may be gauged by rewriting Eq. (36), using Eqs. (34) and (35)

$$\left(\frac{\Delta t_{TOF}}{t_F} \right) = \left(\frac{\Delta t_G}{t_F} \right) + \left(\frac{L_I}{L_F} \right) + \left(\frac{\Delta V}{V} \right) \quad . \tag{37}$$

A value for Δt_G has already been given, as 10 μs, and in the present ionizer design $L_I \sim 2.5$ cm. In the forward position of the detector,

$L_F \sim 20$ cm. For light gases (e.g., He, H_2) at room temperature, or oven-generated species, beam speeds (V) are on the order of 10^5 cm s^{-1} with speed widths of perhaps 10%. In this example, Eq. (37) gives a value of 37 μs for Δt_{TOF}. Notice that 95% of the broadening is due to the gating function and the finite ionizer length so, due to the sharpness of the speed distribution, this term may be dropped from Eq. (37), and the expression for the relative broadening of the TOF signal can be approximated as

$$\left(\frac{\Delta t_{TOF}}{t_F} \right) \simeq \frac{1}{L}\left\{ \frac{V}{v} + 1 \right\} \quad . \tag{38}$$

L and v are characteristic lengths and speeds for a particular TOF arrangement:

$$L \equiv \frac{L_F}{L_I} \quad , \qquad v \equiv \frac{L_I}{\Delta t_G} \quad .$$

This interest in the distortion of the TOF signal arises from the desire to distinguish final velocities of the products belonging to or in different internal states. Explicitly, because $\Delta T_f^{CM} \propto \Delta\epsilon$ (refer to Eq. (28)) product species will possess different flight times for different final internal states and to resolve this distinction requires the broadening of the TOF signal be less than (<1/2) the difference in the corresponding arrival times. Therefore, improving Δt_{TOF} allows smaller differences in internal states to be resolved. Ionizer design difficulties (e.g., space charge effects) and mechanical considerations of the wheel (e.g., motor speed, disc tensile strength) leave little

room for improvement in L_I and Δt_G (perhaps an increase in v by a factor of five). Although the RSA allows V to be manipulated to a certain extent, one cannot count on it in the general case, so an increase in flight path remains the only avenue of assured improvement. Randal K. Sparks in his description [63] of a new rotating detector apparatus (based on the design of Lee, McDonald, LeBreton and Herschbach) incorporating an 88.900 cm i.d. bearing states, "The original incentive for designing a new apparatus which differed significantly from the earlier machines was the desire to increase the velocity resolution for time-of-flight analysis ..., then it is necessary to achieve greater velocity resolution by means of increasing the flight path." Increasing the bearing diameter, from the 63.500 cm i.d. of the previous machines, allowed lengthening the flight path from 17.3 cm to 30.0 cm approximately doubling TOF resolution. In the rotating source apparatus, the forward position of the detector corresponds to a flight path of 20 cm, roughly that of the earlier rotating detector apparati, while the fully retracted position is an additional 60 cm further back. This arrangement permits continuously adjustable TOF resolution to allow optimization on a case by case basis for state resolution with respect to available signal, etc. (up to a factor of 2 1/2 over the "new" RDA). Furthermore, because the detector is enclosed in what is essentially a separate unit, i.e., the detector chamber, a spacer of the desired length can be inserted between the detector chamber flange and (the north plate of) the main chamber to provide even longer flight paths limited, in principle, only by the wall of the laboratory.

However, at some point, the utility of the energy change method must be called into question. The resolution obtained by the energy change method is roughly

$$\frac{\Delta T_{\ell}^{CM}}{T_{i}^{CM}} \simeq 5 \cdot 10^{-2}$$

while state selective techniques have achieved resolution greater by a factor of ~50. As the behavior of more complex species (with higher state densities) at a greater range of energies becomes examined, state to state studies involving energy change become more and more difficult. Cognizance of this inevitability motivated the design of the rotating source apparatus to be compatible with the (evolving) laser technology. This will be touched on in the Summary and Suggestions for Future Research.

Summary and Suggestions for Future Research

Presently, the rotating source apparatus (RSA) has not matured to the point of producing preliminary results. All chambers have been assembled and tested and only installation of the detector remains. As an important example, the critical seals of the rotating plate assembly (e.g., the graphite embedded Tec-Seals) have been tested and even the maximum pressure (mid 10^{-4} Torr range) in the first stage of source differential pumping failed to produce a measurable rise in the main chamber or source second stage pressures. The RSA is in the middle of its fourth year of design and third year of assembly. In view of the

expense, complexity, originality of the device and the fact that a single researcher has been responsible for the design and assembly, the project has progressed rapidly.

Even a partial summary of the capabilities and flexibility of the apparatus is difficult, but the implications of some salient features of the design should be emphasized.

The small beam crossing angles permitted by the present beam source chambers allow (threshold) behavior at low collision energies to be studied. These experiments and others involving diminutive cross sections will benefit by the kinematic focusing and adjustable detector distance. If the scattering signals are still too low, replacement of a flange in the innermost wall (item 4 in Fig. 7a and item 3 in Fig. 7b) with an extended 'cap' will allow the detector to advance from ∿26 cm to within ∿21 cm of the collision region. If one is permitted to completely sacrifice the third stage detector differential pumping by removing the 'cap' or flange altogether a detector-collision region distance of ∿16 1/2 cm is possible. (Comparison to the fixed detector-collision region distances of ∿21 cm and ∿34 cm of the 'smaller' and 'larger' rotating detector apparati is instructive.) The beam source chambers are removable and for high energy studies (e.g., collisional dissociation) involving beam crossing angles greater than or equal to 90 degrees, replacing them with wider beam source chambers that utilize the full 80 degree 'window' throughout their entire height can provide substantial conductance gains in the first differential region. Studies involving a single beam source, such as photofragmentation, can

profit by replacing the rotating plate as well with a larger 'window'. Further, by using the opposite rotating plate, up to three stages of intense source pumping are conveniently possible in the single beam arrangement. However, beyond the highly flexible nature of this design with respect to more conventional crossed beam studies is the inherent ease with which techniques involving lasers may be incorporated.

Lasers and the RSA[1]

Drullinger and Zare in a 1969 paper titled Optical Pumping of Molecules [64] indicate that the "technique of selective excitation of molecular levels also creates the opportunity to prepare oriented or aligned samples which may be used as targets for subsequent chemical kinetics studies in ... crossed molecular beams." Three years later, Zare and co-workers stated, "Reaction scattering studies have been greatly stimulated by the advant of the 'supermachine', a molecular beam apparatus that includes universal detection by electron-impact ionization and mass analysis of the ions. However, this device does not seem well-suited for determining the vibrational-rotational distribution of the reaction products" [65]. Zare has not been alone in recognizing the limitations of state resolution in crossed beam apparati (i.e., time-of-flight) or the pursuit of state selective chemistry via laser techniques. A variety of approaches and experimental apparati have

---

[1]Another suitable light source is synchrotron radiation. Incorporating photoionization detection in an apparatus such as this has been suggested by R. Grover.

rapidly developed. (The rotating detector apparatus, with which the reader is by now familiar, has been capable of experiments involving a single molecular beam and crossing laser beam [66,67].) Still, in a recent monograph devoted to and titled Chemical Dynamics via Molecular Beam and Laser Techniques [68], Bernstein asks, "How can we 'couple' lasers with molecular beams?" To the extent that crossed molecular beams provide the suitable means for the dynamical study of a process, the author's answer, to this somewhat rhetorical question, is the rotating source apparatus. The design of this apparatus has been based not only on improving the proven techniques of the past (e.g., electron bombardment ionization and time-of-flight), but on incorporating the promising, present state-of-the-art techniques. How lasers are incorporated in the RSA is best summarized via Fig. 15. It can be seen that almost every point in the beam plane, after the skimmer of either source, is conveniently accessible to laser beams introduced either along the source axis of rotation through the source second differential region or through the rear of the detector chamber via the "10 inch" Conflat flange of the detector 'cap'. Optical pumping of the reactant species in either beam can be performed by attaching mirrors (or prisms) to the bottom of the beam source chamber such that they intercept the laser beam entering along the axis of source rotation and redirect it to the desired location along the molecular beam. In this manner, reactants may be irradiated at any point prior to the collision region <u>regardless</u> of the source movement or orientation. The collision zone is even more easily accessible and so problems associated with the lifetimes of the

prepared reactants can be, to the greatest possible extent, solved. Illuminating the products in the collision zone as previously described or via a laser beam co-axial with the detector axis (see Fig. 15) allows techniques such as laser-induced fluorescence (LIF) to be performed to ascertain product state information, as suggested by Zare. In fact, preliminary results for the energy dependence of vibrationally inelastic collisions between He and I_2 using just this scheme have recently been obtained in a pulsed beam rotating source apparatus based on the rotating source arrangement of the RSA [69]. Selective photoionization of scattered product molecules, via laser multiphoton ionization (MPI), is possible anywhere along the detector axis from the collision region to the innermost region. Attaching the required optical components to the translating detector incorporates MPI with electron bombardment ionization and mass spectrometry; the best of both worlds.

Due to their intensity, monochromaticity, and tunability, lasers have become powerful tools for achieving state preparation and detection [70]. The crossed beam situation allows the arrangement of well-defined collisions between prepared initial states of the reactants and prevents the loss of information contained in the scattered products. Indeed, lasers and molecular beams have already proven to be an excellent combination for the detailed study of state selective dynamics. And for the future? It is now Bernstein's opportunity to reply [71], "Perhaps, then, it is not merely a speculation but a straightforward extrapolation to conclude that molecular beam and laser techniques will lead to truly dramatic developments in the field of chemical reaction

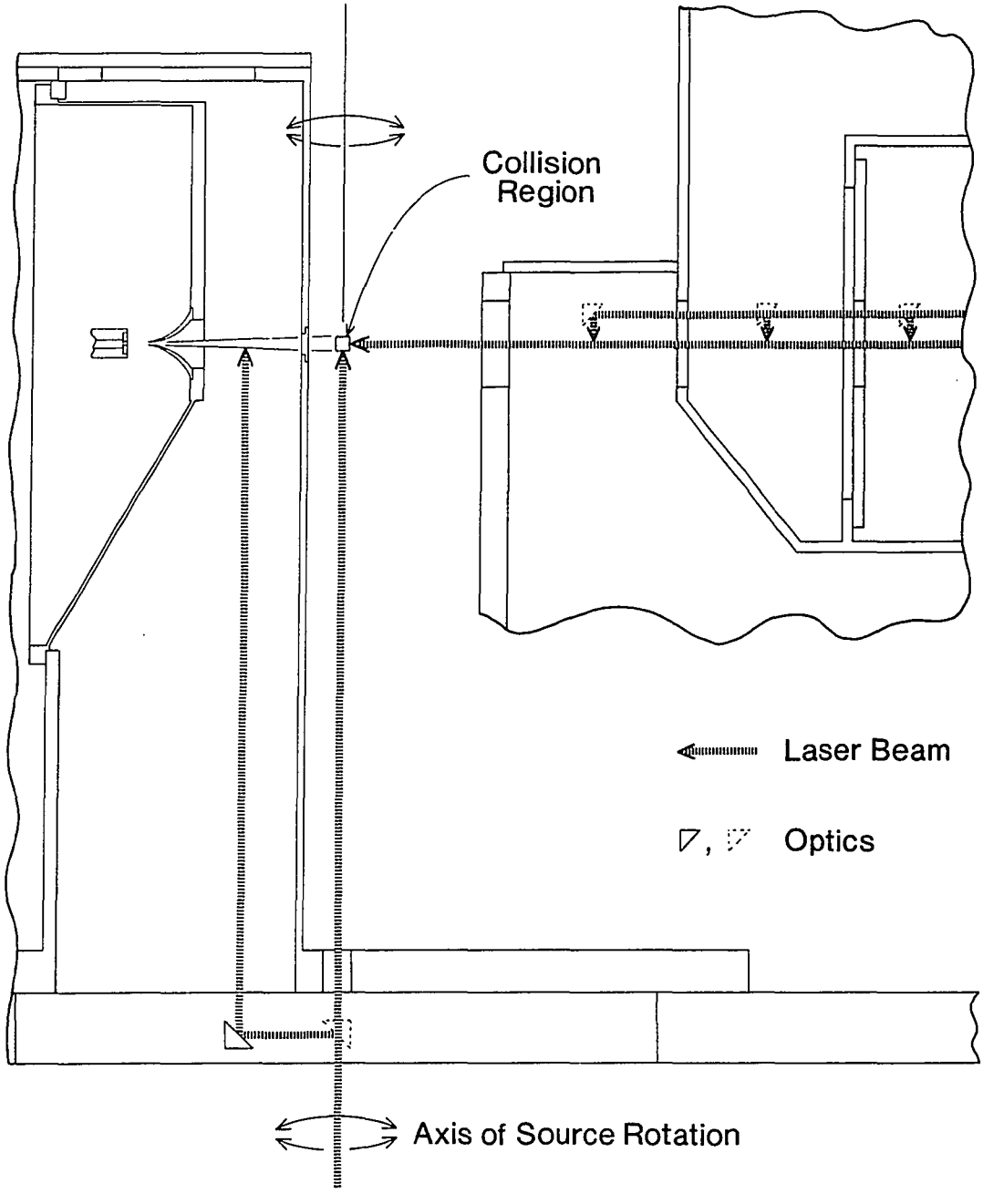

Figure 15. Methods for introducing laser beams in the RSA

dynamics in the years to come." Advancing laser technology and technique can only advance the rotating source apparatus and, if the highly flexible character of this design is exploited carefully, the prospects are indeed promising that this apparatus will be at the forefront of the "truly dramatic developments" which await this field.

References

1. S. J. Riley, Ph.D. Dissertation, Harvard University, Cambridge, MA, 1970.
2. Note that, due to the complexity of most items, several drawings were normally required. Listed are only those drawings deemed most helpful. Drawings are available through: Document Library, 201 Spedding Hall, Ames Laboratory-USDOE, Ames, Iowa 50011.
3. Adept Manufacture, Inc., 175 E. Paularino Ave., Costa Mesa, CA 92626.
4. Parker Seal, 2360 Palumbo Dr., Lexington, KY 40509.
5. Model 5010, Airco Temescal, 2850 Seventh St., Berkeley, CA 94710.
6. Dow Corning DC705 diffusion pump oil, Fisher Scientific, P.O. Box 151, Itasca, IL 60143.
7. VHS-10 diffusion pump, Varian/IEG, 708 Landwehr Rd., Northbrook, IL 60062.
8. Trivac D30A two stage rotary vane pump, Leybold-Heraeus, 5700 Mellon Rd. Export, PA 15632.
9. Monarch Machine Corp., 11642 E. Washington Blvd., Whittier, CA 90606.
10. Commercial Machine Works, 1099 Touhy Ave., Elk Grove, IL 60007.
11. Dow Corning DC704 diffusion pump oil, Fisher Scientific, P.O. Box 151, Itasca, IL 60143.
12. VHS-400 diffusion pump, Varian/IEG, 708 Landwehr Rd., Northbrook, IL 60062.

13. Trivac D60A two stage rotary vane pump, Leybold-Heraeus, 5700 Mellon Rd., Export. PA 15632.

14. Felker Brothers Corp., 22 N. Chestnut Ave., Marshfield, WI 54449.

15. VHS-6 diffusion pump, Varian/IEG, 708 Landwehr Rd., Northbrook, IL 60062.

16. Open type pillow block SPB-20-OPN ball bushing, Thomson Industries, Inc., Manhasset, NY 11030.

17. Keydon Reali-Slim KG350XPO bearing, Keene Corp., Kaydon Bearing Division, 2860 McCracken, Muskegon, MI 49443.

18. Type AO-1926, Fluorocarbon, Mechanical Seal Division, 10871 Kyle St., Los Alamitos, CA 90720.

19. Phosphor bronze worm gear GB8100 driving worm HL1076, Boston Gear Works, 14 Hayward, Quincy, MA 02171.

20. SS400 stepping motor and P2 planetary gear reducer, Superior Electric, 799 Roosevelt Rd., Glen Ellyn, IL 60137.

21. Model 1, Beam Dynamics, 623 East 57th St., Minneapolis, MN 55417.

22. Perkin-Elmer, Vacuum Product Division, 6509 Flying Cloud Dr., Eden Prairie, MN 55344.

23. Open type pillow block SPB-10-OPN ball bushing, Thomson Industries, Inc., Manhasset, NY 11030.

24. Model 951-5227 swing gate valve, Varian/Industrial Components Division, 3100 Jay St., Santa Clara, CA 95050.

25. TPU 330 turbomolecular pump, Balzers, 8 Sagamore Park Rd., Hudson, NH 03051.

26. Trivac D8A two stage rotary vane pump, Leybold-Heraeus, 5700 Mellon Rd., Export, PA 15632.

27. Model 28192-1 right angle valve, Leybold-Heraeus, 5700 Mellon Rd., Export, PA 15632.

28. Model 207-0232 D-I ion pump, Perkin-Elmer, Vacuum Products Division, 6509 Flying Cloud Dr., Eden Prairie, MN 55344.

29. Drawing/Model 1-14-81C, Janis Research Co., 22 Spencer St., Stoneham, MA 02180.

30. Model 7535 G, Hyspan, 1844 Imperial Ave., San Diego, CA 92102.

31. Model 281-6060 rotary feedthrough, Perkin-Elmer, Vacuum Products Division, 6509 Flying Cloud Dr., Eden Prairie, MN 55344.

32. N. R. Daly, Rev. Sci. Instr. 31, 264 (1960).

33. Harper-Leader, Inc., 1046 S. Main St., Waterbury, CT 06720.

34. H. Cross Co., 363 Park Ave., Weehawken, NJ 07087.

35. Model IR-17-14-4, Alberox Corp., Industrial Park, New Bedford, MA 02745.

36. Acton Research Corp., 525 Main St., Acton, MA 10720.

37. Nuclear Enterprises, Inc., 931 Terminal Way, San Carlos, CA 94070.

38. Larson Electronic Glass, P.O. Box 371, Redwood City, CA 94063.

39. Products for Research, Inc., 88 Holten St., Danvers, MA 01923.

40. Type MS power resistor, Caddock Electronics, 1717 Chicago Ave. Riverside, CA 92507.

41. Ceramic capacitors, Republic Electronics, 176 E. 7th St., Patterson, NJ 07524.

42. Bellows 188-81-25-EE, Standard Welded Bellows, 375 Turnpike Ave. Windsor Locks, CT 06096.

43. Model 949C742-3, Ceramaseal, Inc., New Lebanon Center, NY 12126.

44. Instrument Specialties, P.O. Box A, Delaware Water Gap, PA 18327.

45. Drawing ALE 1976, Ames Laboratory Instrumentation Services Group, Ames Laboratory-USDOE, Iowa State University, Ames, Iowa 50011.

46. C. A. Mims, Ph.D. Dissertation, University of California, Berkeley, CA, 1973.

47. D. D. Parish and R. H. Herm, J. Chem. Phys. 51, 5467 (1969).

48. R. Behrens, Jr., Ph.D. Dissertation, University of California, Berkeley, CA, 1975.

49. In private communication with Dr. Z. J. Zhang, University of California, Berkeley, CA, 1981.

50. M. A. D. Fluendy and K. P. Lawley, Chemical Applications of Molecular Beam Scattering (Chapman-Hall, London, 1973), Chapter 4.

51. H. Pauly and J. P. Toennies, in Methods of Experimental Physics, Atomic and Electron Physics, Atomic Interactions, Part A (Academic Press, New York, 1968), Vol. 7.

52. M. Faubel and J. P. Toennies, Adv. At. Mol. Phys. 13, 229, 1978.

53. H. Goldstein, Classical Mechanics (Addison-Wesley Publishing Co., Reading, MA, 1965), p. 58.

54. E. J. Konopinski, Classical Descriptions of Motion (W. H. Freeman and Co., San Francisco, 1969), Chapter 5.

55. O. F. Hagena and A. K. Varma, Rev. Sci. Instr. 39, 47 (1968).

56. J. A. Alcalay and E. L. Knuth, Rev. Sci. Instr. 40, 438 (1969).

57. O. F. Hagena, Rev. Sci. Instr. 41, 893 (1970).

58. W. S. Young, Rev. Sci. Instr. 44, 715 (1973).

59. K. Sköld, Nucl Instrum. Methods 63, 114 (1968).

60. V. L. Hirschy and J. P. Aldridge, Rev. Sci. Instr. 42, 381 (1971).

61. American Chemical Etching, Inc., 13730 Desmond St., Pacoima, CA 91331.

62. Type FC single phase A.C. motor, Globe Industries, 2275 Stanley Ave., Dayton, OH 45404.

63. Randal K. Sparks, Ph.D. Dissertation, University of California, Berkeley, CA, 1979, p. 104.

64. R. E. Drullinger and R. N. Zare, J. Chem. Phys. 51, 5532 (1969).

65. A. Schultz, H. W. Cruse and R. N. Zare, J. Chem. Phys. 57, 1354 (1972).

66. E. R. Grant, M. J. Coggiola, Y. T. Lee, P. A. Schulz, Aa. S. Sudbo and Y. R. Shen, in State to State Chemistry, edited by P. R. Brooks and E. F. Hayes, ACS Symposium Series 56, 1977.

67. Randal K. Sparks, Ph.D. Dissertation, University of California, Berkeley, CA, 1979, Part I.

68. R. B. Bernstein, Chemical Dynamics Via Molecular Beam and Laser Techniques (Oxford University Press, New York, 1982), p. 5.

69. G. Hall, K. Liu, M. J. McAuliffe, C. F. Giese and W. R. Gentry, J. Chem. Phys. 78, 5260 (1983).

70. See for a general treatment: V. S. Letokhov, Non-Linear Laser Chemistry (Springer-Verlag, New York, 1983), Chapter 7.

71. R. B. Bernstein, Chemical Dynamics Via Molecular Beam and Laser Techniques (Oxford University Press, New York, 1982), p. 241.

GENERAL CONCLUSIONS

To have squeezed the universe into a ball
To roll it towards some overwhelming question.
T. S. Eliot

The dilute nature of the beam situation allows highly specific and diverse collisions to be prepared and observed as demonstrated by the photoionization studies of hydrogen sulfide and its clusters and the discourse on the rotating source crossed neutral-neutral molecular beam apparatus. However, the strength of the technique is also its weakness in that carefully arranged and implemented technology enabling sensitive detection of the minute number of interesting events is required. Nonetheless, in view of the fundamental and ubiquitous nature of the collision and the detailed information obtained, these efforts are scientifically well-justified.

APPENDIX A. PUMPING SPEED AND CONDUCTANCE

> "However well fitted atomic theories may be to reproduce certain groups of facts, the physical inquirer who has laid to heart Newton's rules will only admit those theories as *provisional* helps and will strive to attain, in some more natural way, a satisfactory substitute."
>
> Ernst Mach

What began as unsupported, unpopular and basically daring speculations by Bernoulli, Joule, Clausius, Maxwell and others has developed into an aesthetically pleasing and highly useful theory. The early experimental work of Perrin, Loschmidt, Gaede, Knudsen, etc. undisputedly established the kinetic theory of gases. The study of gas flow in tubes, notably by Knudsen [1], led to characterization of the vacuum regimes on the basis of the ratio of the mean free path of the molecules $\bar{\ell}$ to some characteristic tube dimension D such as the radius r for tubes with circular cross sections. In (crossed) beam apparati, the prevailing regime is that of molecular flow for which

$$\bar{\ell} \gtrsim D$$

or, where appropriate,

$$\bar{\ell} \gtrsim r \quad .$$

Because generating molecular beams requires generating gas loads (refer to Section I of Part I), one is interested in the rate at which gas may be removed. The effective removal rate or effective pumping speed S_{eff} for a gas at a particular location is determined by the available

pumping speed S and the conductance C:

$$\frac{S_{eff}}{S} = \left(1 + \frac{S}{C} \right)^{-1} \quad .$$

Figure A1 shows a semilog plot of S_{eff}/S versus S/C. Two situations are readily apparent. First, the 'pumping speed limited' case where if

$$\frac{S}{C} < \frac{1}{10} \quad ,$$

then $S_{eff} \simeq S$ and second, the 'conductance limited' case where if

$$\frac{S}{C} > 10 \quad ,$$

then $S_{eff} \simeq C$. Pump systems represent expensive investments. Figure A2 shows the semilog plot of oil diffusion pump price [2], in thousands of dollars (K$) versus pumping speed for air, in thousands of liters per second (kl/s). It must be emphasized that these are only the diffusion pump prices and the necessary backing pumps, foreline traps, and valves, etc. are not included and, when taken into account, greatly 'accelerate' the illustrated trend. For ultra-high, ultra-clean vacuums, diffusion pumps are unsuitable and other pumping techniques must be employed. One type of inherently clean ultra-high vacuum pumping is provided by ion pumps (which represent the only active, isolated pumping system that, more or less, permanently removes gas species). Figure A3 shows the price, in thousands of dollars (K$), versus pumping speed for air in liters per second (l/s) for two ion pump designs [3]. All pumping speeds are species dependent and ion pumps are perhaps an extreme example. For instance, the pumping speed

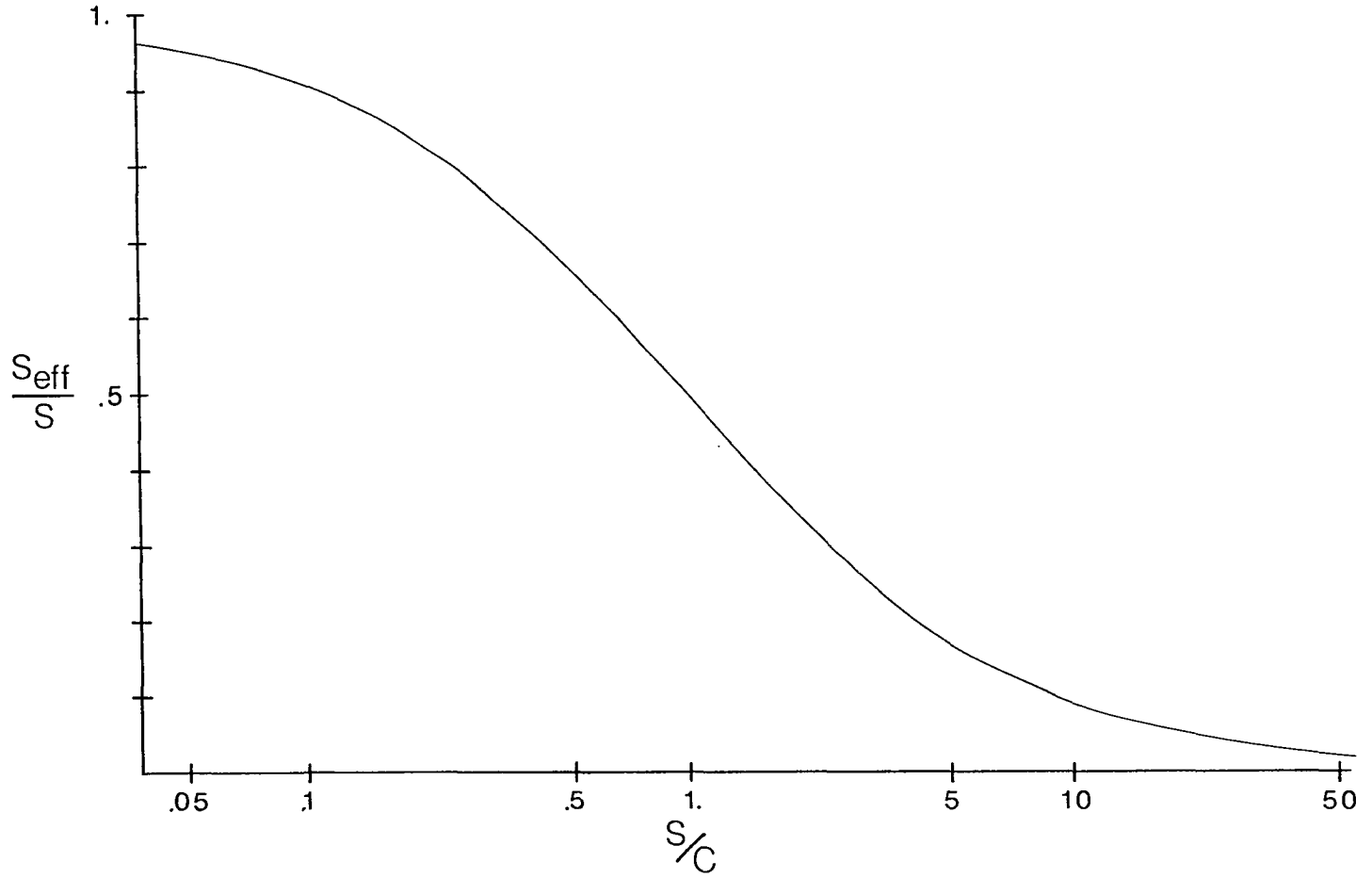

Figure A1. S_{eff}/S versus S/C

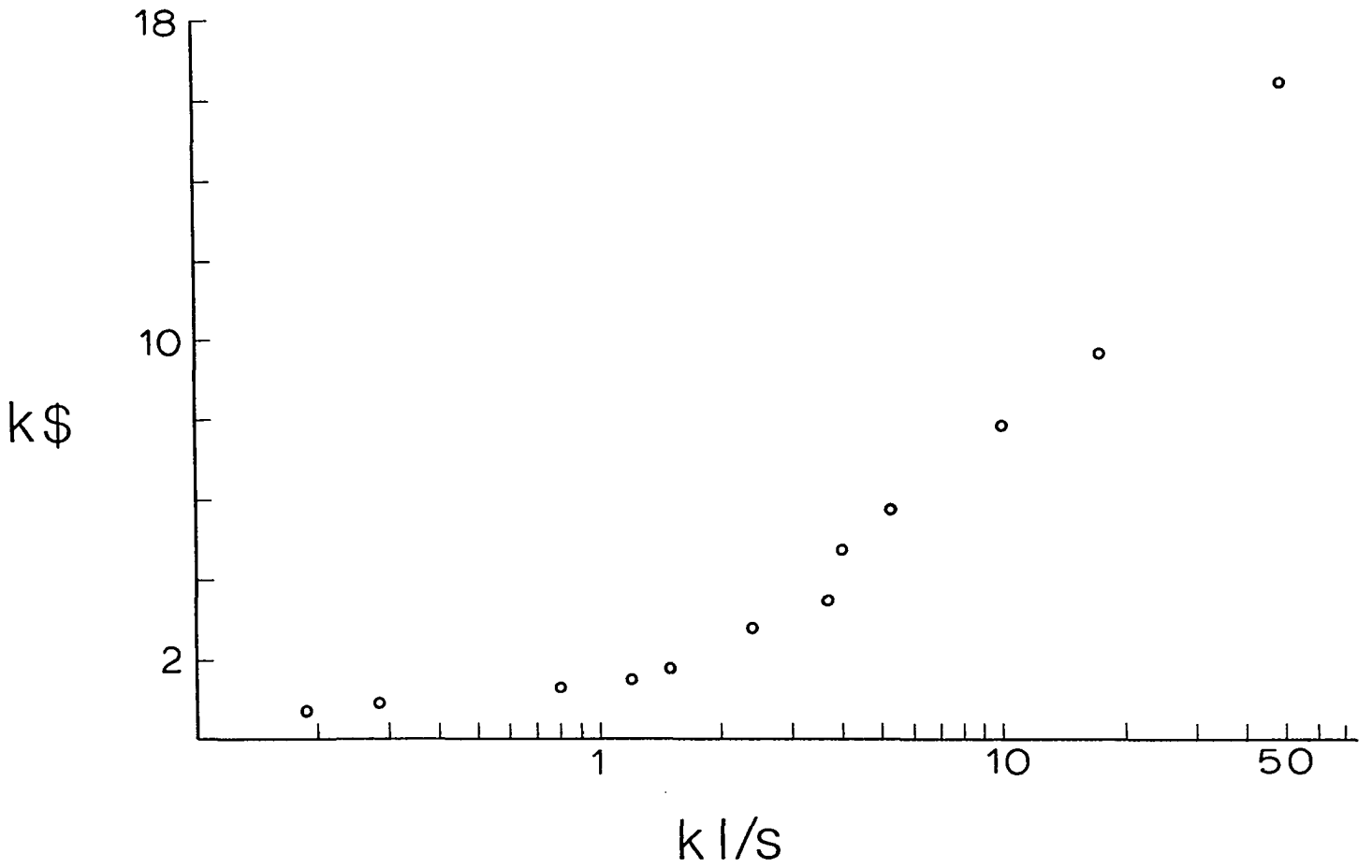

Figure A2. Diffusion pump cost versus pumping speed

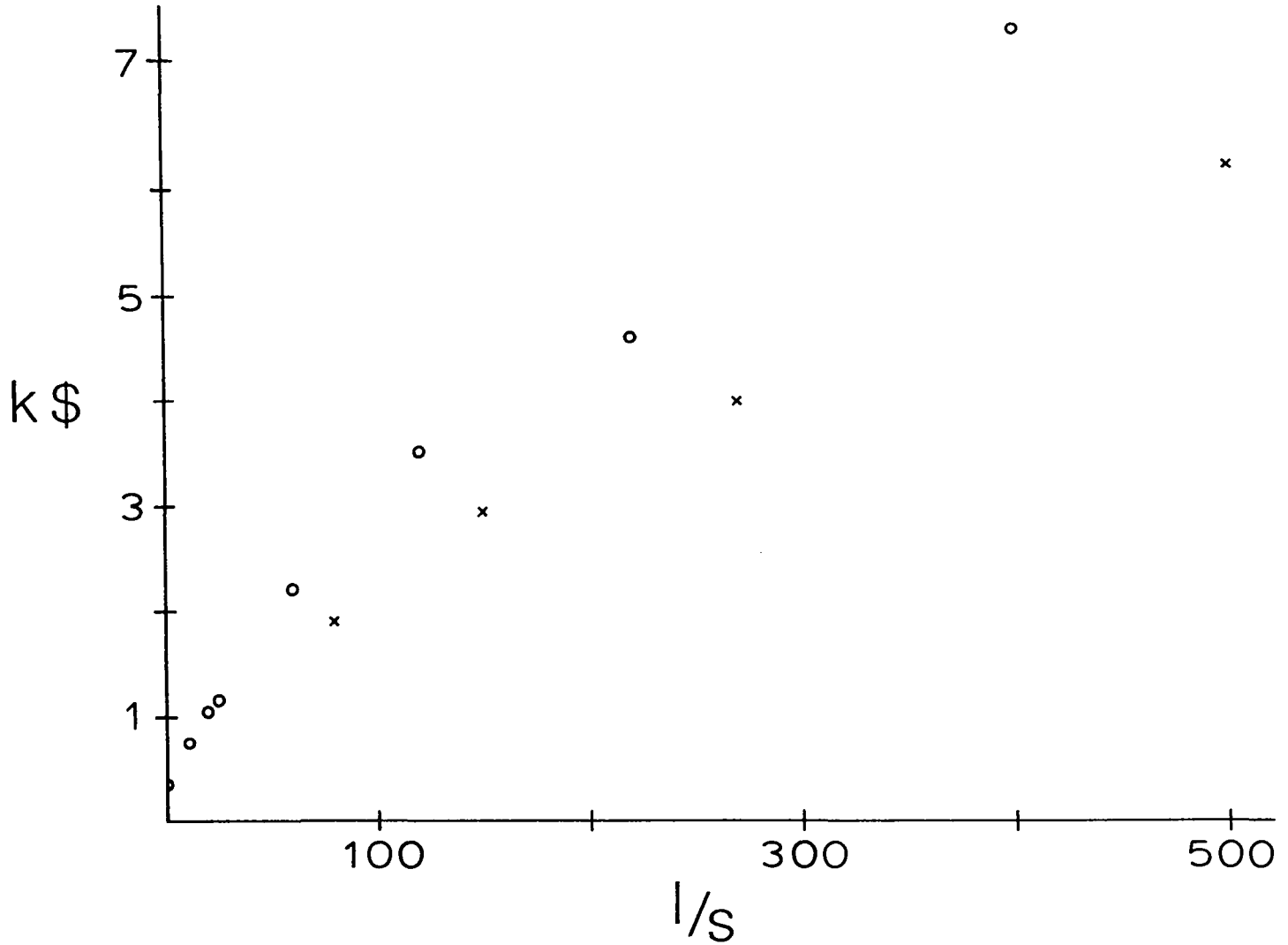

Figure A3. Ion pump cost versus pumping speed

for argon is about 2% of that for air in the conventional ion pump design (x of Fig. A3) while special design (o of Fig. A3) can raise this to about 20%. In view of the expense, the pumping speed actually available, and concrete experimental demands, one attempts to obtain the highest return for one's investment by efficiently using the available pumping speed. Figure A1 provides an indication as to how successful one has been or will be. The luxury of the 'pumping speed limited' condition is usually the result of a design 'accident' in which the mechanical connection to the pump is beneficially large. On the other hand, the unfavorable 'conductance limited' condition represents poor design judgment or an unavoidable situation.

In the molecular flow regime, the value of the conductance depends on the temperature and the particular species involved. Consider the well-known result of the kinetic theory of gases for effusive flow of a gas through an infinitesimally thick circular orifice of radius r (into a perfect vacuum):

$$Q_S = n_S \left(\frac{\bar{V}_S}{4} \right) \pi r^2 \quad .$$

The throughput Q_S for the species S is proportional to the density n_S and average speed $\bar{V}_S$ of the S molecules. Notice the first term is proportional to the pressure of the gas, the second term to the nature of the gas, and the third term reflects the nature of the orifice. This allows the expression to be recast as

$$Q_S = C_S P_S$$

where P_S is the pressure of and C_S is the conductance for the species S at some temperature. For air at ∿300K, the conductance, in liters per second, for an infinitesimally thick circular orifice of radius r, in

$$C(0) = 36.7\ r^2 \quad .$$

Unfortunately, pumps are not attached to vacuum systems by infinitely short connections. The additional resistance to gas flow due to the length L of a cylindrical tube has been calculated by Clausing [4]. The Clausing factor K, a function of the ratio of the length L of the tube to its radius, corrects the orifice conductance C(0) to that of the tube C(L):

$$C(L) = K\ C(0)$$

$$= K\ (36.3)\ r^2 \quad .$$

Figure A4 shows a semilog plot of the Clausing factor versus the ratio L/r. Notice conductance is lost extremely rapidly at first. For example, when the tube length has become equal to the tube diameter, the (tube) conductance has dropped to ∿50% of the orifice, however, extending the tube length to twice the diameter only reduces the conductance an additional 15%. This knowledge has engendered the rule of thumb for vacuum connections "as short and as large as possible" which is of little use in making concrete design decisions. Figure A5 shows the semilog plot of the rate of change of K with the ratio L/r, $\Delta K/\Delta(L/r)$, versus L/r. From this figure, one sees K begins to decrease less

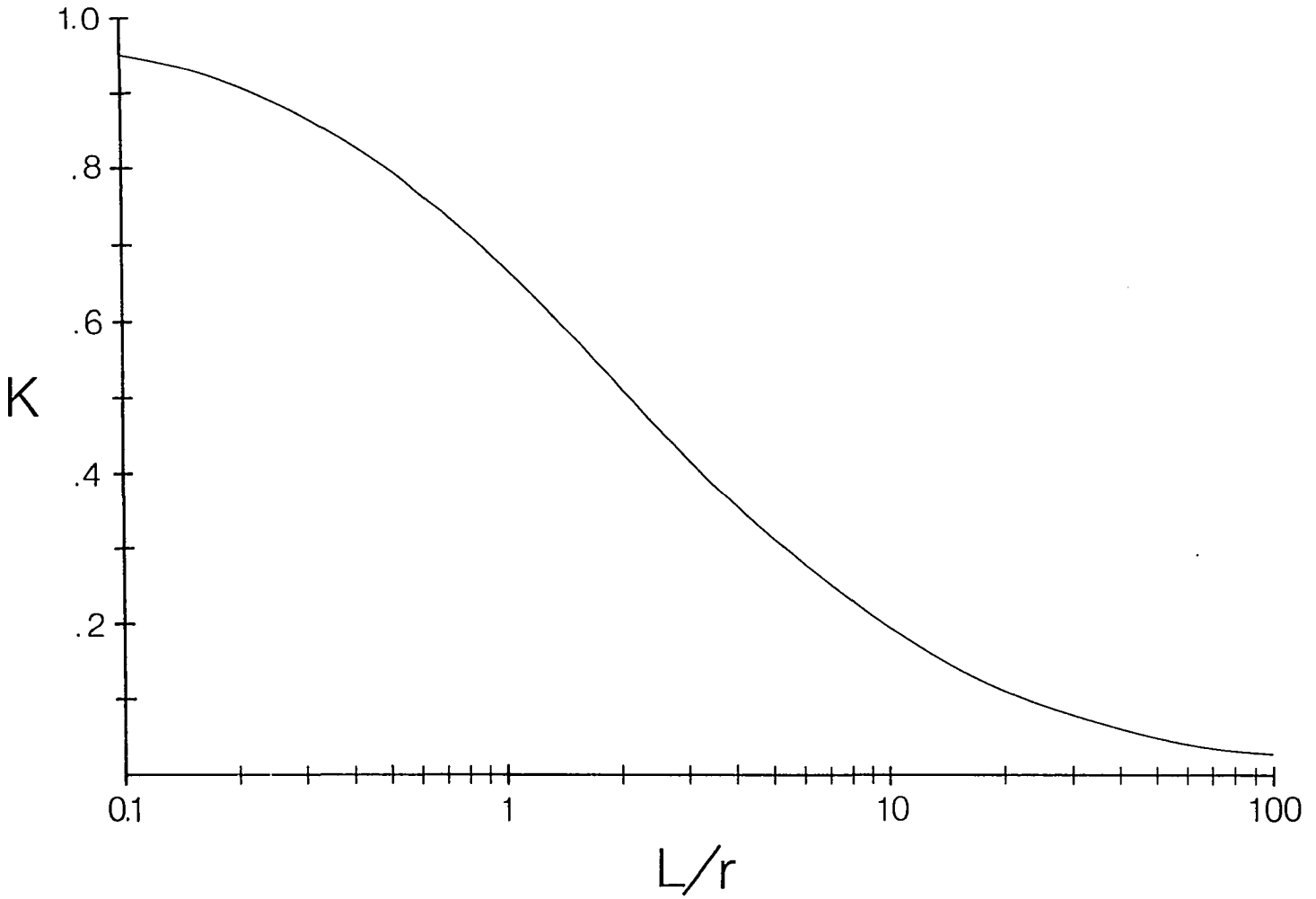

Figure A4. Clausing factor K versus the ratio of tube length to radius

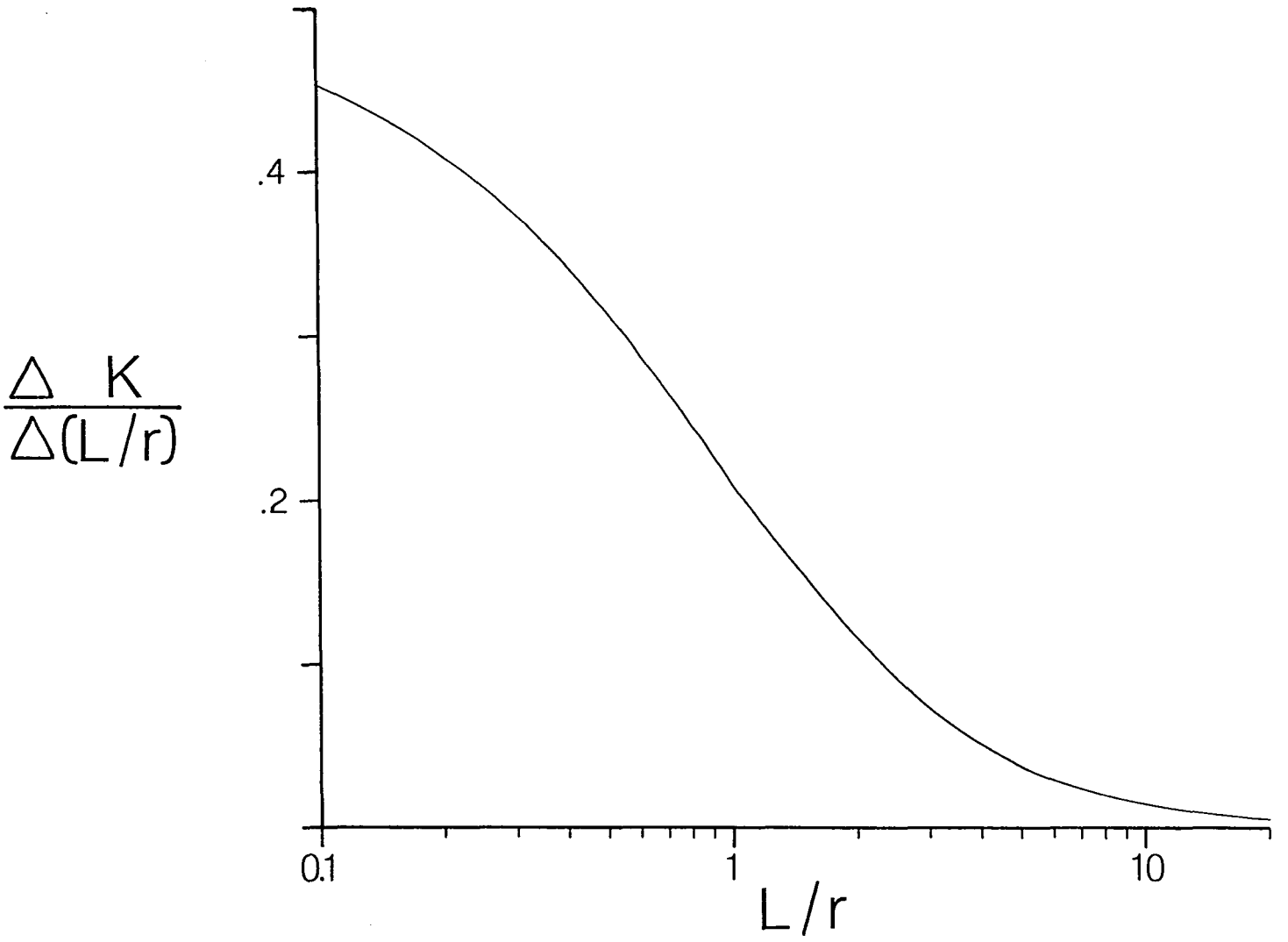

Figure A5. Rate of change of K with L/r versus L/r

rapidly with tube length for $L/r \gtrsim 3$. The impact of this is that in design the struggle to increase conductance is very profitable in the neighborhood of $L/r \gtrsim 3$, but for $L/r > 3$, sizable gain is very difficult to come by. This represents a much more concrete rule for vacuum system design.

It is possible to take advantage of this property of conductance [5]. The outermost square aperture of the detector chamber has a width W_D and a conductance C_D. The throughput Q_1 into the first region of the detector is

$$Q_1 = C_D P_{MC}$$

where P_{MC} is the main chamber pressure. If the effective pumping speed 'behind' this aperture in the detector's first region is S_1, then the pressure P_1 in the first region is

$$P_1 = Q_1 \div S_1 \quad .$$

However, if, instead of being mounted directly on the detector faceplate, the outermost aperture is mounted at the end of a tube of length $2W_D$ and diameter $\sqrt{2}\, W_D$ extending from the faceplate, then the conductance between the main chamber and the first detector regime can be lowered approximately 60%. This cuts the throughput Q_1 into this region roughly in half and, therefore, reduces the pressure in the first detector region P_1 to about half that obtained in the previous arrangement. Essentially, this is equivalent to doubling the effective pumping speed S_1 in the first region. Obviously, the idea (and the tube length) can be extended.

Properly utilizing this technique can eliminate the advantages and the difficulties involved in using adjustable detector aperatures.

References

1. M. Knudsen, Kinetic Theory of Gases (Methuen and Co., Ltd. London, 1952), 3rd Edition, p. 21.

2. Based on (January) 1983 prices for Varian oil diffusion pumps. Varian/IEG, 708 Landwehr Rd., Northbrook, IL 60062.

3. Based on (November) 1983 prices for Perkin-Elmer Conventional (x) and D-I (o) design ion pumps. Perkin-Elmer, Vacuum Products Div., 6509 Flying Cloud Drive, Eden Prairie, MN 55344.

4. P. Clausing, Ann. Physik 12, 961 (1932).

5. This simple and elegant technique is widely used by European researchers. In private communication with Manfred Faubel, Max-Planck-Institut für Strömungsforschung, Göttingen, West Germany.

APPENDIX B. RSA EXPERIMENTAL CONTROL

A great deal of the hardship and complexity involved in operating the rotating source apparatus has been eliminated by an elegant control and data processing system designed by Harold Skank of the Ames Laboratory Instrumentation Services Group. The two stepping motors, which position the sources, and the time-of-flight motor are all under microprocessor control. Also, the signal in 'single shot' and cross-correlation time-of-flight studies and differential scattering experiments is processed by the unit. Herein a brief description by the engineer responsible, Harold Skank, is given[1].

Prest-X System Description

The Prest-X system was designed to provide control and data acquisition capabilities for a dual source, crossed beam, kinematics chemistry experiment. The system consists of a 6809 microprocessor, functioning as the system central processor unit (CPU), the usual random access memory (RAM), sixteen kilobytes of control read-only memory (ROM), a teleprinter serial channel, and a number of special input-output (I/O) ports dedicated to hardware required to control the experiment. The CPU runs a menu driven system, operating under a ROM based tasking system specifically designed for experiment support.

---

[1]Further details are available by contacting Harold Skank, Ames Laboratory Instrumentation Services Group, Ames Laboratory, Iowa State University, Ames, Iowa 50011.

The decision to design the software based upon a menu driven system was prompted by the need to reduce the training time required for succeeding users of the experiment facilities. With this in mind, a menu driven system provides a natural vehicle to convey prompts and queries, greatly reducing the need for learning a special command language.

The following discussion will describe specific items of the design in greater detail.

Prest-X Hardware

The central decision making element in the experiment control system is a 6809 microprocessor. The implementation is a design by the Ames Laboratory Instrumentation Services Group, and was developed about a local bus convention to simplify system extensions. Thus, the system hardware is modular with only the CPU requiring a specific bus slot dedicated to its use. Other elements in the design (although they are not all necessary for this experiment) include eight-kilobyte RAM and ROM boards, serial communication boards, a parallel communication board, a triple sixteen-bit timer/counter board, a dual channel, dual mode digital to analog converter board (C/A), and various other support circuits, including other processor configurations.

In the Prest-X design, the following specific I/O facilities exist and are used as described below:

I. Three triple sixteen-bit timer/counter boards used for:
    1. Phase-lock control of the chopper system (4 sixteen-bit sections).

2. Variable modulo clock for angle motor step control (1 sixteen-bit section).
3. Dual data counters for the molecular beam timer and Gate system (2 sixteen-bit sections).
4. Monitor timer for multi-channel scaler operations (2 sixteen-bit sections).

II. Five twenty-bit parallel interface boards used for:
1. Multi-channel scaler data transfers (1 board).
2. Multi-channel scaler control transfers (1 board).
3. X-Y display of stored spectrum date (1 board).
4. Source beam motor control, limit switch monitor, and monitor timer control (1 board).
5. Molecular beam timer and gate control (2-bits of 1 board).

III. One dual D/A channel (driven by one of the parallel interface boards above), providing two channels of 12-bit resolution digital to analog conversion. The design incorporates a synchronization feature whereby the inputs to two D/A components may be changed at the same time, resulting in sharper display of digital data.

IV. A two-board multi-channel scaler (controlled by two of the parallel interface boards) providing up to 4096 channels of 16-bit data acquisition. In the Prest-X system, the multi-channel scaler (MCS) uses only 1024 channels, and the advance from channel to channel is driven from the chopper drive system. Special synchronization circuitry, driven by an optical

sensor, insures that individual sweeps are started at the proper time. Control commands (accessible from software) permit transfer of stored data from the MCS to the host processor. This transfer is done in a destructive-read fashion, thereby providing a means of clearing the MCS data memory area as well. Start commands are synchronized with the optical sensor signal from the chopper disk, and stop commands are executed only at the end of complete traces, so that only entire traces are recorded. In addition, other special circuitry monitors the most significant data bit and provides a flag to the host processor when data has reached half-scale, permitting transfer to the host processor before data loss occurs.

High speed data latches are used to reduce the scaler dead time to approximately 100 nanoseconds, while memory cycle timing considerations limit the channel dwell time to an approximate minimum of 815 nanoseconds. Fully synchronous counters are used to reduce the state transition time after a count pulse. These counters, along with their channel synchronization circuitry, limit the maximum count-rate within a channel to approximately 11,500,000 counts per second.